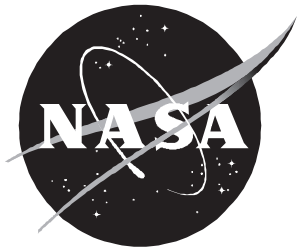

NASA Technical Paper 3502

Experimental Investigation of Inlet-Combustor Isolators for a Dual-Mode Scramjet at a Mach Number of 4

Saied Emami
Lockheed Engineering & Sciences Company • Hampton, Virginia

Carl A. Trexler
Langley Research Center • Hampton, Virginia

Aaron H. Auslender
Lockheed Engineering & Sciences Company • Hampton, Virginia

John P. Weidner
Langley Research Center • Hampton, Virginia

May 1995

Available electronically at the following URL address: http://techreports.larc.nasa.gov/ltrs/ltrs.html

Printed copies available from the following:

NASA Center for AeroSpace Information
800 Elkridge Landing Road
Linthicum Heights, MD 21090-2934
(301) 621-0390

National Technical Information Service (NTIS)
5285 Port Royal Road
Springfield, VA 22161-2171
(703) 487-4650

Summary

Experimental studies were conducted in the cold-flow Mach 4 Blowdown Facility (M4BDF) at the Langley Research Center to parametrically investigate inlet-isolator performance in an airframe-integrated ramjet/scramjet engine. The inlet-isolator test data presented herein result from both variations in geometry (isolator length and rearward-facing step height) and flow-field properties (boundary-layer thickness and oblique-glancing sidewall shock interaction). These data from the coupling of the inlet and isolator provide a portion of the parametric database required in a cycle deck to predict inlet-isolator performance over the ramjet envelope for the design of a hypersonic vehicle.

In order to generate such a database, a generic, two-dimensional, planar inlet-isolator-diffuser model was designed and fabricated to replicate the lines typical of a dual-mode scramjet integrated with a hypersonic vehicle (i.e., a design typical of a flight engine). A large and flight-realistic parametric variation of test data was obtained by providing several interchangeable, rotating cowls of different lengths and also planar isolator sections of different lengths. The combination of inlet cowls and isolator sections resulted in a total of 250 geometric configurations. The length of the isolator varied from 2.7 to 16.7 inlet throat heights by combining sections of different lengths. Rearward-facing steps were also introduced in the isolator to simulate fuel injector locations that are typically used when the isolator section serves as a combustor for supersonic combustion ramjet (scramjet) operation. Each inlet-isolator geometry was also tested with and without a horizontal forebody plate to alter the thickness of the turbulent boundary layer approaching the inlet.

The simulation of combustion pressure rise (to study inlet-combustor isolation) during the ramjet operational mode was accomplished by back pressuring the model flow path by using a variable-area throttling mechanism. This mechanism, when attached to the aft end of the isolator-diffuser model, was designed to throttle the flow gradually via a movable flap pivoting about a hinge near the throttling device exit. For each geometry tested, back pressuring was increased gradually by closing the throttling mechanism until the inlet was forced to unstart.

Model instrumentation included 110 wall static pressure orifices mounted flush on the inlet ramp, sidewalls, cowl, isolator, and throttling mechanism sections. Each data cycle, which represents the pressure distribution throughout the model at a given time, was recorded via an electronic-sensing pressure system that sampled data at 1 Hz.

The results reveal that the performance of each isolator is dependent not only on inlet geometry and forebody boundary-layer thickness but also on the isolator length and isolator step area change. For each inlet cowl, set at a given deflection angle, the maximum pressure that the isolator could withstand just downstream of the isolator prior to inlet unstart was denoted as the peak pressure. These peak pressure data were incorporated in all the analyses to define the performance and set the upper threshold of the inlet-isolator operation. The results show that the combined inlet-isolator maximum back-pressure capability was increased with increasing isolator length and increasing inlet contraction ratio, and it was decreased by inlet distortion and a rearward-facing step area increase in the isolator.

Introduction

The coupling of the isolator with the inlet and combustor is a necessary component in a hypersonic engine flow path integration over the ramjet (RJ) portion of the flight envelope. The isolator section starts at the minimum geometric cross-sectional area of the inlet, often referred to as the “inlet throat,” and it extends to the combustor section in the form of a constant-area (or nearly constant-area) duct. In the ramjet mode, Billig, Dugger, and Waltrup (ref. 1) recognized the need for inlet isolation while testing a hydrogen apparatus. Because of the absence of an isolator, they used boundary-layer bleed to stabilize the shock system at the burner entrance. However, the boundary-layer bleed enhanced the pressure drop immediately downstream of the burner entrance.

Yet, in practice, a direct coupling of the inlet and combustor is a highly optimistic scenario because large amounts of boundary-layer bleed are required. Flow distortion at the inlet throat and viscous boundary-layer growth combined with shock-induced boundary-layer separation typically will not allow the combustor pressure to reach a significant fraction of the normal shock pressure rise before inducing a terminal shock that will unstart the inlet. With sufficient isolator length, the peak pressure in the combustor can gradually reach as much as 90 percent of the normal shock pressure rise at the inlet throat with the terminal shock contained within the isolator section. However, to achieve 90 percent of the normal shock pressure rise at the inlet throat, a long isolator is required and this translates into an increase in vehicle takeoff gross weight (TOGW). Hence designing an isolator of such length is unrealistic. Consequently, an optimal isolator length that yields a large percentage of the normal shock pressure rise at the inlet throat with short length scales will result from trade-off studies of integrated components over the flight trajectory.

Two interdependent functions are ascribed to isolators. First, isolators are expected to behave as a buffer zone between the inlet and combustor in order to impede or, at least, to minimize interferences between

components. In this case, the isolator is required to permit continuous inlet operation over the specified speed range while withstanding the high peak pressure rises that originate in the combustor section. The second function of the isolator is to diffuse the supersonic flow to a subsonic condition and maximize recovery of the total pressure that is vital to efficient operation of both the inlet and combustor in the ramjet mode. Pratt and Heiser (ref. 2) used the "H-K" (thermal energy versus kinetic energy) coordinates to explore and analyze the complex interactions between system components (isolator and burner) in dual-mode combustion systems. They concluded that the nature of interaction between the isolator and combustor is different for ramjet and scramjet operations. In the ramjet operational mode, a constant-area isolator must contain a shock system consistent with subsonic combustion pressure rise. Whereas in the scramjet operational mode, heat addition in a constant-area combustor occurs in a separated core flow at nearly constant pressure equal to the maximum pressure rise at the combustor exit.

The flow process in the isolator in the ramjet operational mode is a series of complex multiple interactions of shock waves with the turbulent boundary layer, usually referred to as a "normal shock train." The formation of this shock train initiates inside the combustor and progresses upstream in the isolator section as the combustor pressure increases because of heat release. The local heat release compresses the flow streamlines in the combustor. The streamline compression creates a blockage that grows in size with the increase of pressure because of the fuel heat release in the scramjet combustor. If the blockage is too great or the isolator duct is too short, the shock train disturbance can extend upstream into the inlet and cause inlet instability or unstart.

Existing experimental data on shock-wave–boundary-layer interactions in constant-area (or nearly constant-area) duct flows are mostly in the form of schlieren photographs and wall static pressure measurements. E. P. Neumann and F. Lustwerk concluded in 1947 that the length of a normal shock train in a constant-area duct can be determined by the flow area of the boundary layer relative to the total cross-sectional area of the duct and by the Mach number immediately upstream of the initial location of the shock train. McLafferty et al. (ref. 3) presented the following conclusions from their tests in a constant-area passage having a circular cross section: (1) the pressure recovery will be maximized if the length of the isolator duct is approximately equal to the length of the shock train, (2) the length of the shock train required to obtain the complete static pressure rise increases with an increase in either the boundary-layer thickness relative to the duct diameter or the average Mach number upstream of the shock train, and (3) the profile at the exit of the subsonic diffuser becomes less uniform if the length of the isolator (for a supersonic inlet) is less than the length of the shock train.

With the advent of the National Aero-Space Plane (NASP) Program, development and application of numerical techniques to solve nonlinear aerodynamics and propulsion problems, such as the inlet-isolator problem, have increased. Hataue (ref. 4) used the second-order Total Variation Diminishing (TVD) technique based on two- and three-dimensional Navier-Stokes equations to investigate shock-wave–boundary-layer interactions in rectangular and circular cross-sectional area ducts. His results showed a bifurcated shock pattern a short distance ahead of the point where the essentially perpendicular "normal" shock wave impinges on the boundary layer. As the interaction became stronger, the shape of the shock wave changed from a bifurcated shock to a cross-shaped shock pattern. Lin, Rao, and O'Connor (refs. 5 and 6) also numerically simulated flows in a two-dimensional (2-D) constant-area duct with an inflow Mach number of 3.0. They used Reynolds-averaged compressible Navier-Stokes equations with the Baldwin-Lomax zero-equation model for flows outside recirculation zones and a backflow turbulence model within the recirculation zones. They examined the effect of the back pressure, confinement, and inflow Mach number on the formation and pattern of the oblique shock train and its interaction with the turbulent boundary layer. Hunter and Couch (ref. 7) modeled a three-shock inlet at a Mach number of 3 coupled with an isolator test article and used a 2-D Navier-Stokes code to study flow physics and shock-train characteristics. Area variation, created by manipulating a flow plug deployed in the downstream diffuser section, was used to simulate combustion pressure rises. The converged analytic solution demonstrated the spatially oscillatory nature of the centerline Mach number undergoing recompressions and reaccelerations. The study also concluded that turbulence modeling is highly critical for shock-train and shock–boundary-layer predictions.

Carroll and Dutton (refs. 8 and 9) used a nonintrusive, two-component laser Doppler velocimeter (LDV) to characterize the flow physics and parameters of a flow at a Mach number of 1.61 that generated a multiple normal-shock–turbulent-boundary-layer interaction in a rectangular duct. Their results indicated that the shock-train system consists of a series of symmetric normal shocks in which the first shock is bifurcated, has incipient separation at its foot, and is followed by several weaker, nearly normal shocks. The velocity component data revealed that two similar expansion processes occurred after both the bifurcated and the unbifurcated shocks. Each expansion originates near the wall and forms an aerodynamic converging-diverging nozzle

effect in the core flow. Measured streamwise centerline Mach number distributions and, consequently, the centerline static pressure distribution showed temporally steady, spatially oscillatory behavior with gradual dampening from supersonic to subsonic through the shock trains. From an examination of Mach number distributions on the flow centerline, one can infer that the smooth rise in the wall static pressure distributions is in sharp contrast with the oscillatory centerline static pressure distribution.

Although research on isolators, specifically isolators with circular cross sections, has been extensive, little of that work, if any, has included flow distortions ahead of the planar isolator created by actual coupling of both inlet and isolator flow fields. The tenet of this report is to document isolator operational characteristics in terms of isolator pressure rise and shock-train length as a function of aerodynamics flow properties that are inherent in the coupling of the isolator with both the inlet and the combustor, such as flow distortion due to boundary layers and shock waves. To achieve this goal, an extensive parametric test program was conducted to create a database necessary for the design of a ramjet inlet-combustor isolator for a vehicle in ramjet operation mode for a future high-speed vehicle. Combinations of different isolator lengths with and without rearward-facing steps were coupled to an inlet with three different rotating cowl lengths to investigate the maximum pressure rise in the isolator as a result of mechanically induced combustor back pressure.

Symbols and Abbreviations

A_{cap}	area of inviscid stream tube captured by inlet, $H_{cap}W$
$A_{cap,\ act}$	area of actual (viscous) stream tube captured by inlet
A_g	area of glow path at cowl lip station, H_gW (geometric)
A_m	frontal of inlet, H_mW
A_{th}	geometric throat area, $H_{th}W$
$A_{th,\ a}$	aerodynamic throat area
B.L.	boundary layer
C_f	skin-friction coefficient, τ_w/q_{edge}
CAP	inlet mass capture ratio, $A_{cap,\ act}/A_m$
CR	inlet geometric contraction ratio, H_{cowl}/H_{th}
$(CR)_a$	inlet aerodynamic contraction ratio, $H_{cap,\ act}/H_{th}$
$(CR)_i$	inlet geometric internal contraction ratio. H_g/H_{th}
H	boundary-layer shape factor, δ^*/θ
H_{cap}	height of inviscid stream tube captured by inlet (fig. A1)
$H_{cap,\ act}$	height of actual (viscous) stream tube captured by inlet (fig. 5)
H_{cowl}	height of cowl leading edge (fig. 3)
H_g	height of flow path at cowl lip (fig. A1)
H_m	model height, 2.30 in. (fig. 3)
H_{th}	inlet throat or isolator entrance height, 0.4 in. (fig. 3)
I.D.	inside diameter
L	isolator length, in.
LC	long cowl
L_c	inlet cowl length (figs. 4(d) and A1), in.
L_r	length of compression ramp to inlet throat, 9.77 in. (figs. 4(a) and A1)
L_s	isolator length up to rearward-facing step, in.
M	Mach number
MC	medium cowl
max.	maximum
N_{Re}	Reynolds number
O.D.	outside diameter
p	pressure, psia
p_s	isolator maximum pressure before inlet unstart, psia
q	dynamic pressure, $(\rho U^2)_{edge}/2$
R	gas constant, ft-lbf/(lbm-°R)
Ref.	reference
rad.	radius
SC	short cowl
St.	station
T_t	total temperature, °R
U	maximum boundary-layer-edge velocity, calculated from pitot measurements (fig. 6), ft/sec
u	local streamwise velocity, ft/sec
W	model geometric width, 2.0 in.
X	axial distance from leading edge of compression ramp, in.

x'	static orifice position in x-direction, relative to reference plane (fig. 4)
y	Cartesian coordinate in vertical direction, in.
z'	static orifice position in z-direction, relative to model centerline (fig. 4)
α	precompression ramp angle, 11° (figs. 3 and A1)
β	inlet convergence angle, deg (figs. 3 and A1)
γ	specific heat ratio
δ	boundary-layer thickness, in.
δ^*	boundary-layer displacement thickness, in.
θ	boundary-layer momentum thickness, in.
θ_c	cowl angle relative to free stream, deg (figs. 3 and A1)
θ_r	angle of shock wave generated by compression ramp and ramp boundary layer (fig. 5), deg
θ_s	shock turning angle, deg (fig. 5)
θ_w	angle of shock wave generated by inviscid flow over compression ramp (fig. A1), deg
μ	air viscosity, lbf-sec/ft^2
ρ	density, lbm/ft^3
τ_w	wall shear stress, psi

Subscripts:

a	aerodynamic
act	actual
cap	captured
edge	condition within 1 percent of free stream
N.S.	condition behind normal shock
t	total conditions
th	throat conditions
1	free-stream conditions
2	after normal shock ahead of pitot tube

Development of Experimental Configuration

Test Facility and Conditions

The Mach 4 Blowdown Facility (M4BDF) at the Langley Research Center was used for this experimental investigation. The test section, which has a 9- by 9-in. cross section, is nominally 15 in. long with glass schlieren windows enabling photographs to be made. The total pressure can be varied and set at any pressure between 150 and 250 psia (a unit Reynolds number variation between 15.75×10^6 and 26.25×10^6 per foot). The two-dimensional fixed-geometry facility nozzle is capable of supplying a steady cold airflow to the test section for a nominal test time of 2.0 minutes. Calibration of the M4BDF (in unpublished data) revealed that the nozzle had a core flow Mach number of 4.03 ± 0.02. The maximum permitted aerodynamic blockage created by a sharp leading-edge model in the tunnel is approximately 13 percent for a flow-through model.

The facility stilling chamber delivered air to the test section at a nominal Reynolds number and a total pressure of 21×10^6 per foot and 200 ± 2 psia, respectively, to all model configurations during the course of this test series. At these conditions, the tunnel free-stream static pressure entering the test section is 1.266 ± 0.034. All other tunnel test conditions were invariant during the course of these tests with the exception of tunnel-flow total temperature. This was unavoidable because of a variation of atmospheric temperature and the absence of a flow heater. The tunnel-flow total temperature varied between $500°\text{R} \pm 3°\text{R}$ and $540°\text{R} \pm 3°\text{R}$ during this period.

Errors introduced into the test data due to a slight variation in the tunnel operating condition (with a total pressure of 200 ± 2 psia and a static pressure of 1.266 ± 0.034 psia) are classified as accuracy errors or systematic errors. To eliminate accuracy errors in test data, all test data were nondimensionalized by tunnel static pressure for each test run. The precision error due to instrumentation and to each pressure gauge is ± 0.25 percent maximum for any static pressure readings. The examination of test data showed that the data were repeatable.

Test Model

The two-dimensional inlet-isolator model was designed at 2-percent scale to replicate the generic features of a hypersonic, air-breathing lifting-body propulsion system. It included inlet compression, an isolator, step area changes in the isolator using rearward-facing steps (which simulate fuel-injector locations for the scramjet mode of operation), and an expanding section downstream of the isolator. A portion of the expanding section served as a diffuser during the ramjet mode of operation; however, the entire expanding section serves as a nozzle during the scramjet mode of operation. Here, the expanding section is referred to as a “diffuser” for the purpose of consistency with the goals of these experimental investigations at the ramjet mode of operation. Figure 1 shows the uninstalled model with various parts labeled. To achieve parametric model variations, the model was constructed from wedges and blocks to allow easy fabrication and simple assembly. Schematic diagrams of the cross section, dimensions, and instrumentation layouts for the 2.0-in-wide and 2.3-in-high test

model are shown in figures 2, 3, and 4, respectively. The wetted surfaces that enclose the flow path consist of three major flow categories: inlet, isolator, and combustor/ diffuser.

The model inlet consists of a compression ramp, interchangeable cowls, flow fences, and a portion of the sidewalls. The inlet compression ramp was designed to simulate a portion of any generic vehicle forebody. The 11° compression ramp is 9.77 in. long and changes abruptly to a flat (0°) surface which marks the inlet throat and the beginning of the isolator section. The purpose of the 60° sweptback fences (fig. 1(a)) is threefold: to contain the shock wave generated by the 11° compression ramp, to prevent spanwise flow spillage on the ramp, and to bleed (or divert) the corner boundary-layer flow generated by the fences themselves (to minimize three-dimensional distortions of the flow entering the inlet). The corner flow bleeding was accomplished through two open gaps just before the mainstream core flow entered the enclosed portion of the inlet. The compression ramp and the fences remained unchanged for all test configurations. The inlet geometry parameters included three different cowl lengths (fig. 5). Each cowl was used with various isolator lengths to examine the effects of inlet distortion created by cowl length variations on peak pressure in the isolators. Each cowl angle associated with each cowl length generates a different Mach number at the throat as the result of variations in shock patterns (fig. 5), captured mass, and inlet contraction ratio (aerodynamic and geometric). The compression ramp turns the flow 11°, and the interaction of the flow with the cowl generates a cowl shock whose strength and number of shocks in the inlet depend on the cowl angle and cowl length. The strongest cowl shock is generated when the cowl is not deflected (i.e., the cowl internal surface is parallel to the free-stream flow upstream of the model). To change the cowl angle, each cowl was designed to rotate about a hinge that was located 0.4 in. above the end of the compression ramp where the geometric throat starts. (The O-ring was placed behind the hinge point to prevent mass spillage.) The cowl rotation angle was set by an actuator mounted outside the tunnel. The geometric throat cross-sectional area (0.4 in. high and 2 in. wide), remained fixed for all test configurations, thus allowing the inlet exit or isolator entrance to maintain an aspect ratio of 5.0.

The effect of incoming boundary layer on the inlet operability and, consequently, on the isolator pressure recovery was also examined. A flat plate extending 12 in. upstream of the compression ramp was added to alter the incoming flow boundary layer on the body side of the model. For comparison, each configuration was tested with and without the flat plate, and the results of each are referred to as “thick” and “thin” turbulent-boundary-layer configurations, respectively.

Two types of isolators were used in the test matrices: (1) a constant-area variable-length isolator with and without steps followed by a diffuser section expanding abruptly at 20°, and (2) a constant-area isolator followed by a 6° expanding isolator which, in turn, is followed by a diffuser section expanding at 20° (fig. 4(c)). The expanding isolator was chosen to compare the results with that of constant area in terms of pressure rise. The first of the two isolators was used extensively in the test matrices. The isolator section of the model, on the body side behind the ramp, could be arranged in several configurations by using combinations of three interchangeable blocks (fig. 4(b)) followed by the aft diffuser wedges (fig. 4(c)). The aft wedges forming the nozzle section of the model extended some length into the throttling device section and could slide axially in order to insert or remove isolator blocks of different lengths. (The location of aft wedges with different isolator lengths is shown by dashed-lines in fig. 3.) Three interchangeable aft cowl plates (fig. 4(e)), two with a 0.028-in. step (7 percent increase in geometric throat) and one without a step, formed the top half of the isolator section. The aft cowl mated directly with the throttling device interface shown in figure 4(g).

The two-dimensional throttling device was used to back pressure the model in order to simulate combustion pressure rise. The throttling device was 2.043 in. wide and 2.75 in. high and utilized a variable-throat mechanism that was actuated by an electric motor. During a test, the movable flap on the throttling device was closed until the throttling device forced a shock train upstream toward the inlet throat. Back pressuring of the isolator and inlet was then continued by closing the throttling device flap until the inlet unstarted. The schematic diagram in figure 2 shows the interfaces between the different model parts and the throttling device.

Model Configurations

The inlet-isolator model was designed to establish a parametric database necessary for the design and trade-off studies of air-breathing lifting-body hypersonic vehicles over the ramjet envelope. The 11° forebody compression ramp and 0.4-in-inlet geometric throat height remained the same for all configurations in the test matrices. Model parametric variations consisted of three different inlet cowl lengths (i.e., the cowl length divided by the inlet geometric throat height (L_c/H_{th}) of 6.25, 9.75, and 11.00) with different isolator lengths (i.e., the isolator length divided by the inlet geometric throat height (L/H_{th}) of 2.7, 4.7, 8.7, and 16.7), each with and without rearward-facing steps. The rearward-facing steps

(0.028 or 0.050 in. on the body side and 0.028 in. on the cowl side) replicate fuel injectors used in supersonic combustion ramjets (scramjets) and generate a step increase in isolator cross-sectional area. The steps located in the isolator were at 0.68 in., or 2.68 throat heights downstream of the inlet throat. The steps were constructed by positioning and adjusting a shim of specific thickness underneath the isolator blocks on the body side (fig. 3). The steps on the cowl side were made by using different aft cowl sections (aluminum), as shown in figure 4(e). The isolators without rearward-facing steps had a constant area throughout the length of the isolator. The body side of all the isolators was joined with the step-expansion diffuser section followed by the throttling device. In addition, a 6° diffuser section (fig. 4(c), lower view) was fabricated and tested together with constant-area isolator lengths (L/H_{th}) of 4.7 and 8.7; the results were compared with constant-area isolators of the same length. The 6° expanding diffuser section also expands to 20° and matches with the lines of the throttling device. Tables I–III present a compilation of each model configuration that consisted of different geometric parameters for each inlet-isolator and isolator-nozzle combination.

Test Procedure, Data Acquisition, and Analysis

The principal objective of this test series was to obtain test data that are descriptive of the performance of inlet-isolator and isolator-combustor combinations that are representative of dual-mode flight scramjets. During the test duration of 2.0 minutes, the cowl angle and throttling-device exit opening were remotely actuated. For a given configuration, a test was first conducted in which the throttling device was left at the most open setting to minimize pressure disturbance upstream (to simulate the no-fuel case), and then the cowl, which was initially parallel to the inlet ramp, was slowly rotated open until inlet unstart was detected. The cowl was then slowly rotated closed until the inlet restarted and the tunnel was shut down. A static pressure orifice on the ramp, opposite the cowl leading edge, was continuously monitored to detect inlet unstart and restart. With a knowledge of the inlet operational map for each cowl, subsequent tests of that configuration consisted of choosing specific cowl angles and slowly closing the throttling device until the inlet unstarted. The inlet unstart is caused by disgorgement of a terminal shock out of the isolator into the

Table I. Inlet-Isolator Configurations for L/H_{th} = 2.7 and 4.7 With Diffuser Angle of 20°

Cowl length, in.	Boundary-layer plate	L_s/H_{th} = 0.7		L_s/H_{th} = 2.7		Plotfiles	Runs
		Body-side step height = 0.05 in.	Cowl-side step height = 0.028 in.	Body-side step height = 0.05 in.	Cowl-side step height = 0.028 in.		
L/H_{th} = 2.7							
4.4 (LC)						cofi6	41–49
	✓					cofi6	54–57
2.5 (SC)						cofi5	36–40
	✓					cofi5	58–61
L/H_{th} = 4.7							
4.4 (LC)						cofi10	105–108
	✓					cofi10	101–104
		✓	✓			cofi10	85–88
	✓	✓	✓			cofi10	89–92
				✓	✓	cofi8	70–73
	✓			✓	✓	cofi8	66–69

Table II. Inlet-Isolator Configurations for L/H_{th} = 4.7

Cowl length, in.	Boundary-layer plate	L_s/H_{th} = 0.7		L_s/H_{th} = 2.7		Plotfiles	Runs
		Body-side step height = 0.05 in.	Cowl-side step height = 0.028 in.	Body-side step height = 0.05 in.	Cowl-side step height = 0.028 in.		
L/H_{th} = 4.7 with diffuser angle of 20°							
3.9 (MC)						cofi10a	187–189
	✓					cofi10a	190–192
2.5 (SC)						cofi9a	109–113
	✓					cofi9a	97–100
		✓	✓			cofi9a	78–81
	✓	✓	✓			cofi9a	94–96
				✓	✓	cofi9	74–77
	✓			✓	✓	cofi9	62–65
L/H_{th} = 4.7 with diffuser angle of 6° turning into 20°							
4.4 (LC)						cofi12	118–121
	✓					cofi12	122–124
2.5 (SC)						cofi11	114–117
	✓					cofi11	125–128

inlet section (induced by an excessively high back pressure generated by the throttling device).

Aerodynamic contraction ratio, internal geometric contraction ratio, and inlet mass capture ratio are parameters that are used to define inlet performance for different cowl lengths and cowl angles. These inlet performance parameters are defined and quantified in the appendix.

Ninety-six static pressure orifices (0.060-in. O.D. and 0.040-in. I.D.) were installed in axial and spanwise arrays throughout each model configuration; an additional nine static pressure orifices were located in the throttling device. While closing the throttling device slowly to increase back pressure, electronic scanning pressure (ESP) units with four modules simultaneously swept data throughout the flow path at 1-Hz intervals (the sampling rate frequency); each module had 32 pressure ports. Each data sweep throughout the model flow path is referred to as a "cycle." Thus, 120 cycles of data throughout the flow path were obtained within the 2 minutes of testing. At the end of each test run, the data stored in the data acquisition and control unit were transferred to a 386 PC (33 MHz) computer with a 200 megabyte hard drive. The flow meter and cowl positions were also recorded via two analog/digital (A/D) multiplexer units. Programs in Microsoft QuickBASIC language permitted plotting the data immediately after each test and comparing it with data taken from previous configurations.

Results and Discussion

A brief introduction to the forthcoming results and discussion is pertinent if one decides not to follow each section of this report sequentially. The "Results and Discussion" section of this report is divided into the following eight major sections:

1. State of Local Boundary Layer: Pitot measurements were used to investigate the state of the local boundary-layer flow at the entrance to the enclosed portion of the inlet and to quantify boundary-layer displacement thickness for both configurations with and without the foreplate. (See fig. 6.)

Table III. Inlet-Isolator Configurations for L/H_{th} = 8.7 and 16.7

Cowl length, in.	Boundary-layer plate	L_s/H_{th} = 0.7		L_s/H_{th} = 2.7		Plotfiles	Runs
		Body-side step height = 0.05 in.	Cowl-side step height = 0.028 in.	Body-side step height = 0.05 in.	Cowl-side step height = 0.028 in.		
L/H_{th} = 8.7 with diffuser angle of 20°							
4.4 (LC)						cofi2	9–14
	✓					cofi2	15–18
				✓	✓	cofi4	30–32
	✓			✓	✓	cofi4	25–28
2.5 (SC)						cofi1	1–8
	✓					cofi1	19–21
				✓	✓	cofi3	33–35
	✓			✓	✓	cofi3	22–24
L/H_{th} = 8.7 with diffuser angle of 6° turning into 20°							
4.4 (LC)							167
L/H_{th} = 16.7 with diffuser angle of 20°							
4.4 (LC)						cofi14	134–137
	✓					cofi14	147–151
2.5 (SC)						cofi13	138–142
	✓					cofi13	143–146

2. Inlet Design and Operation: This section describes both the fundamental philosophies behind the design of the inlet compression ramp (the external part of the inlet) and the three inlet cowl lengths (the internal portion of the inlet); in addition, this section is also followed by a discussion of the interaction of each cowl shock with the expanding flow at the inlet geometric throat (shoulder) and the movement of the aerodynamic throat of the inlet for the short cowl configuration at low inlet convergence angles (low contraction ratio). (See figs. 7–11.)

3. Inlet Throat Flow Properties: Static pressure tap measurements, located on the body side and cowl side of the inlet geometric throat, were area averaged in order to define the inlet throat flow properties (Mach number, total pressure, and size of the aerodynamic throat area). The inlet throat properties are used to separate isolator performance from that of the inlet and to evaluate the effectiveness of the isolator (item 8 listed below) as a single unit with the presence of inlet effects on isolator inflow at the junction of the inlet and the isolator. (See figs. 12–15.)

4. Inlet Unstart and Restart Characteristics: The triggering of inlet unstart is described in this section, which shows that all the inlets unstarted at about the same inlet convergence angle independent of cowl length, inlet contraction ratio, and inlet mass capture; in addition, this section is followed by a short discussion about unstart pressure load. (See figs. 16–18.)

5. Isolator Back-Pressure Characteristics: Both the required isolator length to contain a full shock-train length and the minimum and maximum back pressures to

simulate the effects of no-fuel and maximum-fuel fraction that can be added without unstarting the inlet are discussed in this section for inlets with three different cowl lengths at the maximum and at a medium contraction ratio. (See fig. 19.)

6. Maximum Capability of Inlet-Isolator Back Pressure: This section shows the maximum inlet-isolator pressure rise that each isolator was able to sustain before the inlet unstarted. The discussion in this section evaluates the inlet and isolator operation as a single unit over a wide range of inlet contraction ratios. (See figs. 20–24.)

7. Effects of Inlet Flow Distortion on Inlet-Isolator Maximum Pressure: Inlet losses attributed to a specific inlet cowl length are quantified in terms of the relative impact of those losses on inlet-isolator maximum-pressure capability for all the inlet configurations tested, with a common isolator length over a range of inlet contraction ratios. (See figs. 25–32.)

8. Isolator Effectiveness: The effectiveness of an isolator as a single component, independent of the inlet, is evaluated in this section for a wide range of inlet contraction ratios. Isolator effectiveness is of significance during the course of a design process when assessing the contribution of various isolator lengths to the overall vehicle performance level (i.e., installed thrust). (See figs. 33–35.)

All the figures presented under items 6, 7, and 8 are plotted in terms of inlet contraction ratio. During the course of a realistic design and flow path trade study, one is typically required to evaluate different inlet-isolator configurations with the same mass capture. Thus, the inlet contraction ratio (see the appendix) and the data are presented in a manner consistent with this objective.

Note, with the help of figure A2 (which shows contraction ratio versus convergence angle for each inlet) and figures 12, 13, and 14 (which show the inlet throat flow properties), data versus convergence angle or other inlet throat flow properties are obtainable.

State of Local Boundary Layer

Pitot measurements were obtained to investigate the boundary layer entering the model body side for inlet-isolator configurations both with and without the boundary-layer foreplate. A single 0.060-in. O.D. pitot tube was flattened to 0.032 in. (ellipse minor axis) to measure the boundary-layer pitot pressure 6.81 in. in the axial direction downstream from the compression ramp leading edge (fig. 3). The forward cowl was removed for these boundary-layer measurements; however, the relative locations of these boundary-layer measurements vary with respect to each inlet cowl leading edge. These locations are 0.46 in. upstream of the L_c/H_{th} = 6.25 cowl leading edge, 0.94 in. downstream of the L_c/H_{th} = 9.75 cowl leading edge, and 1.44 in. downstream of the L_c/H_{th} = 11.00 cowl leading edge. The dimensions here are expressed with respect to the cowl leading edges when the cowls are at 0° cowl incidence (at inlet convergence angles of 11°). The measurements started 0.016 in. away from the wall and moved outward radially through the boundary layer to the free stream.

To convert pitot profile data to velocity and Mach number profiles with the use of measured wall static pressure, assumptions are made that include an adiabatic wall and a Prandtl number of unity. Thus, the recovery temperature at the wall (T_{wall}) is equal to the flow total temperature (T_t). In addition, an empirical power-law velocity profile for turbulent boundary layers was chosen to compare with the experimental velocity profile. Exponents (n) of 1/7 and 1/10, which are universally accepted to define fully turbulent flows, were used to model the experimental velocity profiles (note that this general form of velocity profile does not apply in the viscous sublayer region):

$$\frac{u}{U_{edge}} = \left(\frac{y}{\delta}\right)^{1/7} \tag{1}$$

The results from the thin-boundary-layer experiments (without the forebody plate) show that the velocity profiles from the pitot pressure data and the 1/7 power law are in close agreement (fig. 6(c)). However, for the thick boundary layer (with the forebody plate), the 1/10 power-law velocity profile is in close agreement with the pitot-pressure-derived velocity profile. Figure 6(c) also shows that the boundary-layer thicknesses are approximately 55 and 25 percent of inlet geometric throat height for thick and thin boundary layers entering the inlet, respectively. Figure 6(d) shows the Mach number profiles for the thin and thick boundary layers.

Quantification of local boundary-layer characteristics, except for the skin-friction coefficients, for both thin and thick boundary layers was numerically integrated from experimental data (pitot pressure profiles), and results are presented in table IV. A comparison of the shapes of two velocity profiles close to the wall (fig. 6(c)) also shows that the wall skin friction is higher for the thin boundary layer than for the thick boundary layer. Obtaining the skin-friction coefficient from the data was not possible because of the limited spatial resolution of the measurements near the wall. Thus, the skin-friction coefficient was calculated from a semi-empirical equation (ref. 10) valid for compressible

Table IV. Local Boundary-Layer Characteristics With and Without Foreplate on Compression Ramp Behind Wedge Shock Based on Pitot Probe Data

[Located axially 6.81 in. downstream from compression ramp leading edge]

Configuration	Boundary-layer thickness, δ, in.	Boundary-layer displacement thickness, δ^*, in.	Boundary-layer momentum thickness, θ, in.	Shape factor ($H = \delta^*/\theta$)	Skin-friction coefficient, C_f
Model without foreplate (thin boundary layer)	0.1	0.036	0.0185	1.946	0.00207
Model with foreplate (thick boundary layer)	0.23	0.073	0.0425	1.717	0.00174

turbulent flow up to a Mach number of 4. This is written as

$$C_f = \frac{0.472}{(\log_{10} N_{\mathrm{Re}})^{2.58}\left(1 + \frac{\gamma - 1}{2} M_{\mathrm{edge}}^2\right)^{0.467}} \qquad (2)$$

where

$$N_{\mathrm{Re}} = \frac{(\rho U l)_{\mathrm{edge}}}{\mu_{\mathrm{edge}}}$$

based on the boundary-layer-edge condition, which is defined as the distance from the wall to the point where the velocity is within 1 percent of the free-stream velocity. Boundary-layer-edge conditions for both the thin boundary layer and the thick boundary layer are

$$(\rho U)_{\mathrm{edge}} = 127.18 \text{ lbm/ft}^2\text{-sec}$$
$$U_{\mathrm{edge}} = 2010.36 \text{ ft/sec}$$
$$T_{\mathrm{edge}} = 160.25^\circ\mathrm{R}$$

In these calculations, the length (l) is measured from the leading edge of the wetted surface and $\gamma = 1.4$.

Inlet Design and Operation

The inlet was designed to diffuse the approaching supersonic air at a Mach number of 4.03 in a manner consistent with current inlet-flow-path design for lifting-body hypersonic vehicles with two-dimensional planar surfaces. In all test cases, the external compression process was accomplished by a shock from the 11° wedge, which simulated a portion of a hypersonic vehicle forebody. A significant amount of the compression was also accomplished internally, where the process in the inlet was completely enclosed by the cowl, sidewalls, and compression ramp (fig. 3). The cowl shock glances along the inlet sidewalls and impinges on the compression ramp. Depending on the inlet cowl length, the inlet cowl shock could reflect several times from the compression ramp and cowl as it progressed toward and into the inlet throat area (fig. 5).

For all configurations, regardless of the inlet cowl length or angle, the level and distribution of pressure on the forward portion of the ramp are the same (figs. 7(a)–9(a)). An analysis of the ramp pressure level indicates that the combined effects of the 11° compression ramp and boundary layer produce approximately an equivalent 12° inviscid compression flow turn (fig. 5(b)). As explained earlier, the state of flow properties through the boundary layer was measured by using a pitot rake for configurations with and without forebody plate extension. The boundary-layer displacement thickness was calculated from the integration of velocity profile obtained from pitot data, and the resulting mass deficit through the boundary layer was taken into account in the calculation of inlet capture height and contraction ratio. (See the appendix.)

For internal compression, three inlet cowl lengths were designed and tested in order to produce different levels of flow distortion (skewed flow profiles) at the inlet geometric throat, where the inlet flow enters and interacts with the isolator. The distortion results from the interaction of uncancelled shocks with expansion waves, which originate from the inlet and shoulder. As explained previously, the design for each cowl length was based on the number of two-dimensional inviscid shocks theory. The short 2.5-in-long cowl (fig. 5(a)) was designed to compress the inlet internal flow through two shocks. From an inviscid point of view, the latter shock impinges on the cowl just upstream of the throat at an angle initially equal to the inlet convergence angle, it is strengthened by the compression corner formed by the hinge, and it reflects back into the isolator section at 11°. Meanwhile, on the ramp opposite the compression corner, flow expands at 11° as it enters the isolator section. The strong cowl shock and ramp corner expansion waves

are expected to create a distorted flow into the isolator section that can affect isolator performance.

Figures 5(b) and 5(c) also show shock patterns for both the medium and long cowls (L_c/H_{th} = 9.75 and 11.00, respectively). To reduce the inlet throat distortion levels entering the isolator and simultaneously to increase the inlet contraction ratio and throat static pressure, the L_c/H_{th} = 9.75 cowl was designed based on 2-D inviscid shock theory to produce a three-shock-wave reflected system within the inlet. Focusing the third shock on the ramp shoulder, independent of inlet convergence angle, was desirable in order to eliminate expansion waves. This configuration is commonly referred to as the "shock on shoulder" condition. The L_c/H_{th} = 11.00 cowl length is also a three-shock-wave reflected system. The third shock impinges on the inlet ramp upstream of the 11° expansion corner at the shoulder. In contrast to the L_c/H_{th} = 9.75 cowl, where the third shock is focused on the shoulder to minimize the distortion level to the isolator inflow, the isolator inflow distortion with a L_c/H_{th} = 11.00 cowl is caused by the presence of expansion waves from the shoulder and two discrete shock waves from the ramp and the cowl in the isolator section. Also note that the final shock impingement point moves less than 0.20 in. over the range of the inlet-cowl convergence angle.

Figures 7, 8, and 9 show the effects of cowl convergence angle on inlet pressure distributions on the ramp and on the cowl for the cowl lengths (L_c/H_{th}) of 6.25 (2.5 in.), 9.75 (3.9 in.), and 11.00 (4.4 in.), respectively. From these figures, the examination of the pressure variations at the junction of the inlet and isolator also indicates the inlet flow distortion specific to each cowl. In each figure, the "a" and "b" parts denote the thin incoming turbulent-boundary-layer configurations and the "c" and "d" parts denote the thick configurations. Figure 7 shows the consistent progression of inlet pressure rise with increase in convergence angles for both thin and thick boundary-layer configurations with a cowl length of L_c/H_{th} = 6.25. For a given convergence angle, the pressure rise on the body side increases; it starts at 8 in. and reaches a maximum pressure plateau before flow expansion begins at the inlet geometric throat, which reduces the pressure. Pressure distributions on the cowl show that the pressure rise, which starts at 8.8 in. from the compression surface leading edge on the cowl, is eventually reduced by expansion waves and extends into the isolator. The inlet throat flow distortion in the vicinity of the inlet-isolator junction for the L_c/H_{th} = 6.25 cowl design becomes evident when examining the steep decrease (flow expansion) and increase (flow recompression) of the body-side surface pressure, and also the increase and decrease of the cowl-side surface pressure. Compared with the same configuration with the thin boundary layer, the addition of the boundary-layer plate decreased the maximum operational inlet convergence angle before inlet unstart by about 1° (figs. 7(c) and 7(d)).

Figures 8(a) and 8(b) show the partial cancellation of the shock on the ramp shoulder for the L_c/H_{th} = 9.75 cowl over a wide range of convergence angles, with the exception of 10° for thin and 8.6° for thick boundary layers. At this high convergence angle, the sudden rise in pressure level slightly upstream from the geometric throat in the inlet could be attributed to the formation of a separated zone feeding upstream in the inlet and/or a slight misalignment of the third shock shifting forward in the inlet and finally reflecting into the isolator section. The magnitude of this pressure rise is less pronounced for the thick boundary layer. For the L_c/H_{th} = 9.75 cowl, the thick boundary layer (figs. 8(c) and 8(d)) reduces the operational inlet convergence angle by 1.4° (or by 14 percent) before inlet unstart (from 10° to 8.6°), and it also increases the throat pressure on both the ramp and the cowl when comparing the same convergence angles for the thin boundary layer (figs. 8(a) and 8(b)).

Figure 9 shows the pressure distributions within the inlet at different convergence angles for the L_c/H_{th} = 11.00 cowl. The rise and fall in pressure around the inlet geometric throat is evidence of isolator inflow distortion, which is caused by the last inlet shock wave reflecting downstream of the compression ramp shoulder. The inlet maximum operational convergence angle before inlet unstart was reduced by 0.3° for both the thin and thick boundary-layer configurations for the L_c/H_{th} = 11.00 cowl as compared with that of the L_c/H_{th} = 9.75 cowl.

An examination of the pressure distributions (up to the throat) in the enclosed sections of the inlets with internal compression (figs. 7, 8, and 9), independent of the isolator section, shows that the inlet pressure distribution rises and reaches a maximum near the geometric throat on both the body and cowl sides at any convergence angles above approximately 3° and 5° for the inlets with longer cowls (L_c/H_{th} = 9.75 and 11.00) and for the inlet with a short cowl (L_c/H_{th} = 6.25), respectively. If one defines the inlet aerodynamic throat location where the inlet surface pressure on the ramp and cowl is maximum, then the area location of the aerodynamic throat coincides with that of the geometric throat. The aerodynamic throat area is smaller in magnitude than the geometric throat area because of the viscous boundary-layer blockage (fig. 15).

An examination of the pressure distributions for the inlets at convergence angles of 5° or below for the short

cowl (circular symbols in fig. 7) and at 3° or below (not shown) for the long cowls (circular symbols in figs. 8 and 9) shows an unusual rise and fall of local surface pressure in the inlet on both the cowl and ramp. This phenomenon is obvious for the inlet with the short cowl and is subtly evident for the inlets with long cowls. To show this phenomenon, figures 10 and 11 display the pressure levels at several locations within the inlet as a function of convergence angle for both the $L_c/H_{th} = 6.25$ and 11.00 cowls, respectively. For the $L_c/H_{th} = 6.25$ cowl (fig. 10) at low convergence angles (less than 5°), pressure varies significantly with cowl angle. The flow appears not to be fully established within this range of operation: This anomaly may have resulted from local flow separations or transient flow behavior. At a given inlet contraction ratio, the $L_c/H_{th} = 6.25$ cowl possesses a stronger cowl shock than shocks for cowl lengths of 9.75 and 11.00. For the $L_c/H_{th} = 11.00$ cowl (fig. 11), a much more systematic increase in pressure occurred through the inlet as the convergence angle increased for both the thin and thick boundary-layer configurations. This same characteristic is also true for the $L_c/H_{th} = 9.75$ cowl.

Inlet Throat Flow Properties

Development of inlet flow model. To delineate the isolator performance from the inlet performance, the flow properties at the inlet throat plane must be determined for each inlet configuration. From a one-dimensional-flow point of view, one typically employs the measured area-averaged throat static pressure (p_{th}/p_1), the inlet throat geometric area (A_{th}), and the inlet entrance flow conditions in order to calculate the throat Mach number and total pressure recovery (for a given cowl length and angle). Because the internal aerodynamic throat area is smaller than the internal geometric area, as a result of the inlet boundary-layer blockage, this approach would predict an inlet throat Mach number and a total pressure recovery that are lower than the actual inlet throat values.

In light of the above statements, the aerodynamic throat area had to be determined in order to evaluate the isolator performance. Because no pitot measurements were obtained at the inlet throat, a two-dimensional analysis was employed. This analysis consisted of computing the two-dimensional shock strength necessary to obtain the measured ramp and cowl surface static pressures. Consistent with the data, a flow turning angle of approximately 12° was produced by the combined 11° ramp-wedge angle and the boundary layer. (See fig. 5.) The amount of the internal contraction within the inlet, inclusive of boundary-layer effects, was obtained by determining the required turning strength of the cowl shock waves (which would be necessary to produce area-averaged inlet throat pressure). Note the simplifying assumption that the turning strength of each shock reflection was not influenced by the boundary layer.

The number of shock reflections was based on two-dimensional inviscid calculations, and their actual turning strengths were adjusted in order to match the measured area-averaged inlet throat pressure. For the short $L_c/H_{th} = 6.25$ cowl configuration (see fig. 5(a)), the shock wave reflected from the ramp and impinged on the cowl upstream of the inlet throat plane. In this case, the area-averaged throat pressure used in the analysis was the measured pressure on the ramp surface just upstream of the corner. For the $L_c/H_{th} = 9.75$ cowl configurations (see fig. 5(b)), the inlet throat pressure used in the analyses was obtained on the cowl surface opposite the ramp corner. (This analytic throat pressure compares closely with the value obtained by subjecting the flow to one additional shock reflection of identical strength.) The same technique was used to select the area-averaged static pressure location for the throat of the inlet with the $L_c/H_{th} = 11.00$ cowl (fig. 5(c)); however, the shock reflection impinged on the ramp corner located beyond the inlet geometric throat (i.e., slightly into the isolator section). Thus, the selection of the inlet throat static pressure required more information. An examination of the sidewall pressure at the inlet throat region showed that approximately one-third of the flow at the inlet throat plane lay behind the reflected third shock wave, and two-thirds lay in front of the wave. Thus, these weighting factors were used in determining an area-averaged value from the measured inlet throat static pressure. The measured inlet throat static pressure versus the inlet contraction ratio for both thin and thick boundary layers are detailed in figure 12.

Once a representative measured area-averaged throat pressure and the subsequent two-dimensional shock pattern for each inlet were obtained, the throat Mach number, total pressure recovery, and effective aerodynamic contraction ratio were calculated.

Calculated inlet throat flow properties. Figure 12 shows that the short 2.5-in. cowl length produced only a limited operational contraction ratio range, and that the inlet throat static pressure was nearly a linear function of the inlet contraction ratio. Calculated throat flow properties and parameters are plotted in figures 13–15. For known inlet incoming flow properties, the 1-D analytical inviscid calculation dictates that the inlet throat properties have to remain the same regardless of inlet cowl length for the same inlet contraction ratio. Therefore, one can conclude that the discrepancies between inlet throat thermodynamic properties between different cowl lengths at the same inlet contraction ratio are a measure of boundary-layer effects (3-D) and flow distortion at the

inlet throat. The viscous boundary layer and inlet throat flow distortion are different and unique to each cowl setting. In general, because of increasing shock strength with increasing convergence angle, the inlet throat total pressure recovery (fig. 14) decreases with the decrease in the inlet throat Mach number (fig. 13). The results indicate that the longer cowls have a slightly higher throat pressure recovery across the spectrum of inlet contraction ratio. Figure 15 shows the combined effects of boundary layer and inlet throat distortion on the aerodynamic throat area. The aerodynamic throat area decreases with increasing contraction ratio for the $L_c/H_{th} = 6.25$ cowl but increases with increasing contraction ratio for the two larger cowls.

Inlet Unstart and Restart Characteristics

The inlet unstart phenomenon is a result of the disgorgement of a shock system from the inlet throat station to a station just upstream of the cowl leading edge in order to spill air. The inlet unstart manifests itself experimentally by a sudden increase in static surface pressure upstream of the cowl leading edge. Two distinct causes of inlet unstart are as follows: (1) the formation of a separated flow in the inlet that forms as a result of the inlet convergence being too great and the shocks interacting in the form of glancing and incident shocks on sidewall and body-side boundary layers, respectively, and (2) excessive back pressuring due to a simulated combustor pressure rise pushing a shock train forward within the isolator toward the inlet throat, and then finally disgorging out the inlet.

To relate the formation of separated flow in the inlet to inlet unstart, we must examine the inlet unstart data for each cowl geometry. Figure 16 shows the inlet unstart and restart convergence angle for each cowl length with both thin and thick incoming boundary layers. In general, the repeatability of inlet unstart and restart convergence angle varies within a small range for each cowl length. All inlet unstarts occurred between 9° and 10.5° for the thin boundary-layer configurations, and between 8.2° and 9.4° for the thick, incoming inlet boundary-layer configurations, irrespective of cowl length and inlet contraction ratio. Korkegi's model (ref. 11) shows that turbulent boundary-layer incipient separation due to skewed (glancing) shock-wave interactions occurs at a local Mach number of 3.1 when the shock-wave flow turning angle is 7.0°, although Kuehn (ref. 12) indicates flow separation would occur for shock turning angle of 8.3°. For this study, flow separations large enough to cause inlet unstart occurred at a slightly higher shock turning angle. The triggering of inlet unstart, when each cowl reaches about the same convergence angle, indicates that the inlet flow boundary-layer interactions for inlet unstart are independent of inlet contraction ratio or mass capture. (Contraction ratio and mass capture for the inlet are higher by 35 percent for the $L_c/H_{th} = 11.00$ cowl than for the $L_c/H_{th} = 6.25$ cowl.) Thus, when the inlet unstart occurs, the only prevalent similarity between each inlet with a different cowl length is the same convergence angles or shock flow turning angles. This suggests that the interaction of the cowl shock with the inlet boundary layer is critical, and this interaction creates a separated flow that unstarts the inlet. The cowl shock is swept (glancing) and 3-D on the inlet sidewalls, and it is incident and 2-D on the body side. Note that according to existing research literature (refs. 13–15), the 3-D interaction of a glancing shock system with a boundary layer is more sensitive to shock-turning angle than the 2-D interaction.

Figure 17 shows that the inlet unstart pressure load distribution increases on both the inlet ramp and the cowl with increases in cowl length. The thick-boundary-layer experimental results (with foreplate) show that the unstart load distribution is essentially the same as that for the thin boundary layer (without foreplate) on both the cowl and the compression ramp.

The other type of inlet unstart addressed in this study is due to back pressure. The combustor pressure rise forces a shock with high strength upstream toward the throat of the model; this marks the maximum back-pressure limit that the inlet can withstand before the onset of the inlet unstart. The degree of maximum sustainable combustor pressure rise, before the onset of the inlet unstart, depends on inlet geometry, contraction ratio, and isolator length. Back-pressure unstarted pressure distributions throughout the inlet flow path are shown in figure 18.

Comparing figures 17 and 18 shows that the unstarted pressure distribution throughout the inlet for inlet unstart due to convergence angle remains at the same magnitude as the inlet unstarted pressure distribution due to excessive back pressure (ultimately resulting in identical unstart mechanisms).

Figure 16 also shows the inlet restart (swallow the shock system) characteristics for both thin and thick incoming boundary layers. For a thin boundary layer, the range of inlet restart convergence angle varied from about 4.5° for the $L_c/H_{th} = 6.25$ cowl to about 3.0° for the $L_c/H_{th} = 11.00$ cowl, and yielded inlet geometric internal contraction ratios $(CR)_i$ of about 1.44 to 1.31, respectively. The effects of the thick boundary layer with a foreplate reduced the inlet restart convergence angle variation for each cowl by about 0.5°. Inlet restart occurs when the inlet geometric internal contraction ratio is low enough to pass the entrance mass flow at a total pressure that corresponds to the value behind a normal shock at the entrance inlet Mach number of 3.1. Kantrowitz and

Donaldson (ref. 16) showed that the maximum, inviscid, geometric internal contraction ratio for an incoming flow at $M = 3.1$ is $(CR)_i = 1.40$ in order to restart a supersonic inlet (with $\gamma = 1.4$) compared with values of $(CR)_i = 1.4$ and 1.31 obtained experimentally from this test series. Additionally, from the multitude of different inlet sizes and shapes tested in various tunnels, Mahoney (ref. 10) empirically determined the restart internal contraction ratio limit as a function of inlet incoming Mach number for supersonic inlets. Mahoney's empirical determination shows a restart contraction ratio of 3.2 for an approaching inlet Mach number of 3.1, which is in agreement with this experimental study.

An examination of the unstart and/or restart data (not shown here) for each cowl for a variety of downstream configurations suggests that the spread in inlet unstart and/or restart data is not configuration dependent (i.e., isolator lengths and steps); however, the data spread is more pronounced for the inlet with the short cowl ($L_c/H_{th} = 6.25$) than for inlets with medium ($L_c/H_{th} = 9.75$) and large ($L_c/H_{th} = 11.00$) cowls. The larger spread in data, for the short cowl, might be attributed to the larger flow distortion entering the isolator.

Isolator Back-Pressure Characteristics

During the ramjet operational mode of an air-breathing engine, the diffusion process takes place through consecutive supersonic and subsonic diffusion processes. The transition from supersonic to subsonic flow occurs in the isolator section through a complex shock-train interaction with the wall boundary layer. The required isolator length to contain a full shock-train length depends on isolator entrance flow properties and downstream combustor pressure. If the isolator is not of sufficient length to contain the full shock train before the flow enters the combustor section, the diffusion process would be incomplete, which would cause a decrease in the amount of diffusion and pressure recovery. The combination of flow distortion (skewed) and shock–boundary-layer interaction makes a 3-D numerical solution approach (full Navier-Stokes) very challenging. Thus, experiments were conducted to investigate the pressure distribution throughout the isolator and to determine the upper pressure threshold that is sustainable in the isolator section before unstarting the inlet. Test results include the combined effects of distorted (skewed) isolator inflow conditions generated by a supersonic inlet and simulated combustion effects downstream of the isolator via back pressuring of the model with the throttling device.

As noted previously, two inlets with different cowl lengths, but with the same convergence angle, possess different shock strengths and different isolator inflow properties (i.e., Mach number, mass capture, pressure, and distortion) at the inlet throat. Thus, from figures 19–24, direct isolator performance comparisons between two inlets with the same convergence angles and isolator lengths should not be inferred due to mass flow and isolator entrance Mach number variations.

The effects of gradually increased back pressure on the static pressure distribution along the centerline of the inlet isolator and combustor nozzle on the body side and cowl side are shown in figures 19–24 for the $L_c/H_{th} = 6.25$, 9.75, and 11.00 cowls (i.e., the 2.5-, 3.9-, and 4.4-in. lengths, respectively). The $L_c/H_{th} = 6.25$ and 11.00 cowl configurations include data for isolator length ratios (L/H_{th}) of 2.7, 4.7, 8.7, and 16.7; data for the $L_c/H_{th} = 9.75$ cowl are presented only for $L/H_{th} = 4.7$. In addition, the constant-area isolator length of $L/H_{th} = 4.7$ was mated to a 6° divergent section on the body side to investigate the effects of a low-divergent-angle isolator section on combustor back pressure for the $L_c/H_{th} = 6.25$ and 11.00 cowl configurations. The constant-area length of isolator and diffuser combined is approximately 16 throat heights (i.e., $L/H_{th} = 16$). The pressure distributions are nondimensionalized by the nozzle-exit static pressure (p_1) of the free-stream tunnel. For each cowl length, the results are presented for a large inlet convergence angle (representing the largest inlet compression achieved), the maximum possible inlet capture for that configuration before unstarting the inlet, and a medium convergence angle.

The inlet would operate somewhere within these two inlet convergence angles for optimum integrated inlet-vehicle performance. For each inlet convergence angle, results on different-length isolators represent the effect of a partial shock train and the progression toward a fully contained shock train with increases in isolator length. Each figure in this section shows a gradual progression of pressure rise and back-pressure influence upstream throughout the inlet-isolator flow path, starting from a minimum and gradually progressing to a maximum throttling back pressure before unstarting the inlet. Figures 19–24 also show that back pressuring separated the flow downstream of the 20° nozzle expansion and caused the pressure to become constant starting at the nozzle expansion corner. The minimum and maximum throttling back pressures simulate the effects of no-combustion heat release and maximum-combustion heat release that can be added in the combustor without unstarting the inlet. The value of the percentage of the isolator normal shock pressure recovery was calculated using inlet throat conditions. These data inlet throat Mach number, and normal shock pressure values are presented with each figure.

Figures 19 and 20 show shock-train progression and the simultaneous rise in pressure distribution upstream in the isolator with back pressure for the $L_c/H_{th} = 6.25$ short cowl at inlet convergence angles of $8.5° \pm 0.3°$ (high convergence angle) and $5.5° \pm 0.5°$ (medium convergence angle) with inlet throat Mach numbers of 2.27 ± 0.02 and 2.40, respectively. The inlet throat Mach number and the normal shock pressure were calculated based on the isolator inflow Mach number and static pressure at the shoulder. Figures 19(a)–19(f) and 20(a)–20(f) show that the maximum static pressure rise on the body side and cowl side increases with isolator lengths from $L/H_{th} = 2.7$ to 8.7. The continuous rise in isolator maximum pressure with isolator length indicates the progression of the partial shock train to containment of the full shock train with increased isolator length. However, the gain in pressure rise levels off with a further increase in isolator length beyond 8.7. The shock train is considered fully contained within the isolator if a further addition of isolator length does not continue to increase the pressure level within the isolator. If the isolator length is shorter than the shock-train length, the pressure decreases rapidly with decreasing isolator length. If the isolator length is longer than the shock-train length, the additional viscous losses decrease the maximum pressure recovery only gradually with increasing isolator length. This becomes evident when comparing figure 19(e) with 19(g) and figure 20(e) with 20(g). An isolator length of 8.7 was sufficient to achieve a maximum pressure recovery for both high and medium inlet convergence angles at these particular isolator inflow conditions. However, the maximum pressure rise for the high and medium inlet convergence angles is only 63 percent and 71 percent of inlet throat normal shock pressure, respectively. For the $L_c/H_{th} = 6.25$ cowl, the large isolator inflow distortion may be a cause in reducing the isolator pressure rise.

The 6° expanding section added to the constant-area isolator length of $L/H_{th} = 4.7$ yields a total isolator length equivalent to $L/H_{th} = 16.0$. The 6° expanding section was added to examine the maximum back-pressure capability of an expanding diffuser flow as compared with a flow of constant area with the same equivalent isolator length. Figures 19(i) and 20(i) show that the addition of the 6° divergent section reduces the diffusion of the flow. This fact is evident from comparing the pressure rise in figure 19(g) with 19(i), and in figure 20(g) with 20(i). The pressure rise slope is steeper in the constant-area diffuser than in the 6° expanding section. As compared with the constant-area isolator, the differential Mach number in the expanding 6° diffuser section is higher, which consequently, results in a decrease in shock-angle distribution within the expanding 6° diffuser section. Smaller shock angles associated with the higher Mach number increase the shock-train length as compared with the constant-area duct of the same length. Thus, higher shock losses lower total pressure recovery and decrease the maximum pressure rise before inlet unstart. However, the 6° expanding isolator does diffuse the flow as opposed to the 20° expanding section, which separates and provides minimal additional back-pressure capability.

The $L_c/H_{th} = 9.75$ cowl was tested only with the constant-area isolator length of 4.7 (figs. 21 and 22). The inlet convergence angles were 9.8° with an inlet throat Mach number of 1.70 and 5.8° with an inlet throat Mach number of 2.15. Because of reasons noted previously, this inlet was expected to have a minimum distortion level at the inlet throat in comparison with the configuration having $L_c/H_{th} = 6.25$ and 11.00 cowls. The $L_c/H_{th} = 9.75$ inlet cowl with the $L/H_{th} = 4.7$ isolator produced a shock-train system in which the isolator maximum pressure rise was 67 percent and 50 percent of the normal shock pressure rise associated with the throat Mach number at the inlet convergence angles of 9.8° and 5.8°, respectively. Comparable values for the $L_c/H_{th} = 6.25$ cowl at inlet convergence angles of 8.4° and 6° with a constant-area isolator length of $L/H_{th} = 4.7$ are 47 percent and 46 percent, respectively.

Figures 23 and 24 also show an isolator pressure distribution for the $L_c/H_{th} = 11.00$ inlet cowl at convergence angles of $9.55° \pm 0.25°$ and 6.1° with inlet throat Mach numbers of 1.74 ± 0.03 and 2.14, respectively. The pressure levels are somewhat higher throughout each isolator with the $L_c/H_{th} = 11.00$ cowl than with the $L_c/H_{th} = 9.75$ cowl. Again, the maximum pressure level in the isolator was about the same for isolator lengths of 8.7 to 16.7. (See, e.g., figs. 23(e) and 23(g), and figs. 24(e) and 24(g).)

Other experimental data (not shown) indicate that the addition of the forebody boundary-layer plate and sudden area changes in the isolator (steps) slightly reduce the isolator maximum pressure level. However, the general pressure distribution characteristics throughout the isolator remained unchanged. The maximum isolator pressure rise for both the thin and thick boundary layers is summarized in the next section.

Maximum Capability of Inlet-Isolator Maximum Back Pressure

Figures 25–27 show the maximum inlet-isolator pressure rise on the body side (p_s/p_1) that each isolator was able to sustain before the inlet unstarted. The maximum inlet-isolator back pressure is an implicit interdependent parameter between the inlet and the

isolator. This parameter is significant only if the combined performance of the inlet and the isolator as a single unit is under evaluation. When evaluating the inlet-isolator combination as a single unit, one must remember that the maximum obtainable pressure rise in the isolator is a function of both inlet contraction ratio and isolator length. As explained previously, the degree of inlet contraction ratio depends on the inlet cowl length and angle, and the shock-train containment in the isolator depends on the physical isolator length. At a fixed inlet contraction ratio, the relative impact of an increase in incremental isolator length on the maximum back pressure before unstart can be examined in figures 25, 26, and 27 for the L_c/H_{th} = 6.25, 9.75, and 11.00 cowls, respectively.

Figure 25(a) demonstrates the general trends of increased maximum back pressure with increased inlet contraction ratio. Supersonic inlet throat conditions at the inlet shoulder are a strong function of inlet contraction ratio and distortion level (due to cowl length and angle). Thus, for a fixed inlet contraction ratio, the relative increase in maximum inlet-isolator pressure with isolator length is solely attributed to the extent of the containment of the shock train within the isolator. Figure 25(a) also shows that the increase in the maximum inlet-isolator pressure rise is negligible with the addition of isolator length (L/H_{th}) from 8.7 to 16.7, indicating that the shock train is fully contained within isolator lengths of 8.7 throughout the full range of inlet contraction ratio. For each isolator length, the maximum inlet-isolator pressure rise was always at about the same level below the calculated rise in normal shock pressure across the full range of inlet contraction ratio. The L_c/H_{th} = 6.25 cowl inlet shows the same general trends with a thick boundary layer (fig. 25(b)) as with a thin boundary layer (fig. 25(a)), but with a lower maximum inlet-isolator pressure rise. The forebody plate introduced a thick boundary layer which further added to the distortion level of an already skewed flow at the inlet throat, which in turn caused higher inlet losses throughout the range of inlet contraction ratio.

Figures 26 and 27 show that the maximum inlet-isolator pressure rise for inlets with the L_c/H_{th} = 9.75 and 11.00 cowls, respectively possesses the same general trends as that for the L_c/H_{th} = 6.25 cowl (fig. 25). The maximum inlet-isolator pressure rise continues to increase over the broad range of inlet contraction ratio attainable with the longer cowls.

Effects of Inlet Flow Distortion on Inlet-Isolator Maximum Pressure

The losses in the inlet are a cumulative combination of inlet inviscid shock losses, viscous and shock boundary-layer interaction losses, and flow profile distortion losses. The relative magnitude of these losses varied with each cowl length. (See the inlet throat flow properties in fig. 14 for the total pressure recovery.) For an isentropic compression inlet with known entering flow properties, the compression process is primarily a function of inlet contraction ratio. For a fixed inlet contraction ratio, the isentropic inlet throat properties would be the same in spite of cowl length. Here, the fact that the inlet throat properties vary for each inlet cowl length for the same inlet contraction ratio is reflective of losses that are inherent but different in magnitude for each inlet cowl. When comparing configurations that have different inlet cowl lengths but the same inlet contraction ratios, one is reminded that the amount of mass flow is fixed throughout the flow path of each configuration.

For a configuration with a common isolator length, the inlet losses attributed to a specific inlet cowl length were quantified in terms of the relative impact of those losses on inlet-isolator maximum pressure capability for a full range of inlet contraction ratios (figs. 28–32). The maximum inlet-isolator pressure in figures 28–32 varied with each cowl length for a fixed inlet contraction ratio, which is reflective of those cumulative losses and the inlet throat distortion just noted herein.

Figure 28(a) shows the inlet-isolator maximum pressure rise for the L_c/H_{th} = 6.25 and 11.00 cowls mated with an L/H_{th} = 2.7 throat height with constant-area isolator length. The L_c/H_{th} = 6.25 cowl rendered the lower maximum pressure rise before inlet unstart. To maintain the same contraction ratio, the shorter cowl must have a greater incidence angle to the free-stream flow. Thus, the flow entering the isolator section for the L_c/H_{th} = 6.25 cowl had a higher loss (due to a greater flow turning angle) and distortion level at the throat than the L_c/H_{th} = 11.00 cowl. The high inlet losses of the L_c/H_{th} = 6.25 cowl length when combined with losses due to the incomplete shock-train containment of the L/H_{th} = 2.7 throat height reduced the inlet-isolator maximum pressure capability across the inlet contraction ratio range. Figures 29(a)–32(a) show that the shock train was further contained with the increase in isolator length, which led to a higher back-pressure capability.

Configurations with thick boundary layers, such as those shown in figures 28(b)–31(b) (fig. 32(b) has insufficient data available), show the same general trends as the configuration with a thin boundary layer. Also, with the thick boundary layer, the inlet-isolator maximum pressure rise for the L_c/H_{th} = 6.25 cowl was near the value obtained with the L_c/H_{th} = 11.00 cowl for isolator lengths (L/H_{th}) of 8.7–16.7 geometric throat heights (figs. 30(b) and 31(b)).

The sudden step area increase in the isolator is intended to replicate the location of fuel injectors during

operation. Figures 29(c)–29(f) show the effects of a step area increase of 20 percent (rearward-facing steps) on the inlet-isolator maximum pressure rise for the $L/H_{th} = 4.7$ isolator. The presence of the step area increase lowered the maximum pressure rise in the $L_c/H_{th} = 4.7$ isolator. The impact of the step area increase on isolator maximum pressure rise was more pronounced for the $L_c/H_{th} = 6.25$ configuration with the thin boundary layer than for the same configuration with the $L_c/H_{th} = 11.00$ cowl. This is evident when comparing constant-area isolator results (fig. 29(a)) with the isolator having a rearward-facing step (a sudden area increase) (figs. 29(c) and 29(e)).

Isolator Effectiveness

To separate isolator effectiveness from the combined inlet-isolator performance, the maximum sustainable pressure rise in the isolator (p_s) for any given inlet contraction ratio was divided by the inlet throat static pressure (p_{th}) at the junction of the inlet and isolator. Evaluating the effectiveness of an isolator as a single component, independent of the inlet, is of significance during the course of a design process when assessing the contribution of various isolator lengths to the overall vehicle performance level (i.e., installed thrust). The incremental vehicle aerodynamic performance gain, obtained from the various isolator lengths with different isolator inflow conditions, would then be traded against the adverse impact of isolator dry weight on vehicle takeoff gross weight (TOGW) over the integrated flight trajectory.

Figures 33–35 show the effectiveness of four different isolator lengths in terms of the pressure ratio (p_s/p_{th}). The figures show that, in general, the isolator effectiveness decreases with increasing inlet contraction ratio. However, one must note that the decrease in isolator effectiveness for any given inlet cowl and isolator length is expected because the Mach number at the inlet throat or isolator entrance decreases with increasing inlet contraction ratio; consequently, a reduction in Mach number at the isolator entrance also reduces both the normal shock pressure rise and the pressure rise in the isolator due to back pressuring.

The isolator effectiveness with inlet contraction ratio can also be related to combustion heat release and, consequently, the maximum permissible combustion heat release is one that generates a combustion pressure rise consistent with the isolator maximum pressure capability and still avoids unstarting the inlet. It can be inferred from figures 33–35 that the fuel equivalence ratio required to unstart the inlet decreases with increasing inlet contraction ratio. This behavior is consistent with Rayleigh flow in which the amount of heat (i.e., combustion heat) necessary to generate a normal shock in the isolator section is lower for low-supersonic isolator inflow Mach numbers created by high inlet contraction ratios. However, the amount of combustion that can be accomplished in a larger downstream area is more a function of the absolute pressure level that can be contained by the inlet-isolator combination.

Figures 33–35 also reveal that isolator effectiveness decreases more rapidly with inlet contraction ratio for the short inlet cowl (fig. 33) than for the same isolator configurations with long cowls (figs. 34 and 35). In addition, in the thin-boundary-layer tests (solid symbols), configurations with a short cowl possess a higher isolator effectiveness (isolator pressure rise) than those with the long cowl. The sharp decrease in isolator effectiveness with inlet contraction ratio for the configuration with the short cowl can be attributed to the effect of inlet diffusion and the degree of inlet flow distortion. Thus, the isolator effectiveness data suggest that in the case of the short cowl, in which flow distortion and high inflow Mach number to the isolator section are prevalent, the isolator plays a major role in the diffusion of the flow in the isolator with back pressuring. However, for the inlet-isolator configurations with longer cowls, the isolator effectiveness would gradually phase out and further diffuse the flow in the isolator section.

The data presented in figures 33–35 for given inlet geometries and isolator lengths are of eminent value to optimize the integration of the inlet and isolator geometries in the design of lifting-body hypersonic vehicles in order to obtain the proper combustor pressure rise with minimum structural weight.

Conclusions

Combinations of different constant-area isolator lengths, with and without rearward-facing steps, were coupled to a supersonic inlet with three different rotating cowl lengths to investigate the maximum isolator pressure rise. The results in this report explore the operational characteristics of various inlet/isolator configurations in terms of pressure rise in the isolator. Test results for inlet and isolator coupling provide a novel parametric state-of-the-art database that is necessary for the design of a hypersonic vehicle, and this enables the use of a cycle deck to predict inlet-isolator performance over the ramjet envelope. In conclusion, the salient features observed from this study include the following:

1. The examination of static pressure measurements obtaining at the inlet geometric throat (inlet-isolator junction) showed that depending on the inlet cowl length, the interaction of the cowl shock with the expanding waves at the compression ramp shoulder generated various levels of flow distortion which impacted the isolator

performance. The inlet throat distortion level was at a maximum for the short cowl, which had a limited range of inlet contraction ratio and a high isolator entrance Mach number. The inlet throat distortion level entering the isolator was minimized by a cowl length that focused the cowl shock on the ramp shoulder.

2. The addition of a boundary-layer plate to simulate the thicker turbulent boundary layer (from $0.25H_{th}$ to $0.55H_{th}$, where H_{th} denotes the inlet throat or isolator entrance height) of the forebody of a hypersonic vehicle reduced the maximum operational inlet convergence angle by approximately 1.4°, and correspondingly the maximum operability of the inlet contraction ratio was reduced by about 5 percent.

3. An examination of the pressure distribution throughout the inlet showed that independent of isolator length, the inlet pressure distribution reached a maximum near the inlet geometric throat on both the body and cowl sides for any inlet convergence angle above 5° for long cowls (i.e., $L_c/H_{th} = 9.75$ and 11.00, where L_c denotes the inlet cowl length), and above 7° for the short cowl (i.e., $L_c/H_{th} = 6.25$). This indicated that within their limits, the location of the inlet aerodynamic throat area coincided with the inlet geometric throat.

4. Data showed that the inlet unstarted at approximately the same convergence angle despite inlet cowl length and inlet contraction ratio. This result indicates that the shock boundary-layer interactions were the mechanism for inlet unstart independent of inlet contraction ratio and mass capture.

5. The inlet unstart load (unstart drag) reflected by a higher pressure level increased on both the inlet ramp and the cowl with an increase in cowl length. The thick-boundary-layer experimental results (with foreplate) also showed the unstart pressure distribution to be about the same as that of the thin boundary layer (without foreplate).

6. The shock train was considered to be fully contained within the isolator if further addition of isolator length did not continue to increase the isolator pressure level. If the isolator length was shorter than the shock-train length, the maximum value of back pressure before inlet unstart decreased rapidly with decreasing isolator length. The results also showed that if the isolator length was longer than the shock-train length, the additional viscous losses decreased pressure recovery gradually with increasing isolator length. Optimal isolator length (L/H_{th}) was 8.7, where L denotes the isolator length.

7. When evaluating the inlet-isolator model as a single unit, the combination of inlet and isolator caused the maximum pressure rise in the isolator to increase with inlet contraction ratio and isolator length before unstarting the inlet.

8. An increase in the step rearward-facing area of 20 percent reduced the inlet-isolator maximum back-pressure rise before inlet unstart, as opposed to the same configuration with constant-area isolator length. This result was more pronounced for the short $L_c/H_{th} = 6.25$ cowl than for the same isolator configuration with the long $L_c/H_{th} = 11.00$ cowl.

9. The sharp decrease in isolator effectiveness with increasing inlet contraction ratio for the configuration with a short inlet cowl indicated that the isolator played a major role in the diffusion of the flow in the isolator. However, for the inlet-isolator configurations with longer cowls, the isolator effectiveness gradually phased out further diffusion of the flow in the isolator section, thus diminishing the need for further reliance on an extended isolator section.

10. Isolator effectiveness data showed that the required combustion heat release for inlet unstart increased with increasing inlet contraction ratio because the amount of combustion that can be accomplished in a larger downstream area is a function of the absolute pressure level that can be contained by the combined inlet-isolator model.

NASA Langley Research Center
Hampton, VA 23681-0001
February 14, 1995

Appendix

Inlet Performance Definitions

The inlet used in this experiment was designed to compress the approaching supersonic air (M = 4.03) externally and internally at subcritical mode. In all test cases, the external compression process was accomplished by a ramp shock at a wedge angle of 11° that simulated a portion of a hypersonic vehicle forebody (fig. A1). The inlet internal compression was achieved via a combination of several reflective oblique shock waves (initiated by the cowl) and was contained by surfaces that were contracted two dimensionally in the lateral direction. The oblique shock waves reflected from the compression ramp and cowl progressed toward and into the geometric throat ($A_{th} = H_{th}W$), with the number of reflections dependent on the inlet cowl length. The projected frontal stream tube area of the inlet is often referred to as the "captured stream tube area" ($A_{cap} = H_{cap}W$). The number of shock reflections and the magnitude of the projected frontal stream tube area directly depend on the cowl length (L_c), cowl angle position (θ_c), precompression-ramp wedge angle (α), and shock-wave angle (θ_w).

One parameter that governs the inlet performance is based on the inviscid stream tube area captured by the inlet (A_{cap}). Flow visualization of the surface oil on the inlet body side showed that the flow was mainly two dimensional throughout the body side of the inlet. The two dimensionality of the flow and the constant width (W) of the model flow path justify the simplification that the captured area is equal to the product of captured height (H_{cap}) and model width. Because of the boundary layer on the ramp, the actual captured stream tube is reduced to less than the inviscid stream tube. The integrated boundary-layer displacement thickness (δ^*) obtained from the ramp pitot pressure measurements behind the wedge shock immediately upstream of the inlet entrance was used to calculate the actual captured stream tube from that of the inviscid capture area. A relationship was derived to relate the inlet inviscid captured height to the inlet geometry and compression shock-wave angle. Thus, from the schematic diagram in figure A1, we derive

$$H_{cap} = L_r \tan\alpha - L_c \sin\theta_c + H_{th} + \frac{\tan\alpha \ \tan\theta_w}{\tan\alpha - \tan\theta_w} \times \left[L_r\left(1 - \frac{\tan\alpha}{\tan\theta_w}\right) + L_c\left(\frac{\sin\theta_c}{\tan\theta_w} - \cos\theta_c\right) - H_{th}\left(\frac{1}{\tan\theta_w}\right)\right] \quad \text{(A1)}$$

Additionally for any given inlet cowl length and inlet cowl angle, the height of the flow path at the cowl leading edge (H_g) is also related to H_{cap} through a constant derived from the geometric relation

$$H_{cap} = 1.876 H_g \quad \text{(A2)}$$

Thus, the same geometric relation was also used to account for the effect of boundary-layer displacement thickness on the inlet mass deficit, yielding

$$H_{cap,\,act} = H_{cap} - 1.876\delta^* \quad \text{(A3)}$$

Inlet aerodynamic contraction ratio ($(CR)_a$), and inlet mass capture ratio (CAP) usually describe the inlet performance. Here, the inlet contraction ratio is defined as the ratio of the actual projected area of the inlet frontal stream tube (parallel to the free stream) to the inlet geometric throat area, and the inlet mass capture ratio is defined as the ratio of mass flow rate actually passing through the inlet to that approaching the projected frontal model area ($A_m = H_m W$). These parameters are given, respectively, as

$$(CR)_a = \frac{A_{cap}}{A_{th}} = \frac{H_{cap,\,act}}{H_{th}} \quad \text{(A4)}$$

$$CAP = \frac{H_{cap,\,act}}{H_m} \quad \text{(A5)}$$

The substitution of each cowl length, the cowl angle positions, and the compression shock-wave angle for a given wedge angle at any approaching flow Mach number in equations (A1) and (A3) would render the actual captured height. Inlet $(CR)_a$ and CAP can be calculated from equations (A4) and (A5), where H_{th} and H_m are invariable inlet throat geometric dimensions throughout the course of these test series. Figures A2 and A3 show the inlet $(CR)_a$ and CAP versus inlet convergence angle (β) for 4.4, 3.9, and 2.5 in. inlet cowl lengths for cowl angle variations from 0° to 11°. The

compression wedge angle of 11° and the Mach number approaching 4.03 remained the same for all calculations. From figure A1, the relationship between cowl angle (θ_c) and cowl convergence angle (β) is

$$\beta = 11° - \theta_c \tag{A6}$$

Inlet mass capture ratio was also used to calculate mass flow rate through the inlet for each cowl for the same range of convergence angles (fig. A4).

Another parameter often used to define the inlet is the geometric internal contraction ratio ($(CR)_i$) given as

$$(CR)_i = \frac{A_g}{A_{th}} = \frac{H_g}{H_{th}} \tag{A7}$$

The inlet mass capture ratio can also be related to free-stream and throat flow properties by equating the continuity equation at free-stream and throat conditions. This relationship can be expressed as

$$\frac{p_{t,\,cap,\,act}\left[\frac{p}{p_t}f(\gamma, M)\right]_{cap,\,act} A_{cap,\,act}}{\sqrt{T_{t,\,cap}}} = \frac{p_{t,\,th,\,a}\left[\frac{p}{p_{t,\,th,\,a}}f(\gamma, M)\right]_{th,\,a} A_{th,\,a}}{\sqrt{T_{t,\,th,\,a}}} \tag{A8}$$

where $f(\gamma, M)$ is given by

$$f(\gamma, M) = \sqrt{\frac{\gamma}{R}}\, M \left(1 + \frac{\gamma - 1}{2}M^2\right)^{1/2} \tag{A9}$$

Further manipulation of equation (A8) allows flow properties to be determined by recognizing that

$$T_{t,\,cap} = T_{t,\,th,\,a} = T_{t,\,1}$$

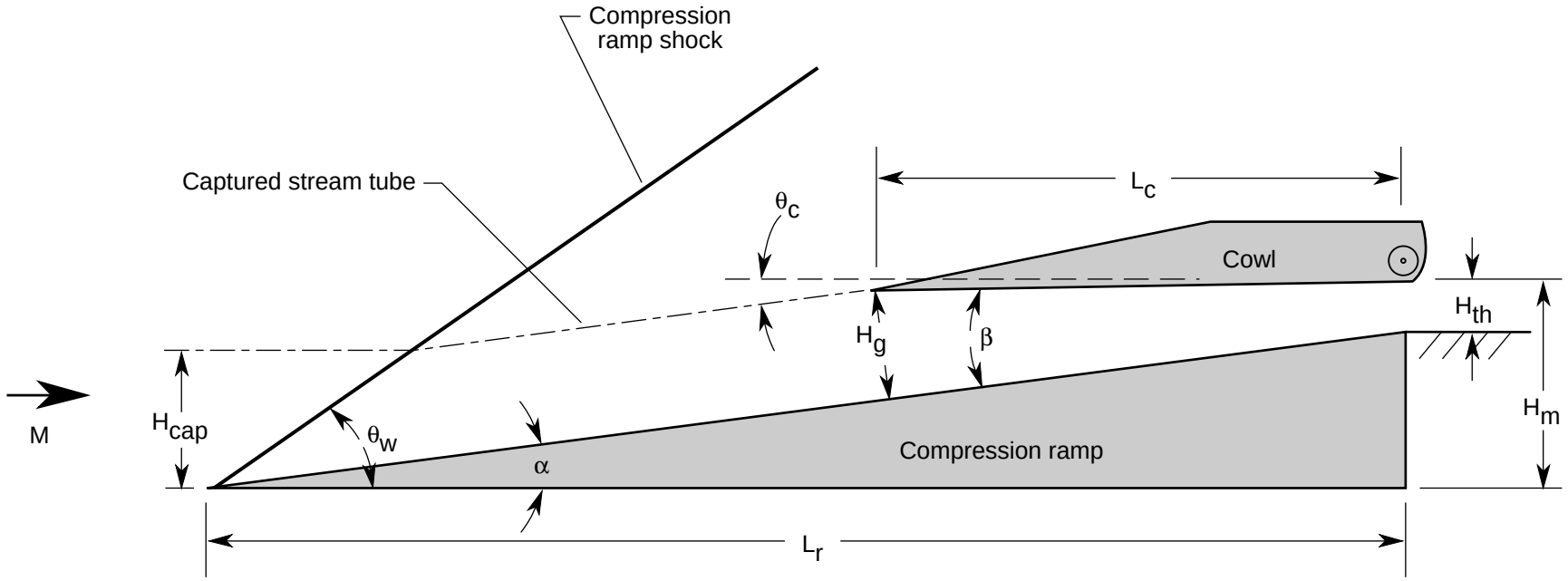

Inlet performance variables:

$H_{cap}/H_{th} \equiv$ Aerodynamic contraction ratio

$H_g/H_{th} \equiv$ Geometric internal contraction ratio

$H_{cap}/H_m \times 100 \equiv$ % of mass capture for given model height

Geometric test variables:

β = Inlet convergence angle

θ_c = Cowl angle with respect to horizontal

L_c = Cowl lengths 4.4" (L_c/H_{th} = 11.00), 3.9" (L_c/H_{th} = 9.75), and 2.5" (L_c/H_{th} = 6.25)

Fixed geometric values for all tests:

α = Compression ramp angle, 11°

H_{th} = Inlet throat height, 0.4"

L_r = Compression ramp length to inlet throat, 9.77"

θ_w = Shock-wave angle. For M = 4.03, θ_w = 23.043°

H_m = Model height, 2.3"

Figure A1. Schematic diagram of inlet geometry with inlet performance definitions.

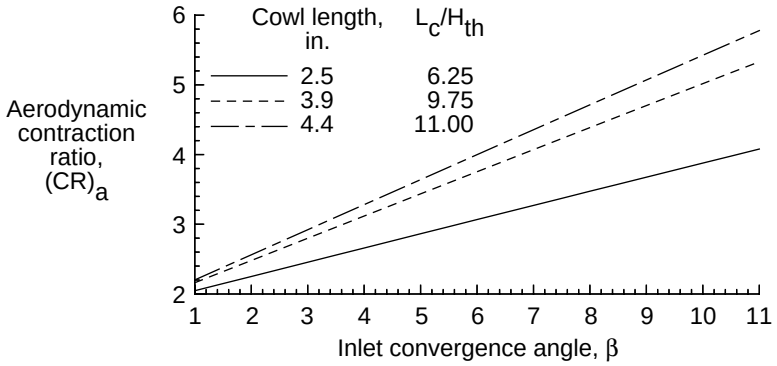

Figure A2. Aerodynamic contraction ratio versus inlet convergence angle.

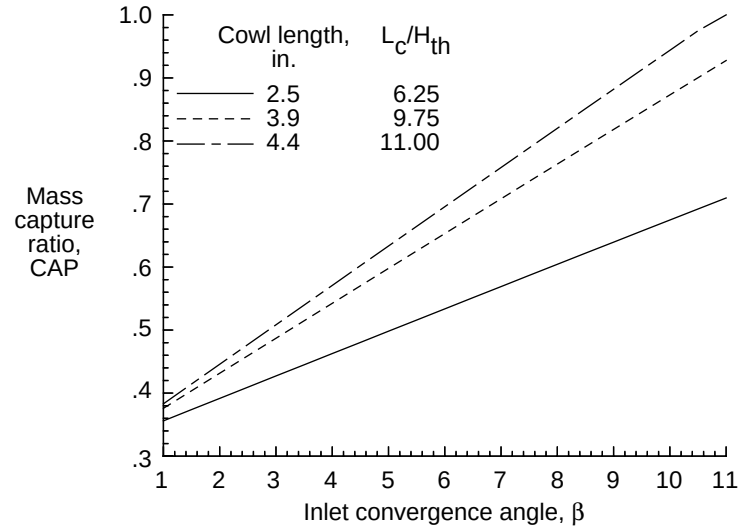

Figure A3. Inlet theoretical mass capture ratio versus inlet convergence angle.

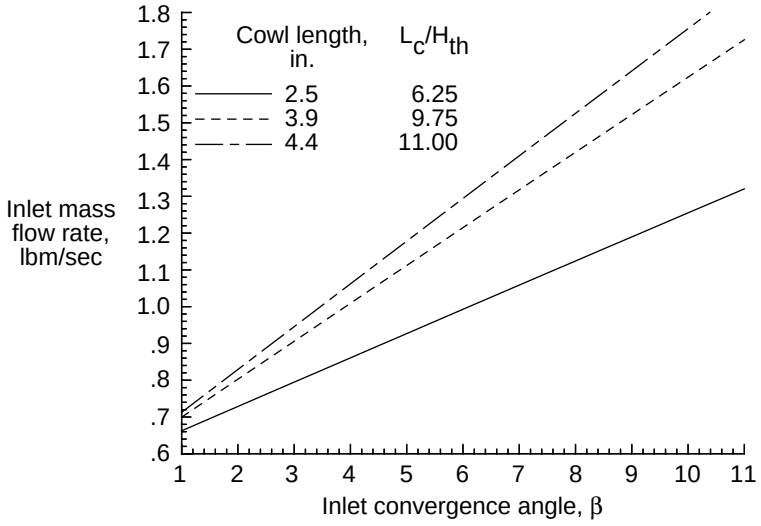

Figure A4. Inlet theoretical mass flow rate versus inlet convergence angle.

References

1. Billig, F. S.; Dugger, G. L.; and Waltrup, P. J.: Inlet-Combustor Interface Problems in Scramjet Engines. *1st International Symposium on Air Breathing Engines.* Institut de Mechanique des Fluides, June 1972.

2. Pratt, David T.; and Heiser, William H.: Isolator-Combustor Interaction in a Dual-Mode Scramjet Engine. AIAA-93-0358, Jan. 1993.

3. McLafferty, G. H.; Krasnoff, E. L.; Ranard, E. D.; Rose, W. G.; and Vergara, R. D.: *Investigation of Turbojet Inlet Design Parameters*. Rep. R-0790-13, Res. Dep., United Aircraft Corp., Dec. 1955.

4. Hataue, Itaru: Computational Study of the Shock-Wave/ Boundary-Layer Interaction in a Duct. *Fluid Dyn. Res.*, vol. 5, Dec. 1989, pp. 217–234.

5. Lin, Pei; Rao, G. V. R.; and O'Connor, George M.: Numerical Investigation on Shock Wave/Boundary-Layer Interactions in a Constant Area Diffuser at Mach 3. AIAA-91-1766, June 1991.

6. Lin, Pei; Rao, G. V. R.; and O'Connor, George M.: Numerical Analysis of Normal Shock Train in a Constant Area Isolator. AIAA-91-2162, June 1991.

7. Hunter, L. G.; and Couch, B. D.: A CFD Study of Precombustion Shock-Trains From Mach 3–6. AIAA-90-2220, July 1990.

8. Carroll, B. F.; and Dutton, J. C.: Characteristics of Multiple Shock Wave/Turbulent Boundary-Layer Interactions in Rectangular Ducts. *J. Propuls. & Power*, vol. 6, no. 2, Mar.–Apr. 1990, pp. 186–193.

9. Carroll, B. F.; and Dutton, J. C.: Multiple Normal Shock Wave/Turbulent Boundary-Layer Interactions. *J. Propuls. & Power*, vol. 8, no. 2, Mar.–Apr. 1992, pp. 441–448.

10. Mahoney, John J.: *Inlets for Supersonic Missiles*, AIAA Education Series, 1990.

11. Korkegi, R. H.: Comparison of Shock-Induced Two- and Three-Dimensional Incipient Turbulent Separation. *AIAA J.*, vol. 13, no. 4, Apr. 1975, pp. 534–535.

12. Kuehn, Donald M.: *Experimental Investigation of the Pressure Rise Required for the Incipient Separation of Turbulent Boundary Layers in Two-Dimensional Supersonic Flow.* NASA MEMO 1-21-59A, 1959.

13. Reddy, D. R.; and Weir, L. J.: Three-Dimensional Viscous Analysis of a Mach 5 Inlet and Comparison With Experimental Data. *J. Propuls. & Power*, vol. 8, no. 2, Mar.–Apr. 1992, pp. 432–440.

14. Settles, Gary S.; and Dolling, David S.: Swept Shock Wave/ Boundary-Layer Interactions. *Tactical Missile Aerodynamics*, Michael J. Hemsch and Jack N. Nielson, eds., AIAA, 1986, pp. 297–379.

15. Settles, G. S.; and Dolling, D. S.: Swept Shock/Boundary-Layer Interactions—Tutorial and Update. AIAA-90-0375, Jan. 1990.

16. Kantrowitz, Arthur; and Donaldson, Coleman duP.: *Preliminary Investigation of Supersonic Diffusers*. NACA WR L-713, 1945. (Formerly NACA ACR L5D20.)

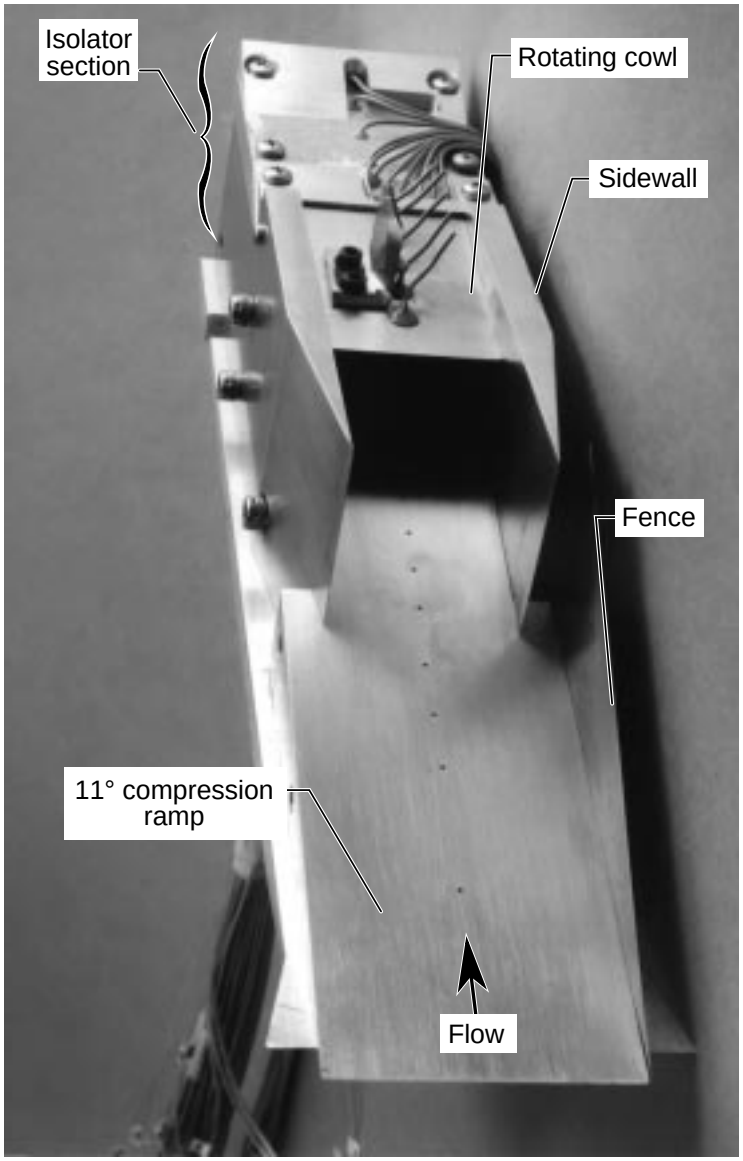

L-91-16292

(a) Model assembly.

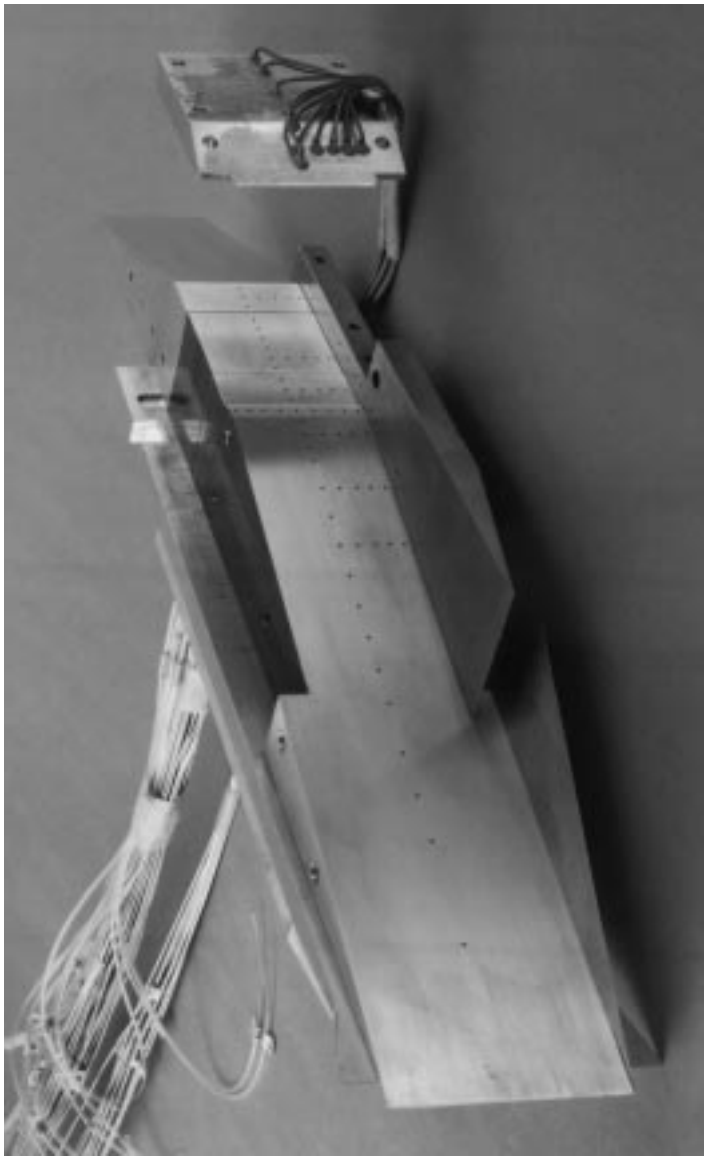

L-91-16290

(b) Model assembly without left side fence, left sidewall, and cowl.

Figure 1. Uninstalled inlet-isolator model.

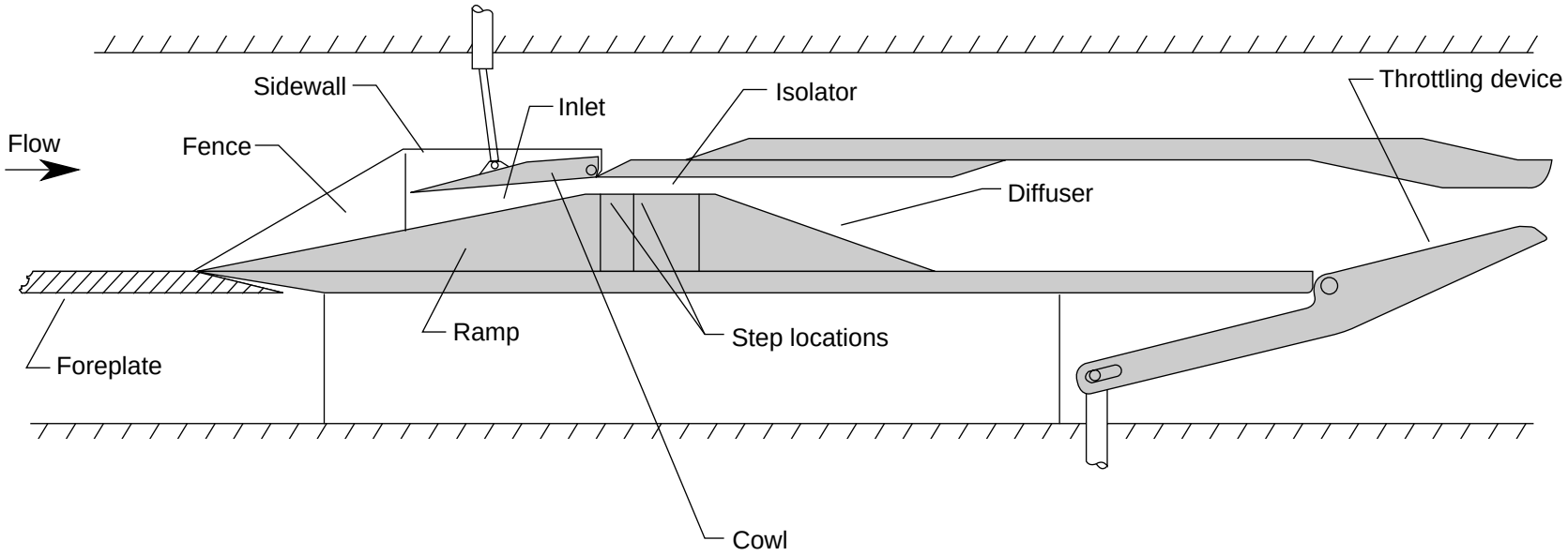

Figure 2. Schematic diagram of assembled model cross section.

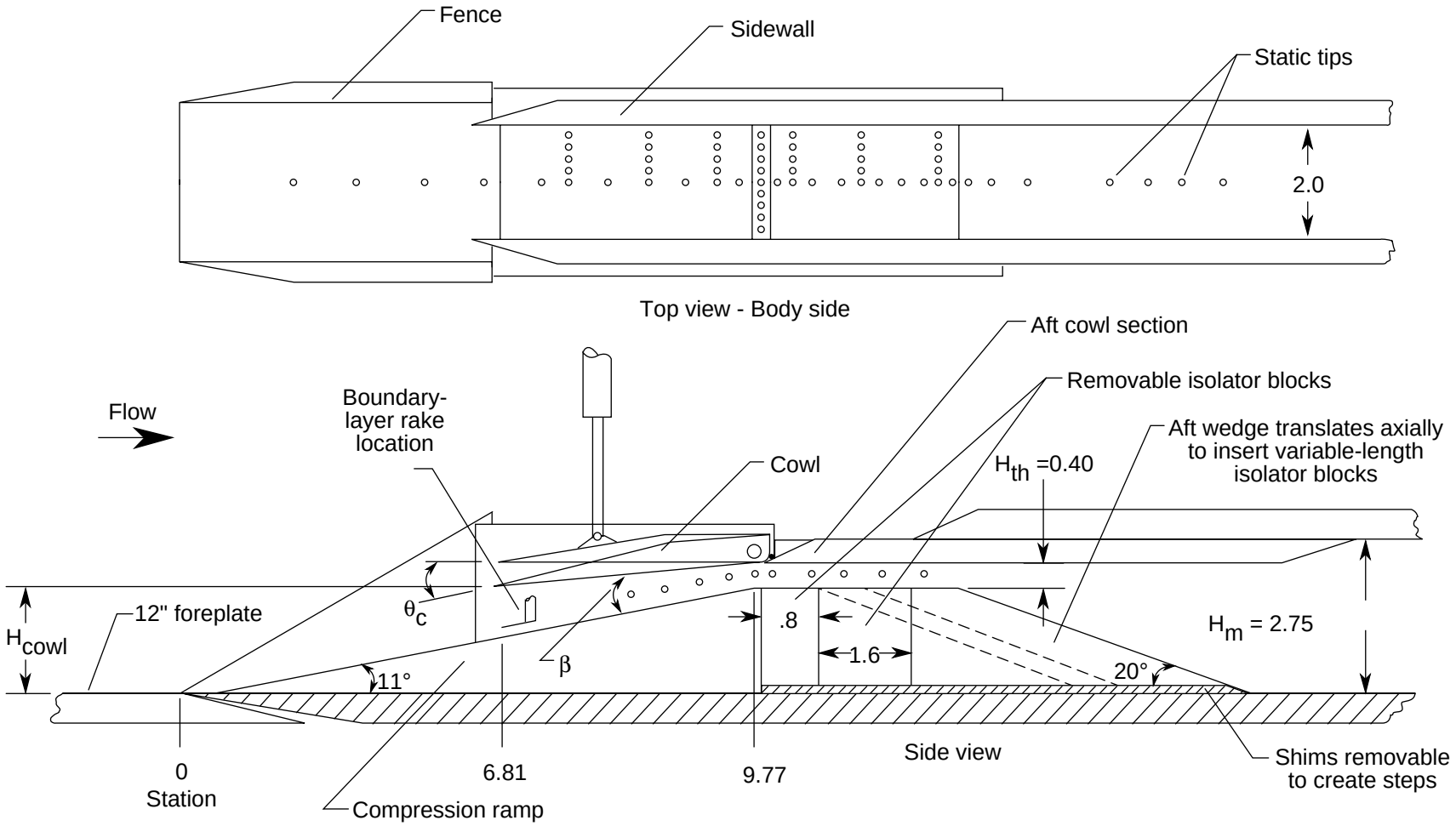

Figure 3. Schematic diagram of model. Linear dimensions are given in inches.

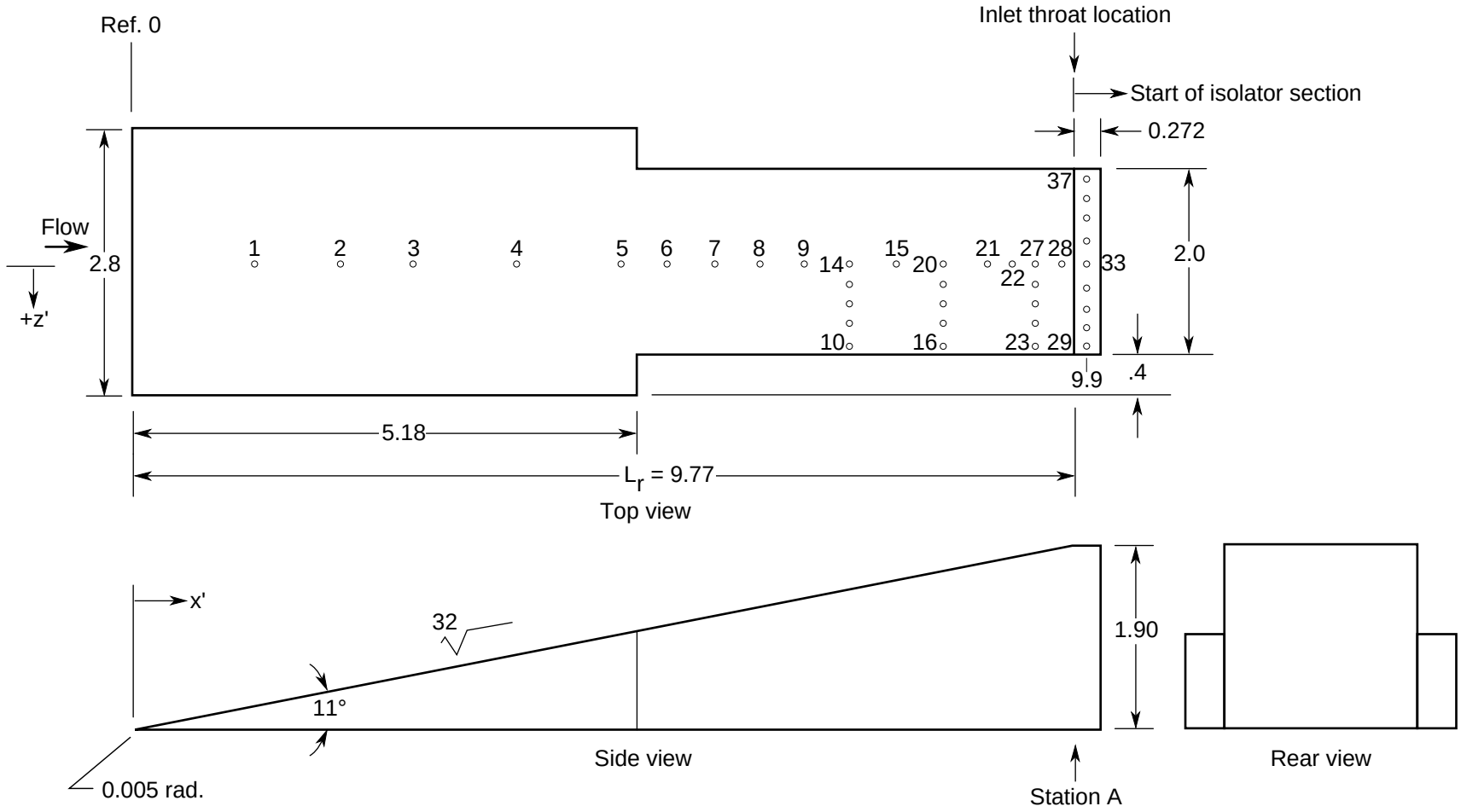

(a) Compression ramp (aluminum).

Figure 4. Instrumentation layouts. See figure 4(h) for orifice locations. Linear dimensions are given in inches.

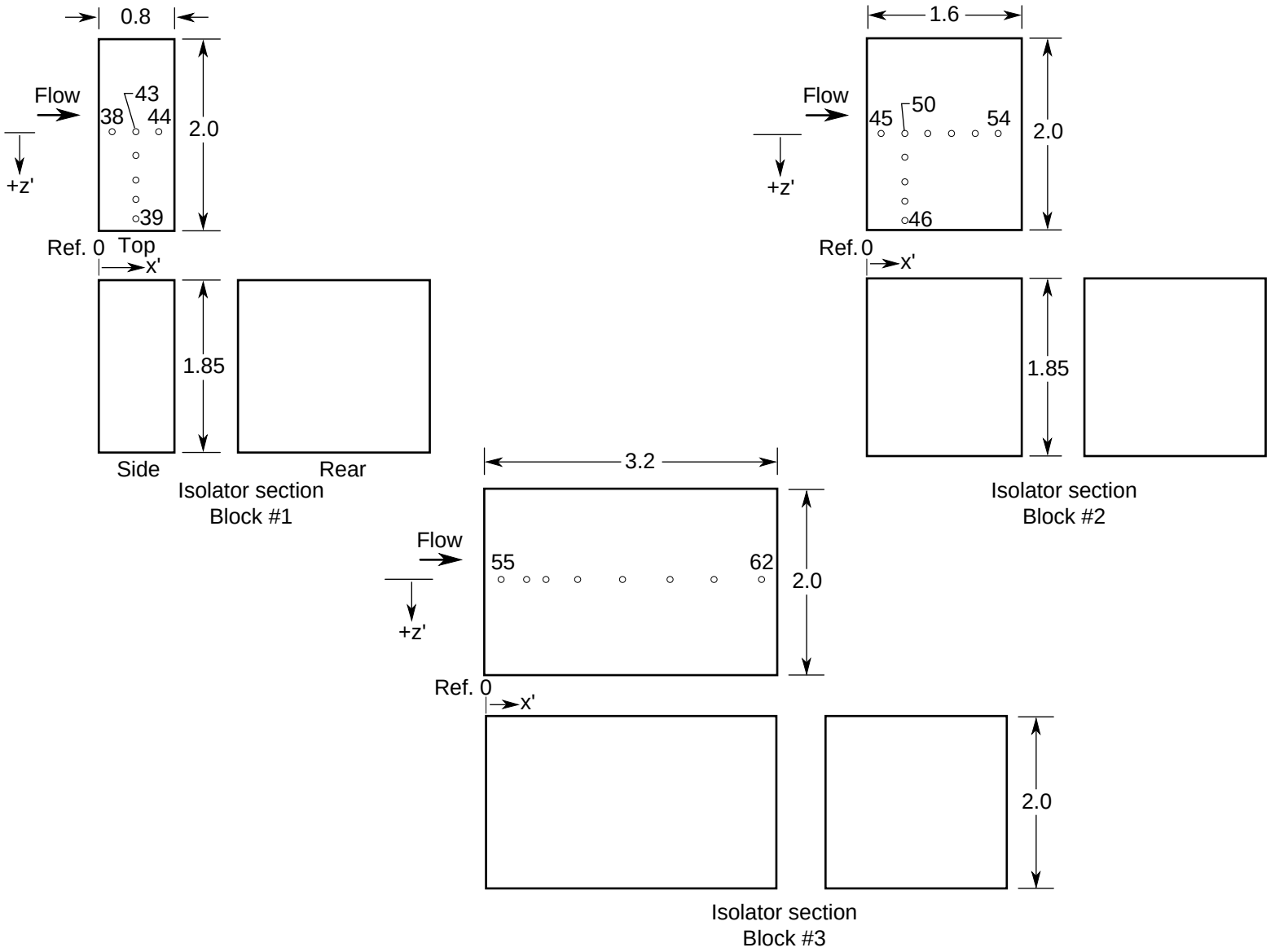

(b) Isolator blocks (aluminum).

Figure 4. Continued.

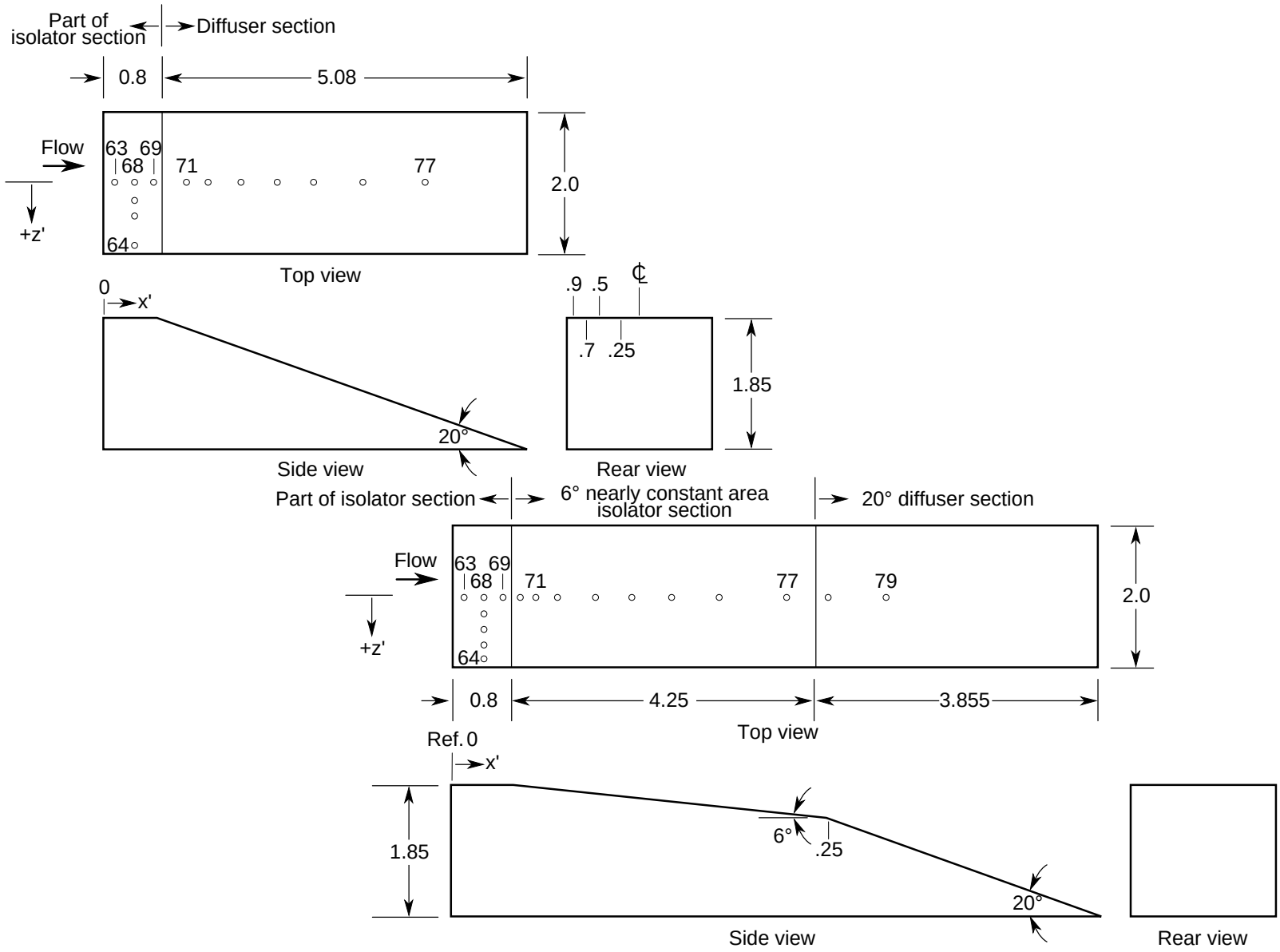

(c) Aft wedges (aluminum).

Figure 4. Continued.

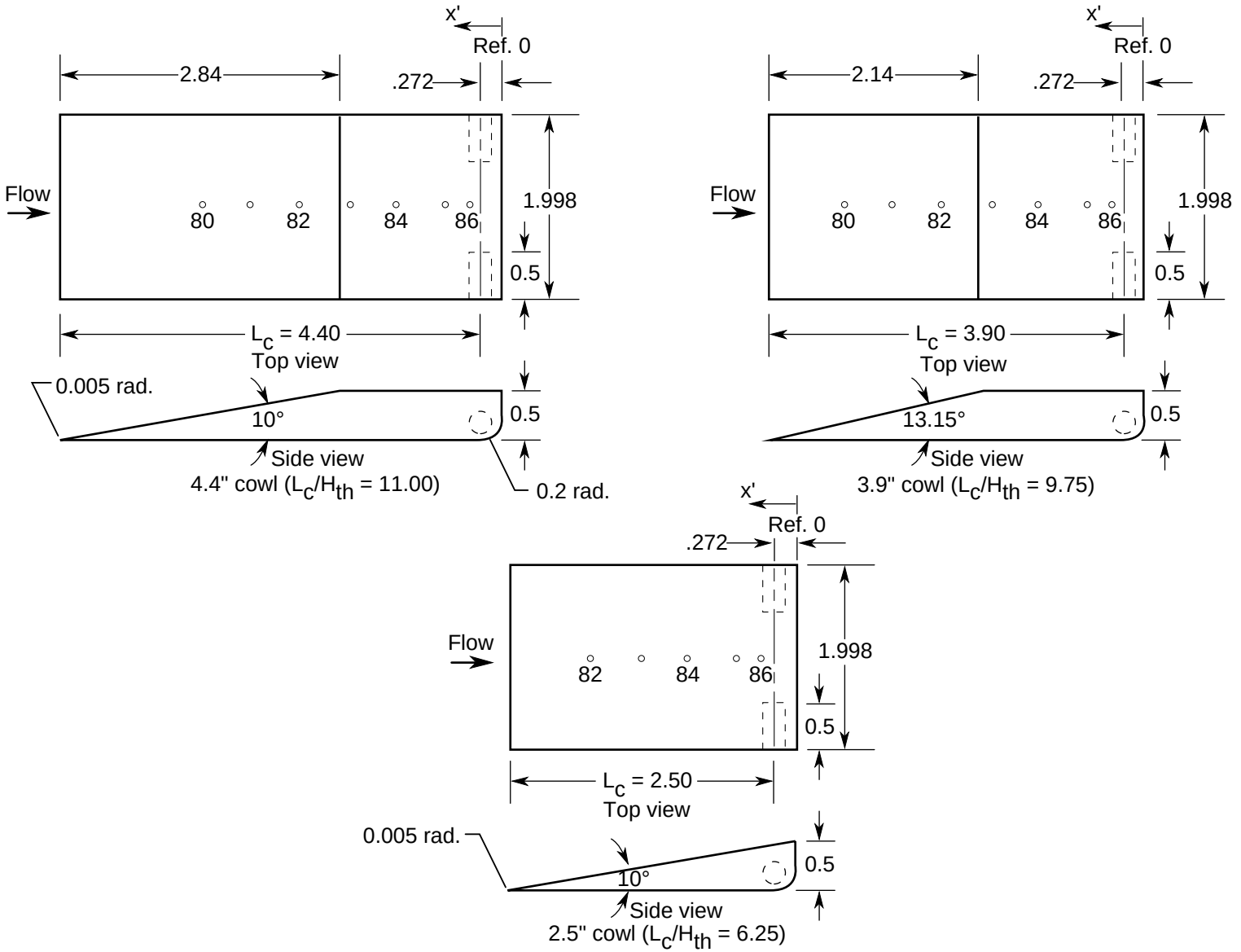

(d) Forward cowl sections (stainless steel).

Figure 4. Continued.

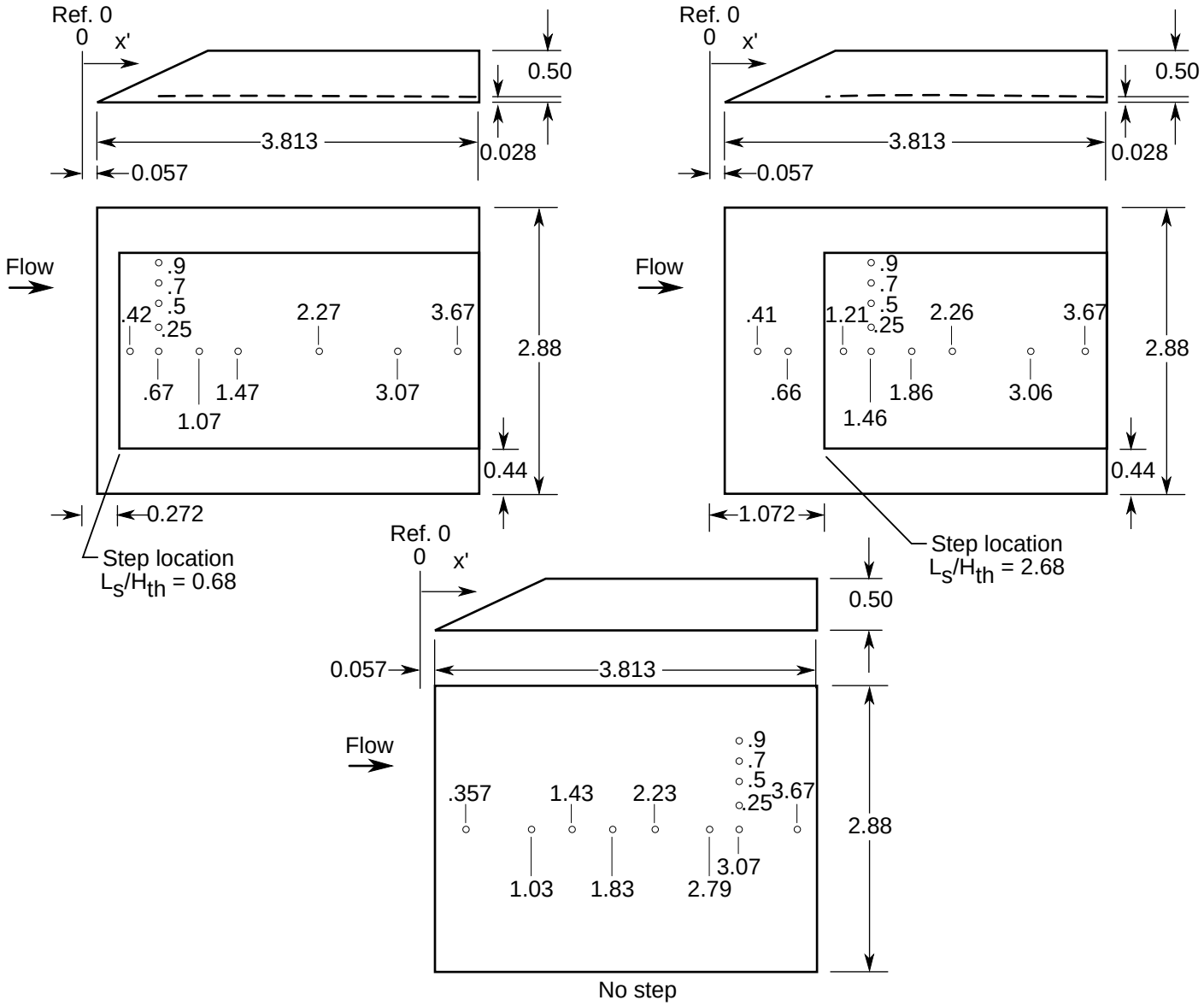

(e) Isolator aft cowl sections (aluminum).

Figure 4. Continued.

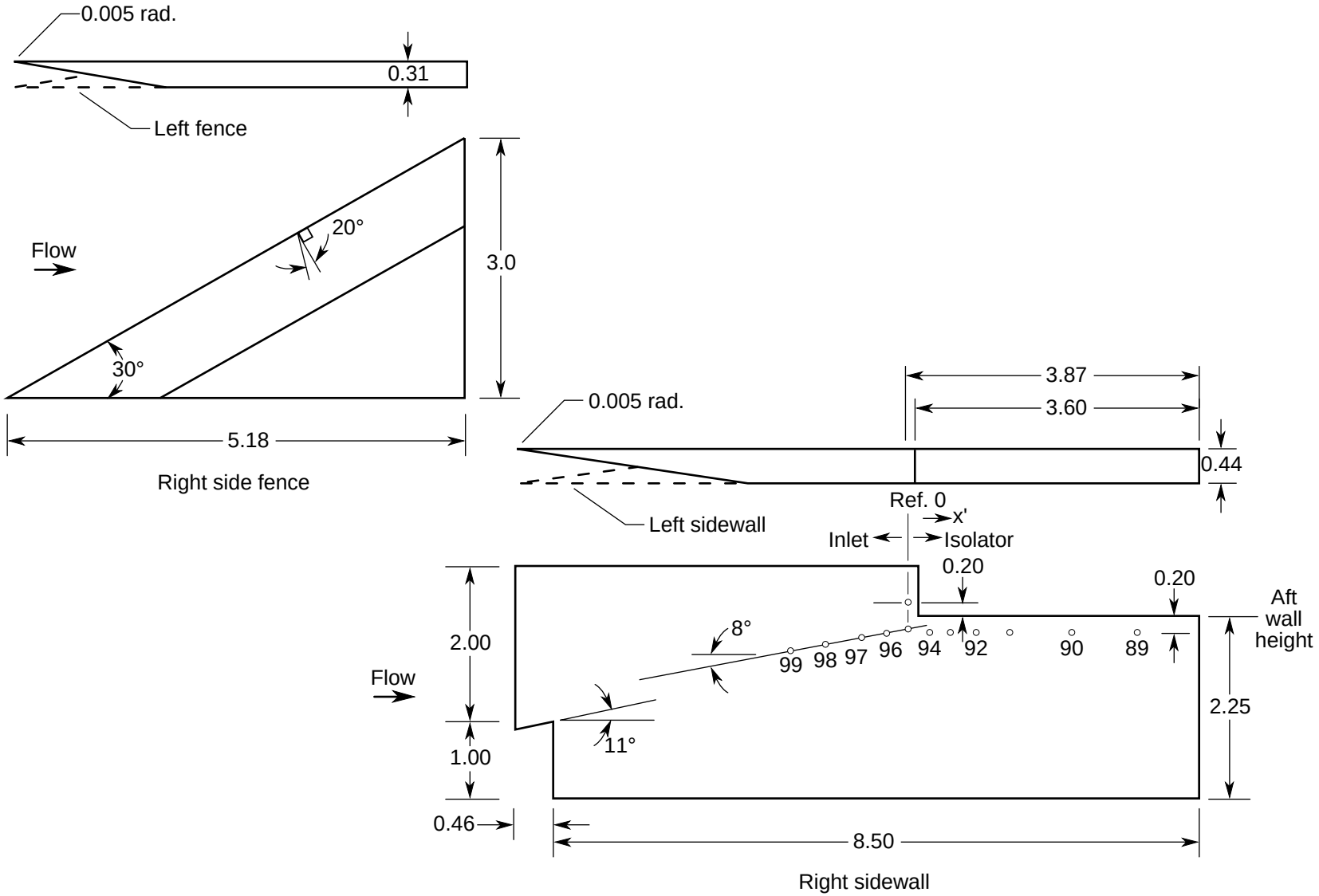

(f) Fence and sidewall (stainless steel).

Figure 4. Continued.

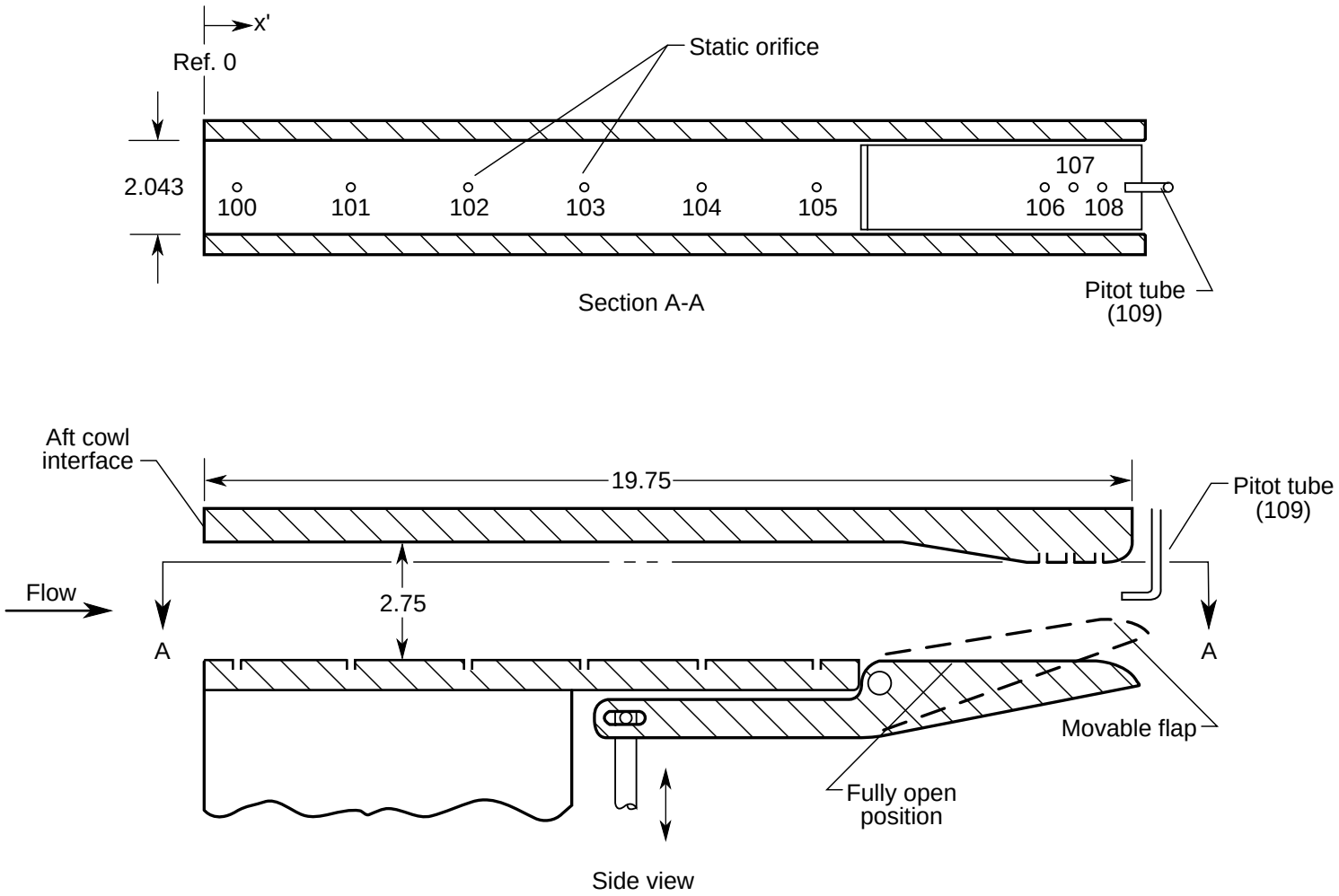

(g) Schematic diagram of back-pressure throttling device (aluminum).

Figure 4. Continued.

Compression ramp
(see fig. 4(a))

Orifice	x'	z'
1	1.79	0.00
2	3.09	0.00
3	3.68	0.00
4	4.27	0.00
5	5.02	0.00
6	5.51	0.00
7	6.00	0.00
8	6.49	0.00
9	6.98	0.00
10	7.47	0.90
11	7.47	0.70
12	7.47	0.50
13	7.47	0.25
14	7.47	0.00
15	7.96	0.00
16	8.45	0.90
17	8.45	0.70
18	8.45	0.50
19	8.45	0.25
20	8.45	0.00
21	8.94	0.00
22	9.19	0.00
23	9.43	0.90
24	9.43	0.70
25	9.43	0.50
26	9.43	0.25
27	9.43	0.00
28	9.68	0.00
29	9.91	0.90
30	9.91	0.70
31	9.91	0.50
32	9.91	0.25
33	9.91	0.00
34	9.91	–0.25

Compression ramp (cont.)

Orifice	x'	z'
35	9.91	–0.50
36	9.91	–0.70
37	9.91	–0.90

Isolator blocks
(see fig. 4(b))

Orifice	x'	z'
38	0.15	0.00
39	0.40	0.90
40	0.40	0.70
41	0.40	0.50
42	0.40	0.25
43	0.40	0.00
44	0.65	0.00
45	0.15	0.00
46	0.40	0.90
47	0.40	0.70
48	0.40	0.50
49	0.40	0.25
50	0.40	0.00
51	0.65	0.00
52	0.90	0.00
53	1.15	0.00
54	1.40	0.00
55	0.15	0.00
56	0.40	0.00
57	0.65	0.00
58	1.00	0.00
59	1.50	0.00
60	2.00	0.00
61	2.50	0.00
62	3.00	0.00

Diffuser section
(see fig. 4(c))

Orifice	x'	z'
63	0.25	0.00
64	0.40	0.90
65	0.40	0.70
66	0.40	0.50
67	0.40	0.25
68	0.40	0.00
69	0.65	0.00
70	0.90	0.00
71	1.15	0.00
72	1.50	0.00
73	2.00	0.00
74	2.50	0.00
75	3.00	0.00
76	3.80	0.00
77	4.80	0.00
78	5.30	0.00
79	6.05	0.00

Forward cowl sections
(see fig. 4(d))

Orifice	x'	z'
80	3.10	0.00
81	2.60	0.00
82	2.10	0.00
83	1.60	0.00
84	1.10	0.00
85	0.60	0.00
86	0.35	0.00

Cowl aft sections
(refer to fig. 4(e))

Sidewall
(see fig. 4(f))

Orifice	x'	z'
89	2.80	2.00
90	2.00	2.00
91	1.20	2.00
92	0.80	2.00
93	0.40	2.00
94	0.15	2.00
95	–0.20	2.00
96	–0.37	2.00
97	–0.62	2.00
98	–1.11	2.00
99	–1.60	2.00

Back pressure mechanism
(see fig. 4(g))

Orifice	x'	z'
100	0.60	0.00
101	3.10	0.00
102	5.60	0.00
103	8.10	0.00
104	10.60	0.00
105	13.10	0.00
106	18.60	0.00
107	18.90	0.00
108	19.10	0.00
109	19.00	0.00

(h) Instrumentation layout locations for figures 4(a)–4(d) and 4(f).

Figure 4. Concluded.

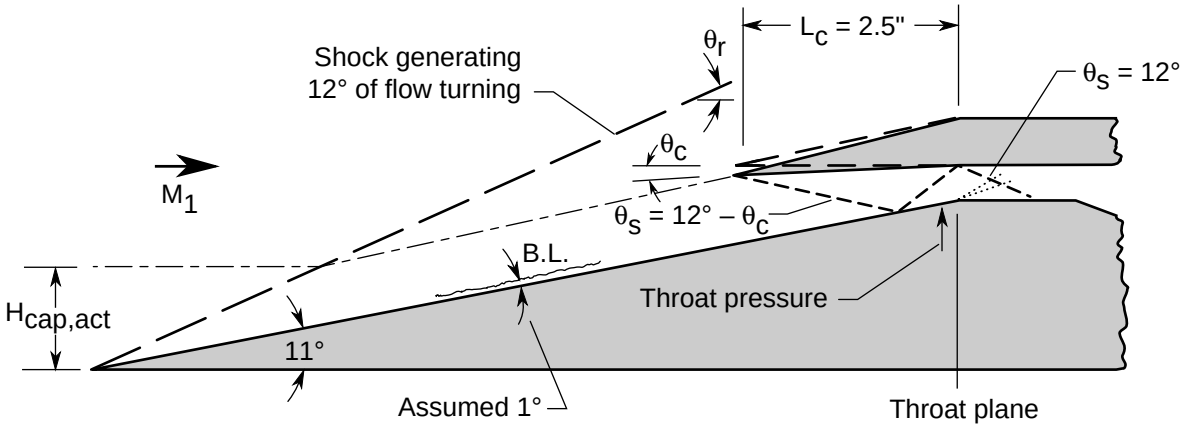

(a) Short 2.5-in. cowl (L_c/H_{th} = 6.25).

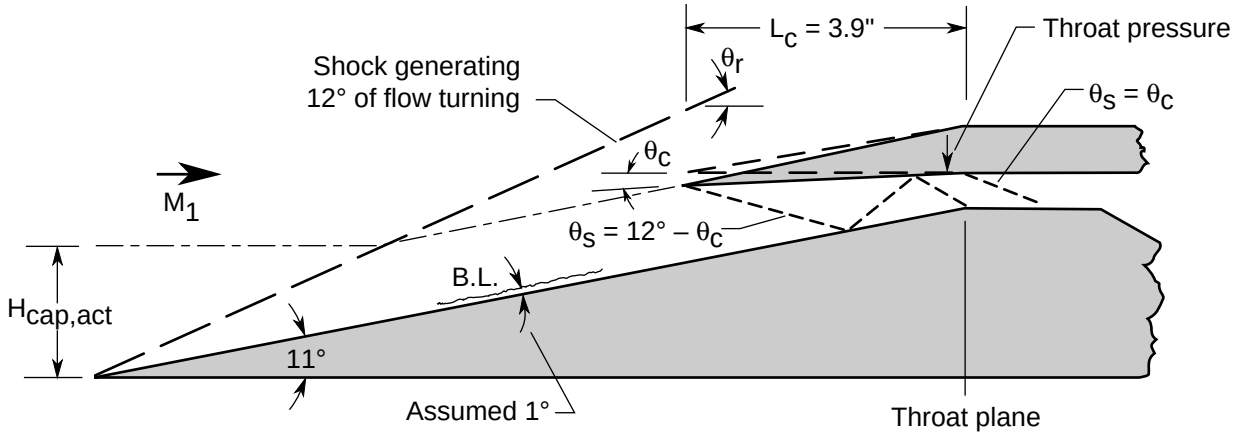

(b) Medium 3.9-in. cowl (L_c/H_{th} = 9.75).

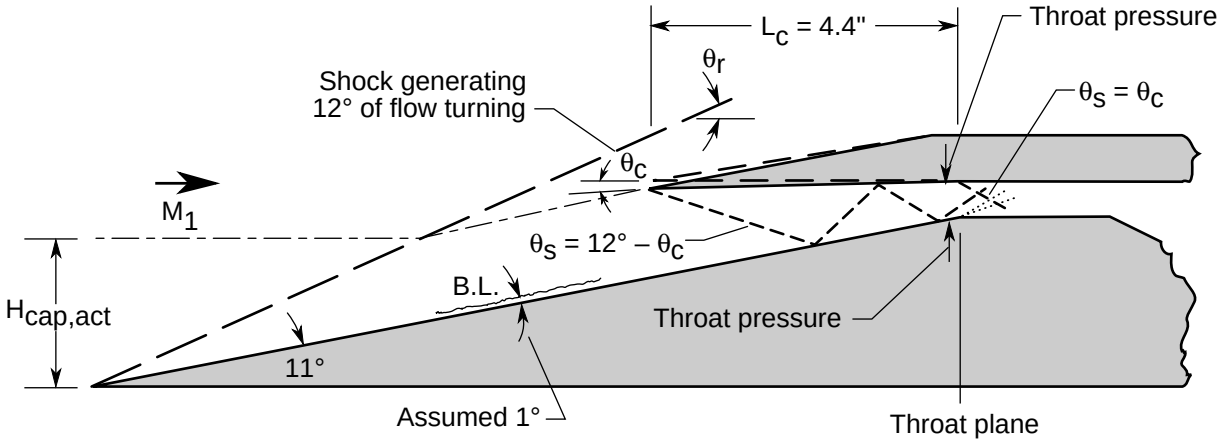

(c) Long 4.4-in. cowl (L_c/H_{th} = 11.00).

Figure 5. Cowl configurations.

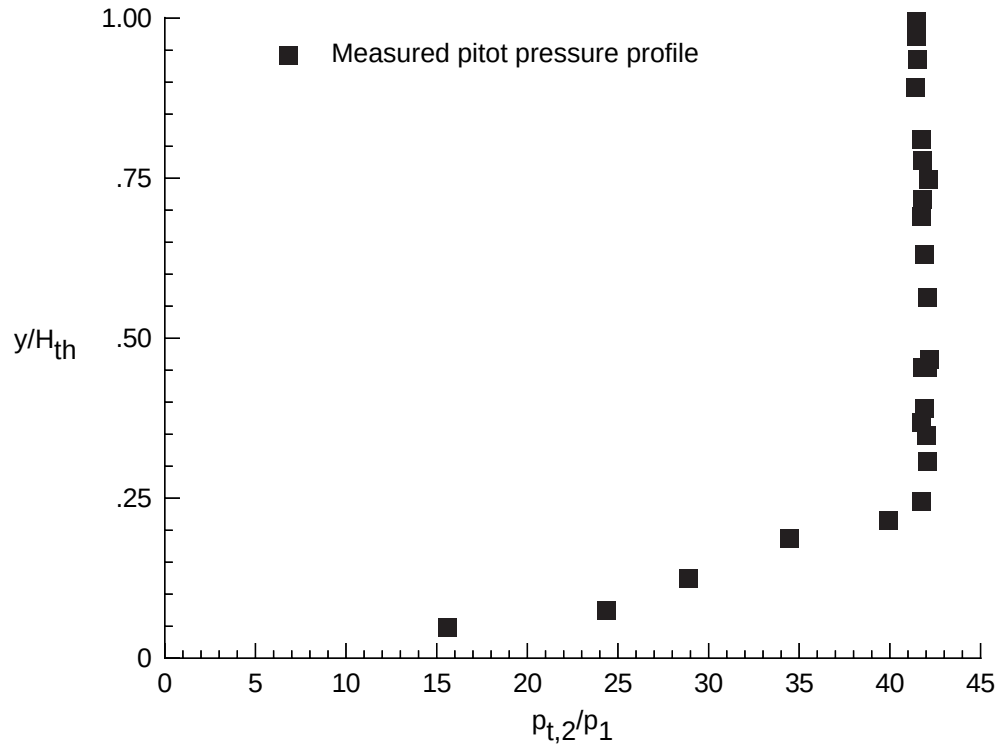

(a) Pitot pressure profile for thin boundary layer.

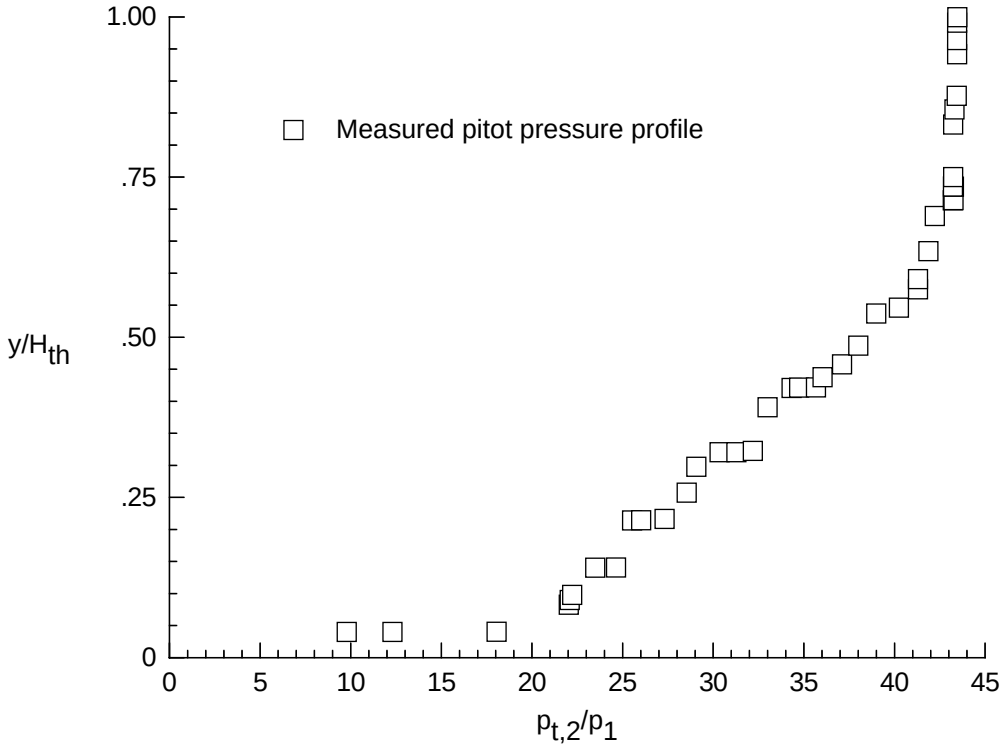

(b) Pitot pressure profile for thick boundary layer.

Figure 6. Measured pitot pressure profiles and calculated flow profiles with and without foreplate behind compression shock. Thick boundary layer (B.L.) refers to configuration with foreplate.

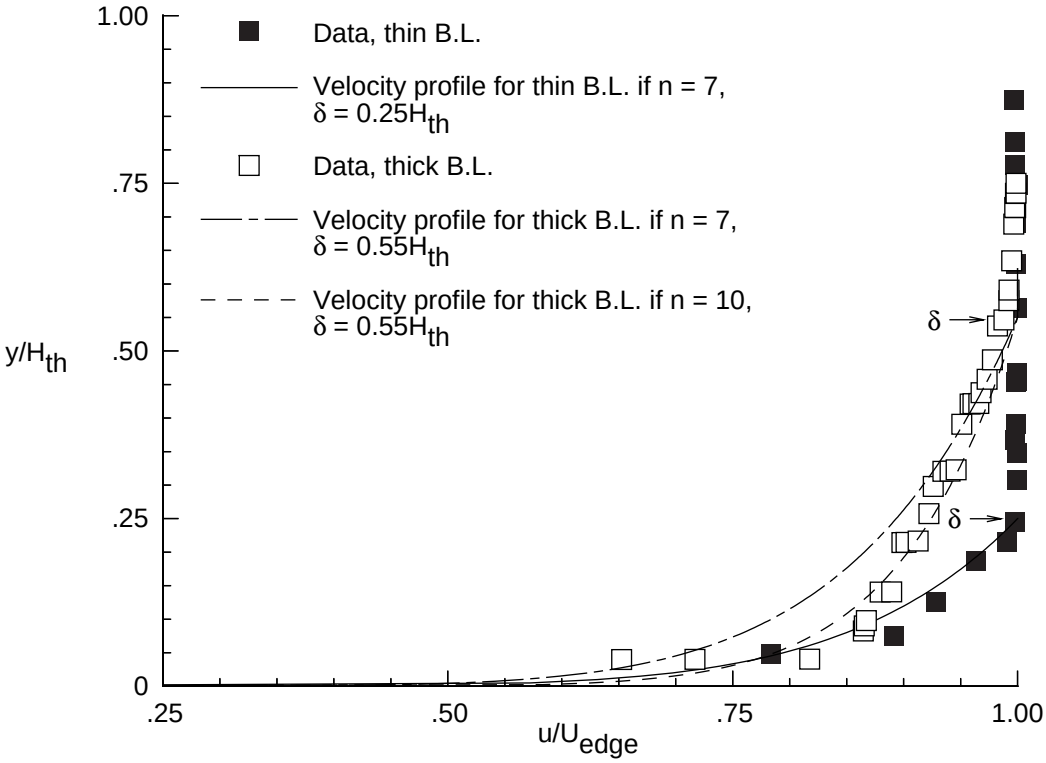

(c) Velocity profiles. $u/U_{edge} = (y/\delta)^{1/n}$.

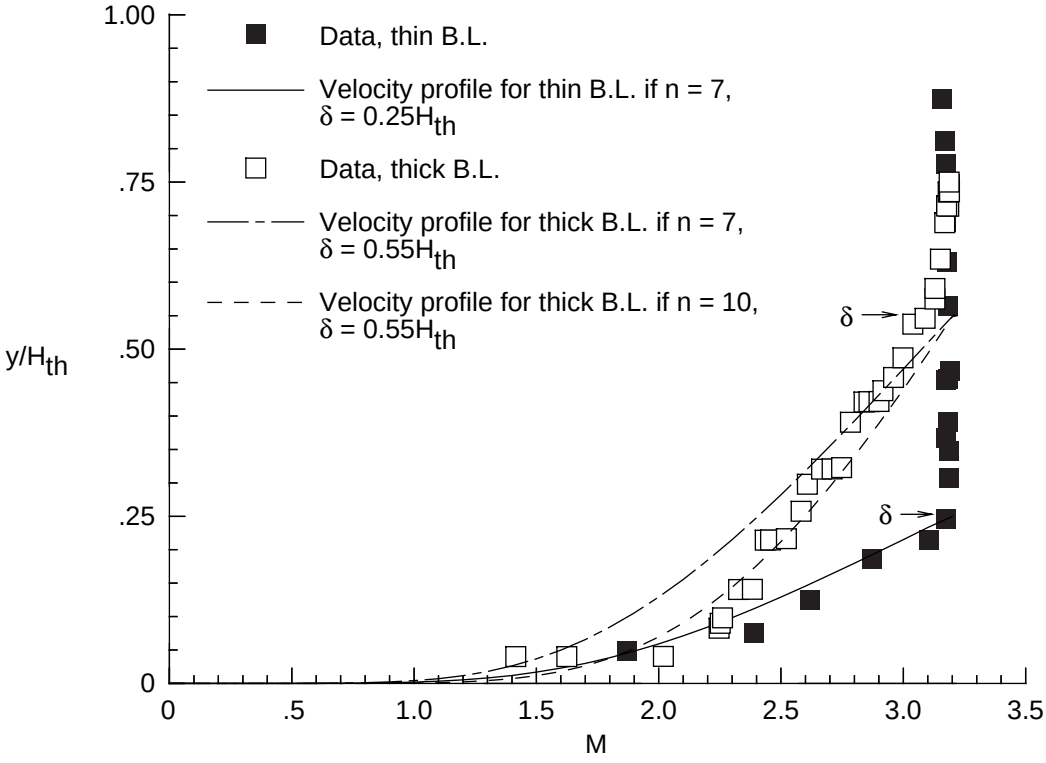

(d) Mach number profiles. $M \propto u/U_{edge} = (y/\delta)^{1/n}$.

Figure 6. Concluded.

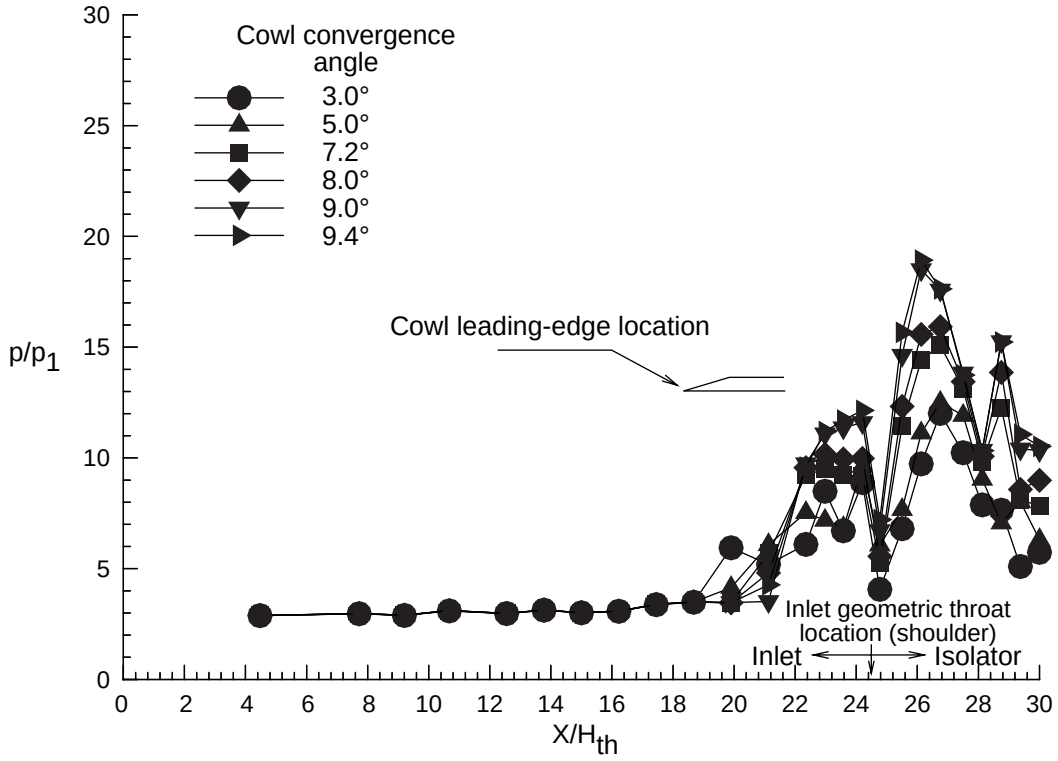

(a) Ramp pressure with thin boundary layer.

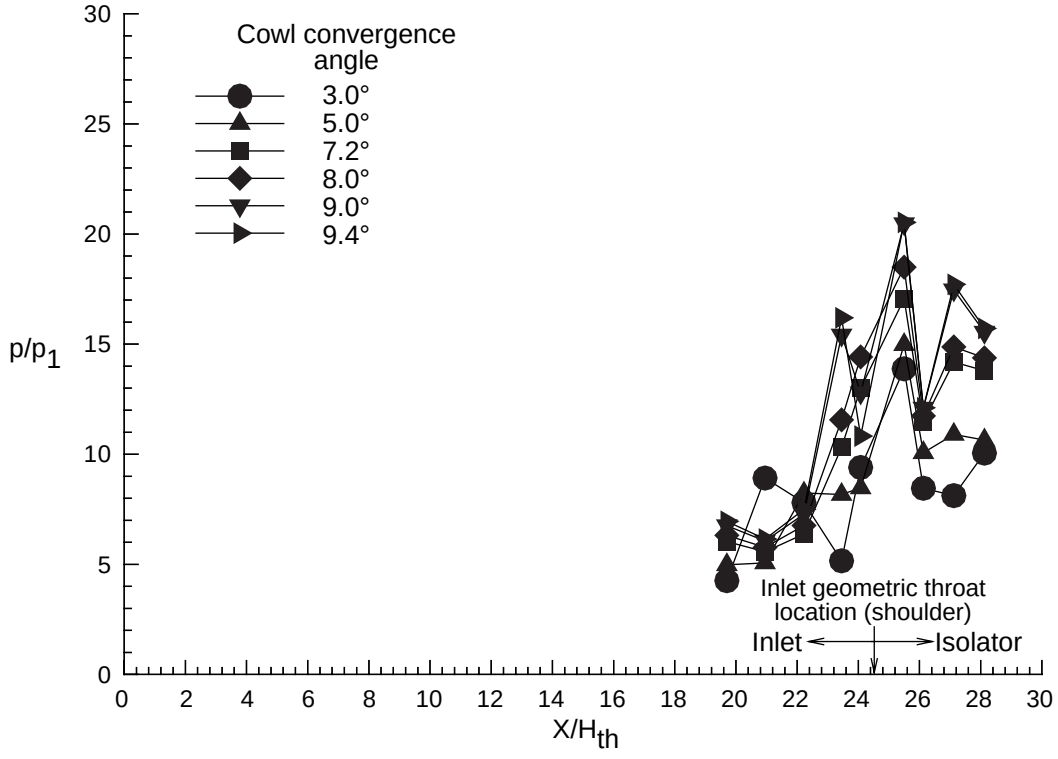

(b) Cowl pressure with thin boundary layer.

Figure 7. Inlet pressure distribution at different cowl convergence angles for 2.5-in. cowl (L_c/H_{th} = 6.25).

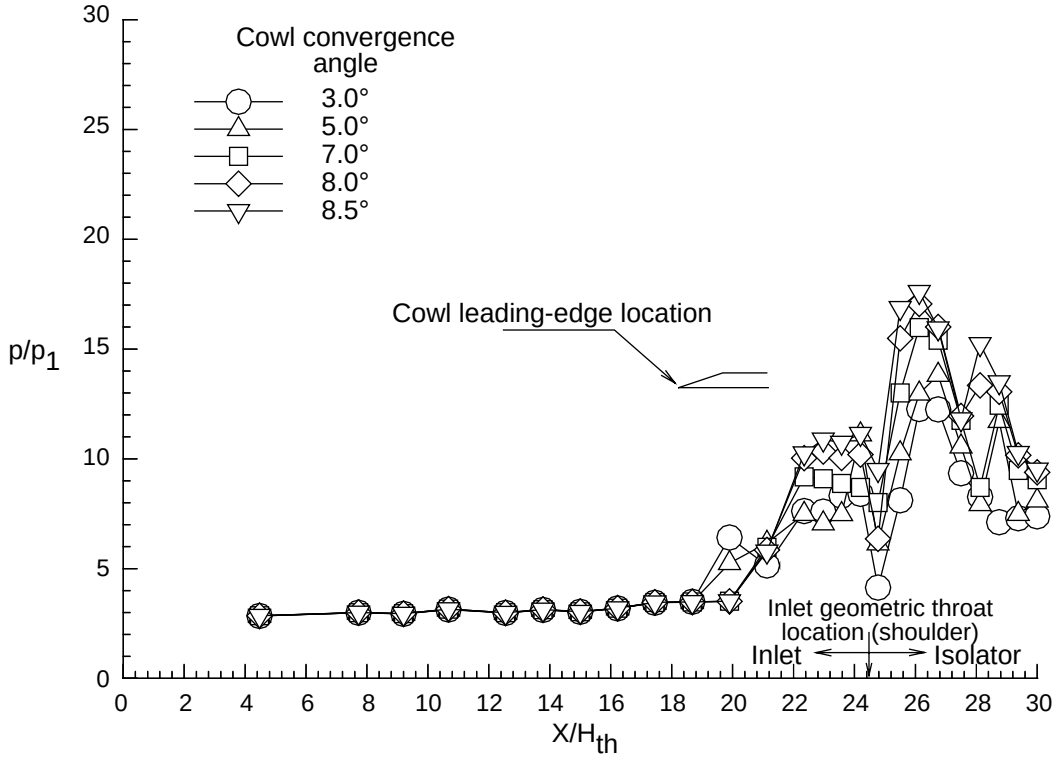

(c) Ramp pressure with thick boundary layer.

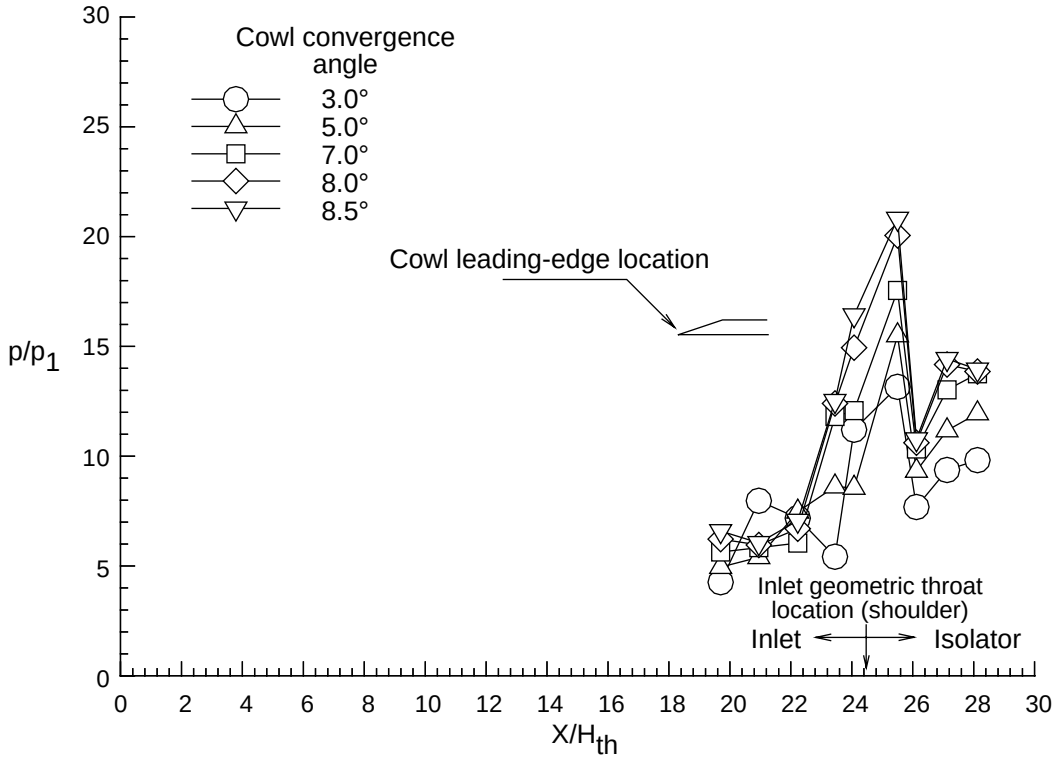

(d) Cowl pressure with thick boundary layer.

Figure 7. Concluded.

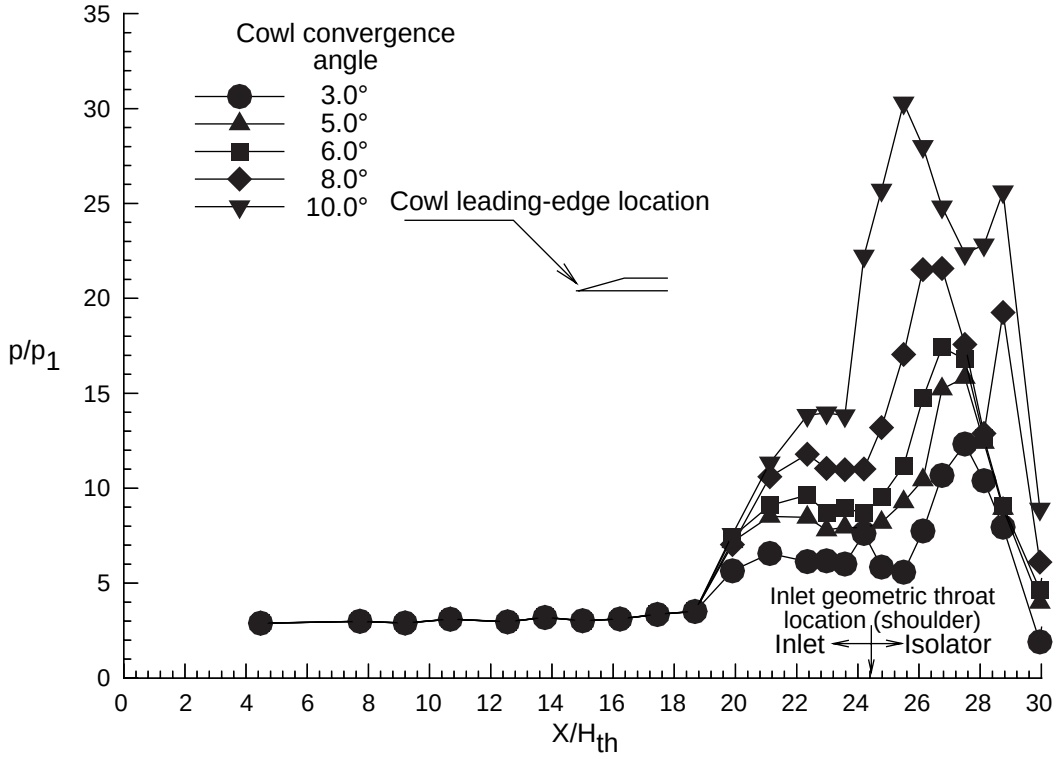

(a) Ramp pressure with thin boundary layer.

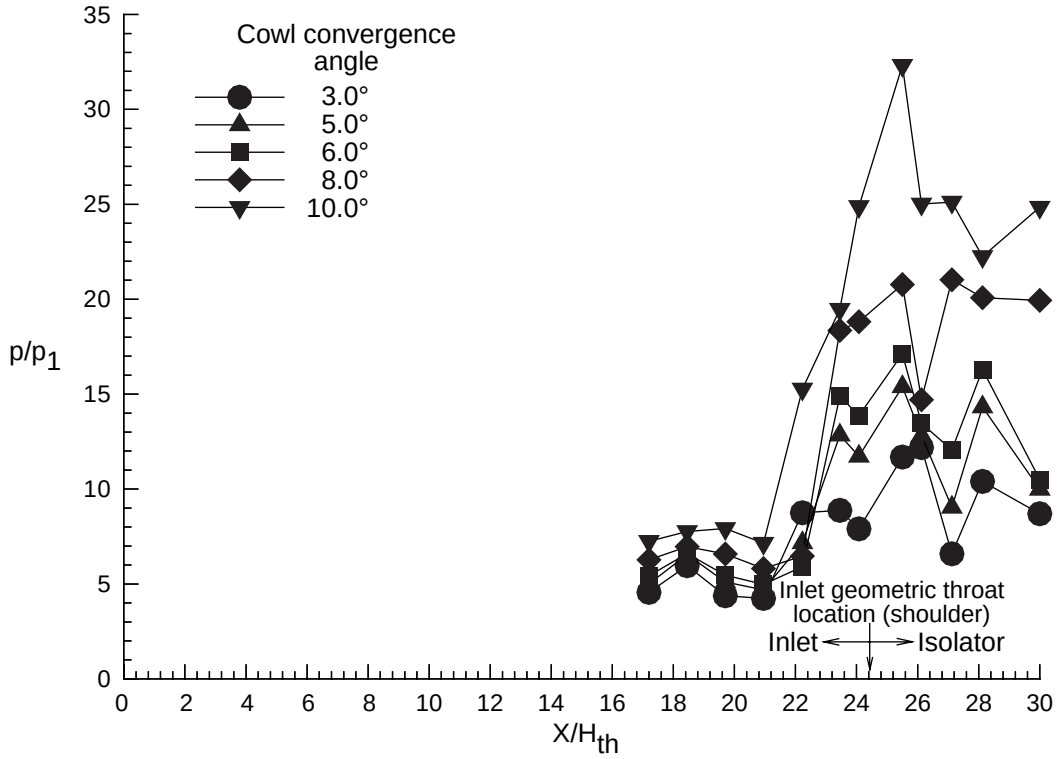

(b) Cowl pressure with thin boundary layer.

Figure 8. Inlet pressure distribution at different cowl convergence angles for 3.9-in. cowl (L_c/H_{th} = 9.75).

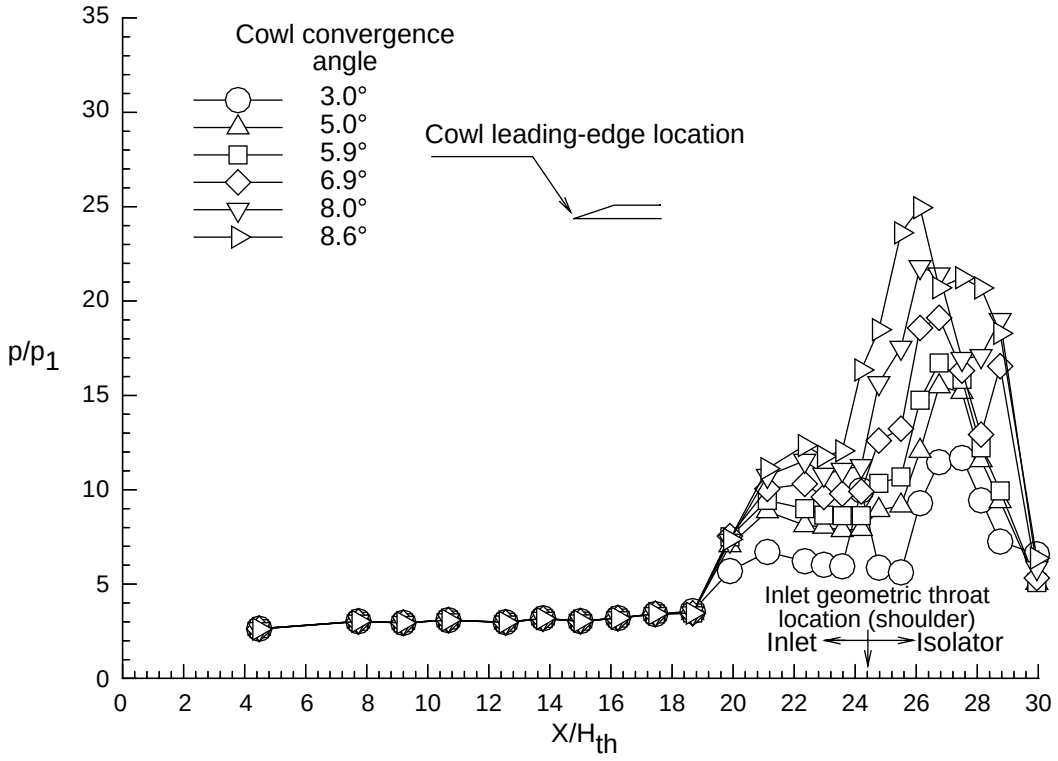

(c) Ramp pressure with thick boundary layer.

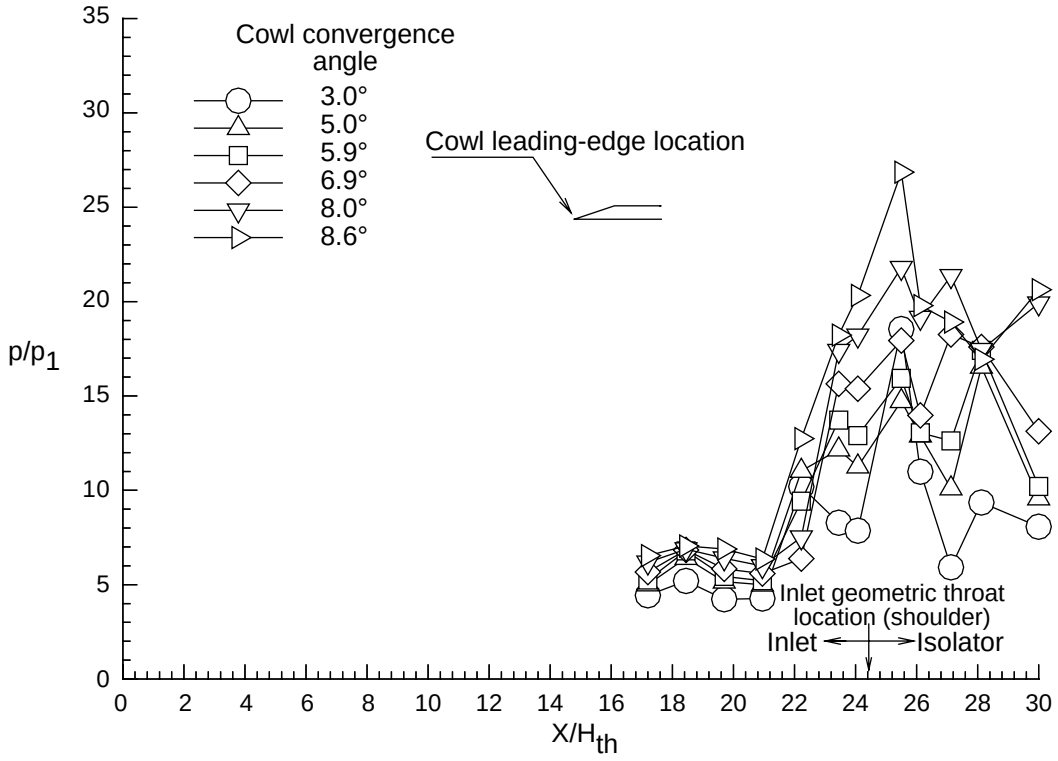

(d) Cowl pressure with thick boundary layer.

Figure 8. Concluded.

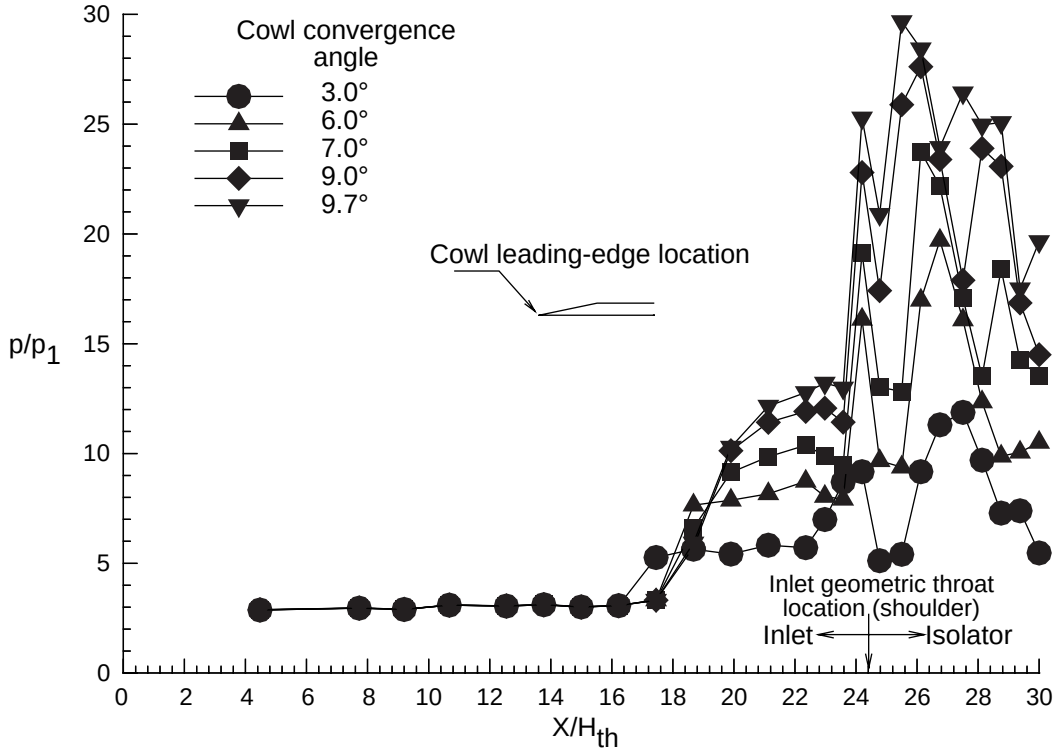

(a) Ramp pressure with thin boundary layer.

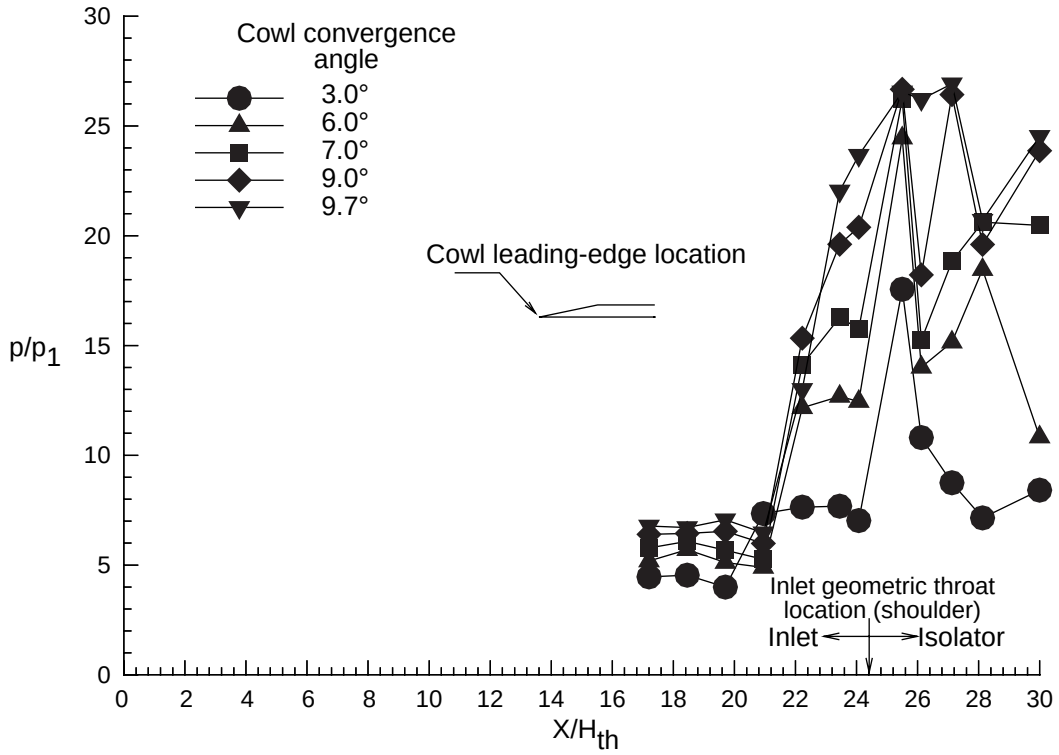

(b) Cowl pressure with thin boundary layer.

Figure 9. Inlet pressure distribution at different cowl convergence angles for 4.4-in. cowl (L_c/H_{th} = 11.00).

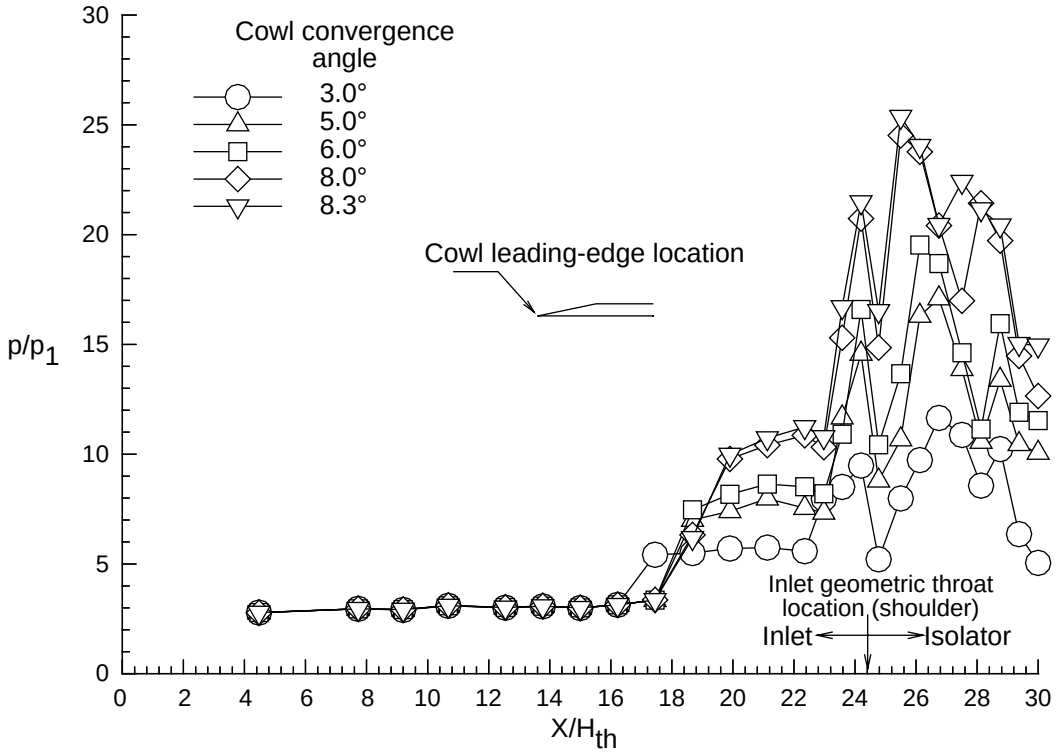

(c) Ramp pressure with thick boundary layer.

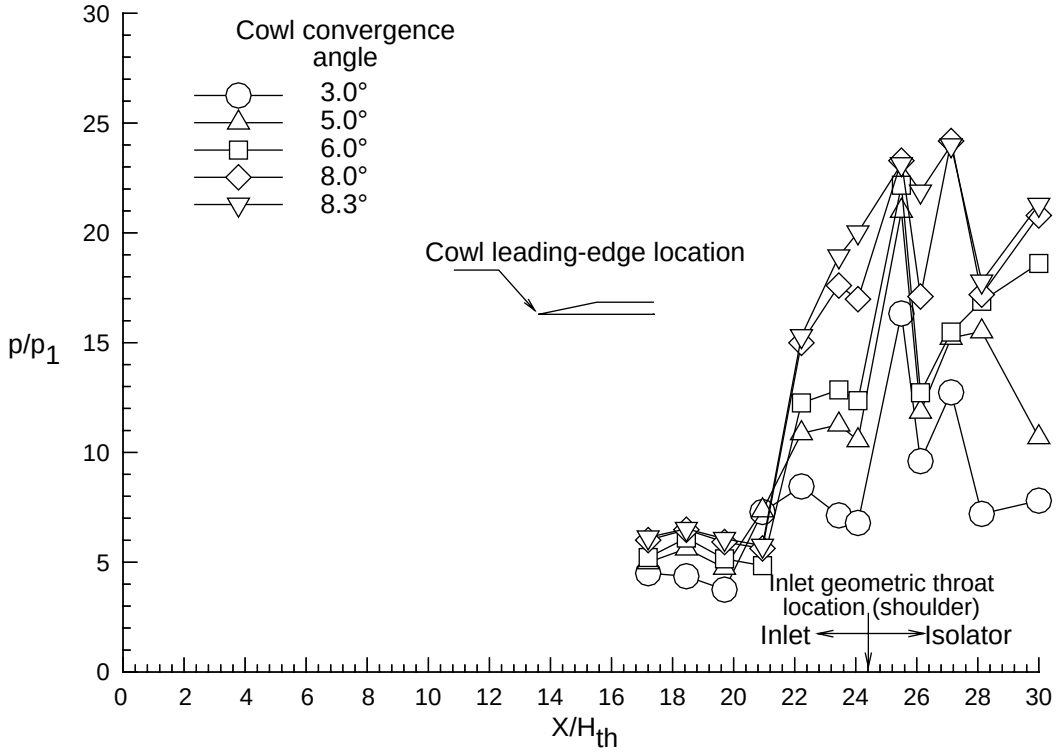

(d) Cowl pressure with thick boundary layer.

Figure 9. Concluded.

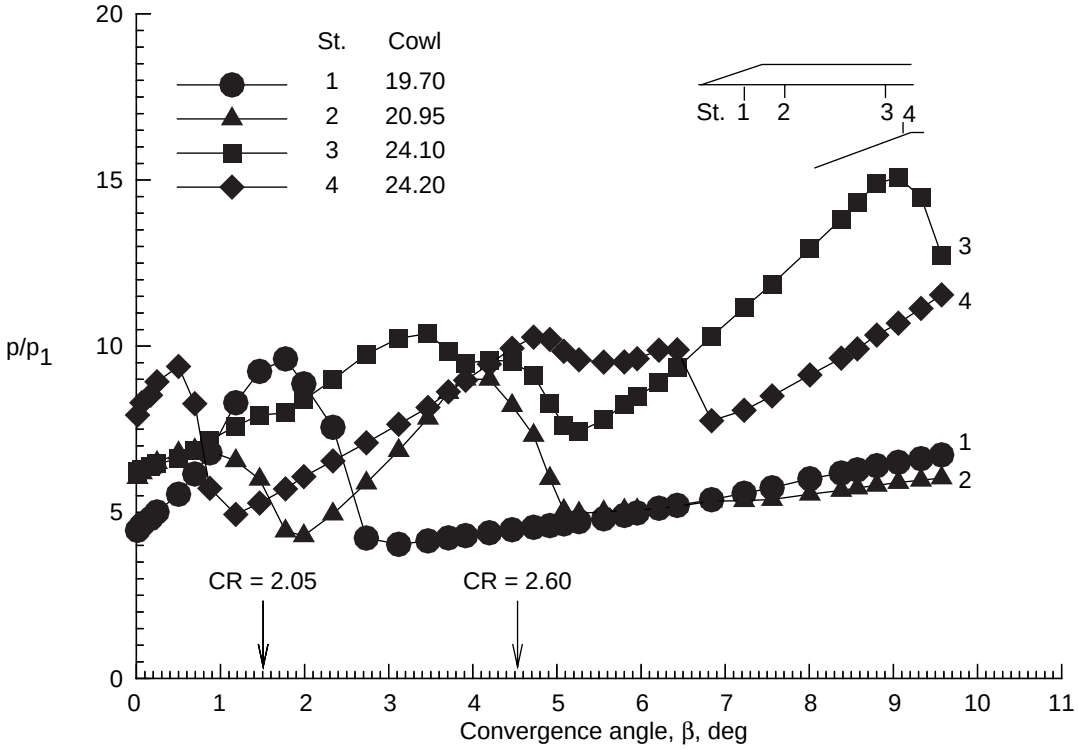

(a) Thin boundary layer.

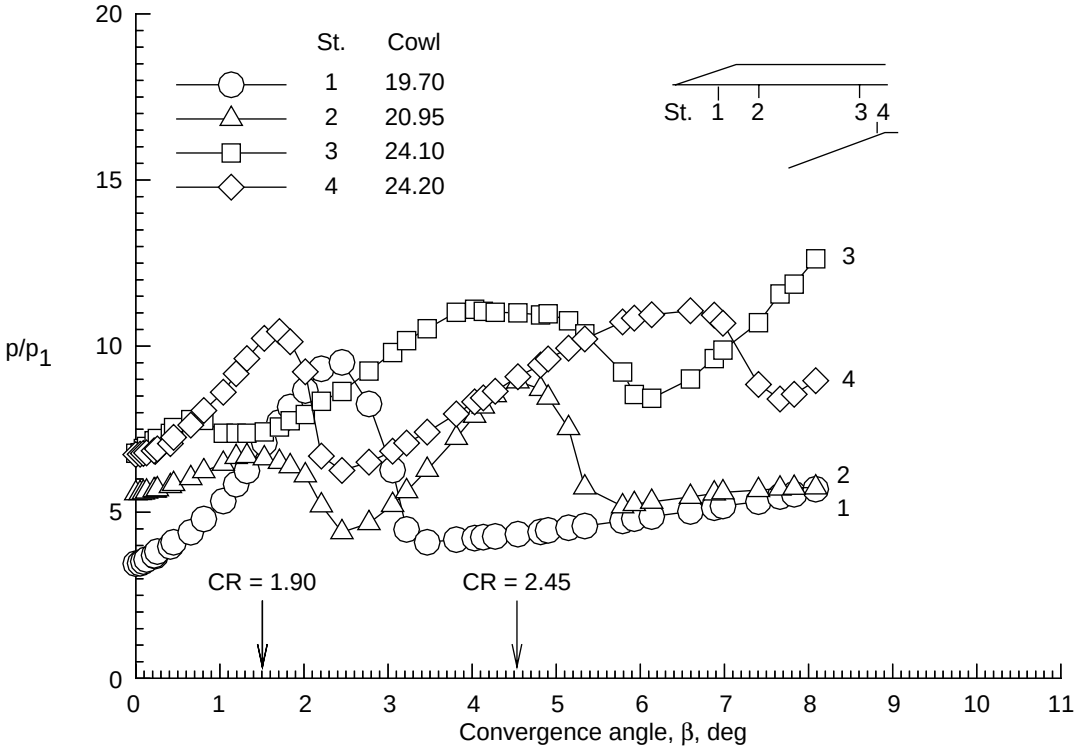

(b) Thick boundary layer.

Figure 10. Inlet local pressure variation versus cowl convergence angles for 2.5-in. cowl (L_c/H_{th} = 6.25). Static pressure taps referenced from ramp leading edge (X/H_{th}).

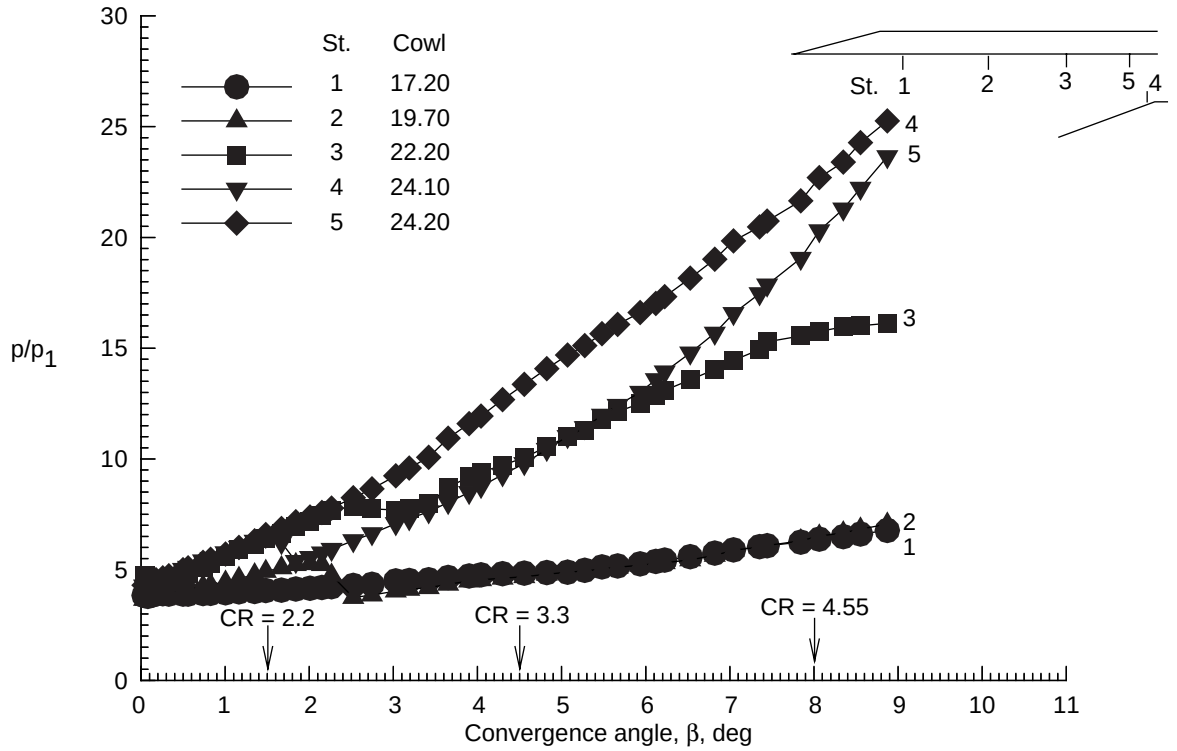

(a) Thin boundary layer.

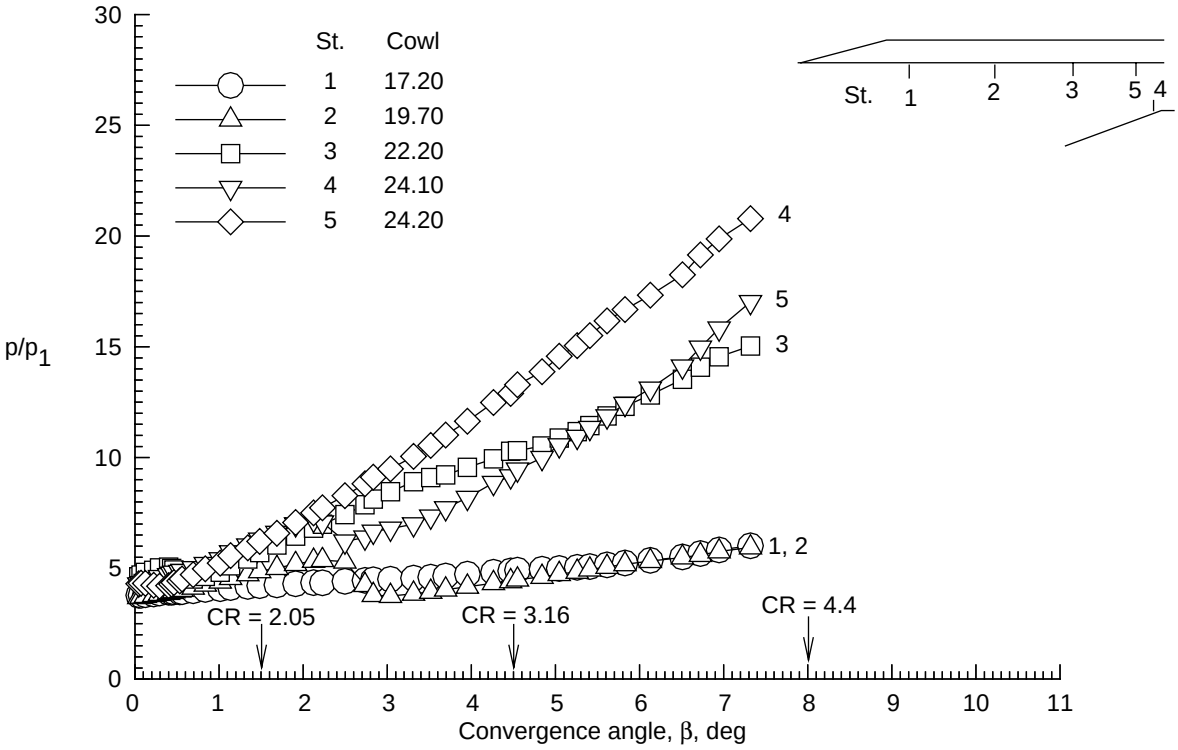

(b) Thick boundary layer.

Figure 11. Inlet local pressure variation versus convergence angles for 4.4-in. cowl (L_c/H_{th} = 11.00). Static pressure taps referenced from ramp leading edge (X/H_{th}).

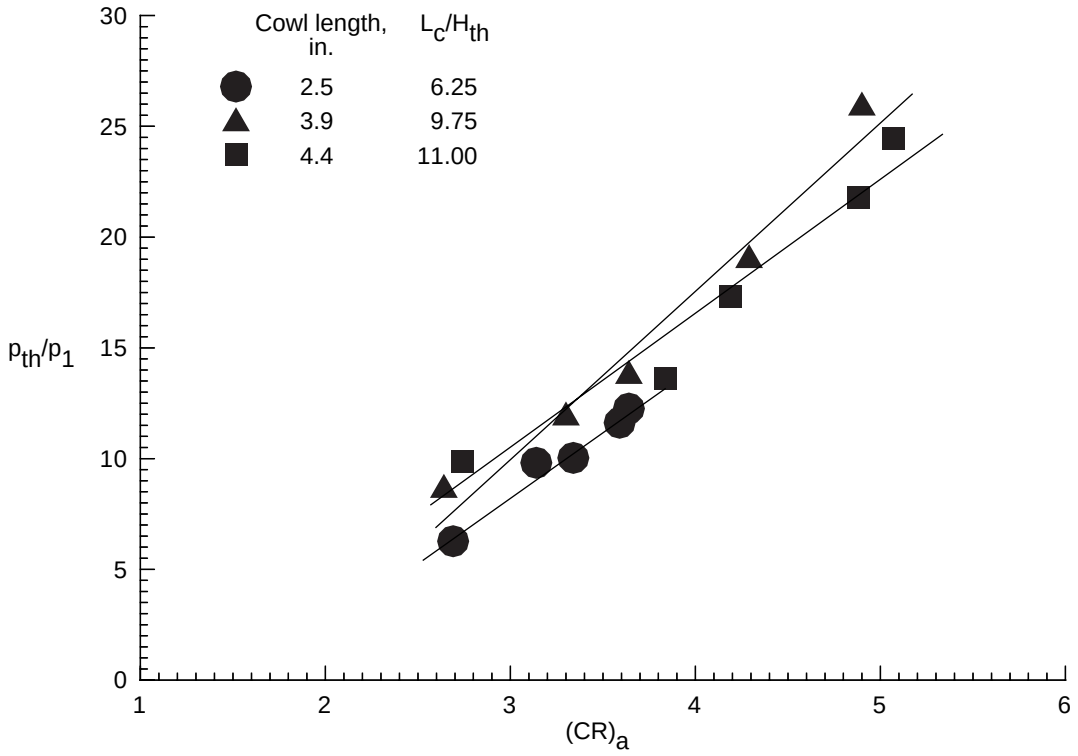

(a) Thin boundary layer.

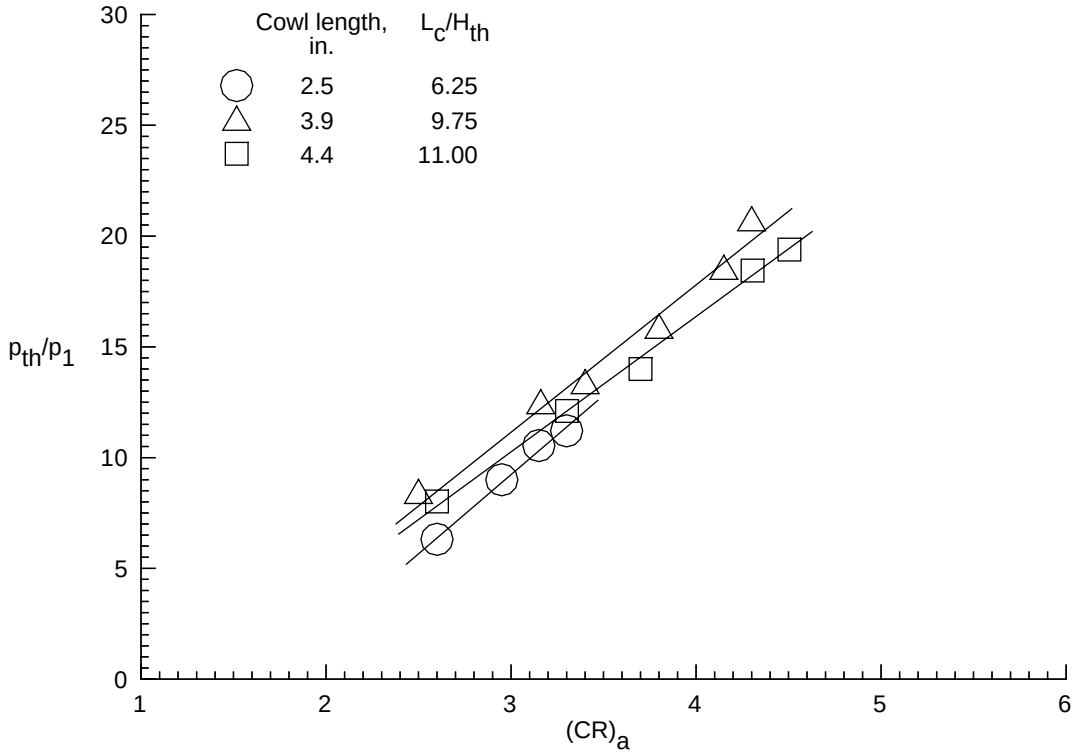

(b) Thick boundary layer.

Figure 12. Inlet throat static pressure versus inlet contraction ratio for 2.5-, 3.9-, and 4.4-in. cowls. Linear curve fit through data.

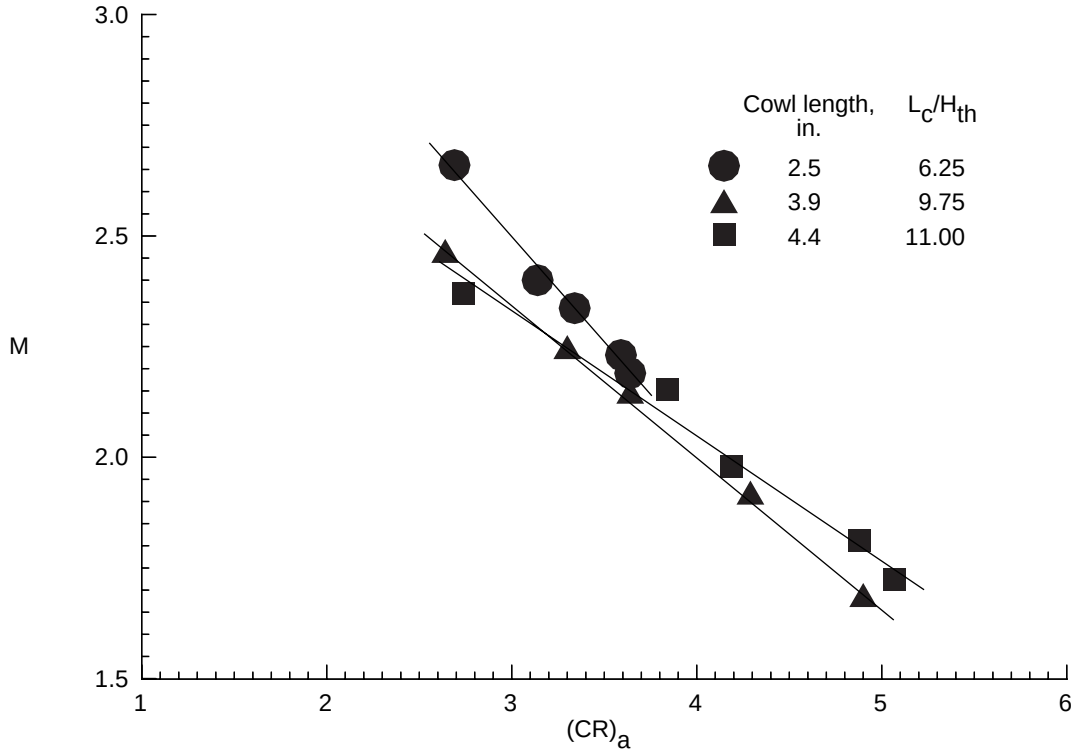

(a) Thin boundary layer.

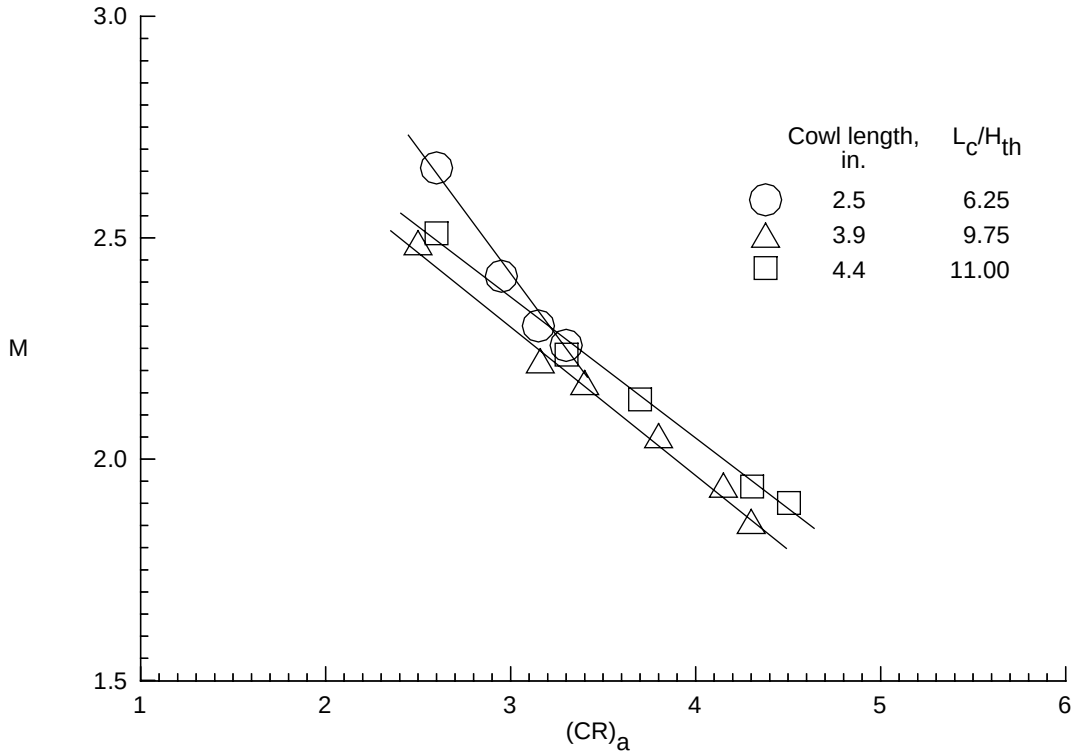

(b) Thick boundary layer.

Figure 13. Inlet throat Mach number versus inlet contraction ratio for 2.5-, 3.9-, and 4.4-in. cowls. Linear curve fit through data.

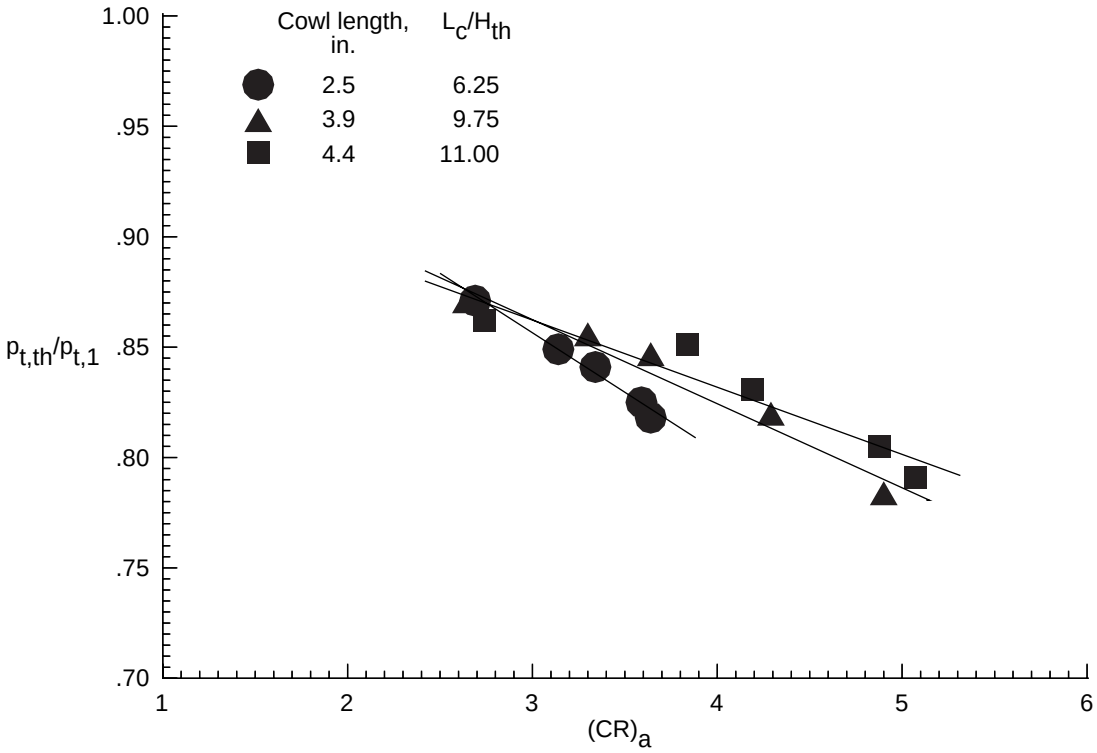

(a) Thin boundary layer.

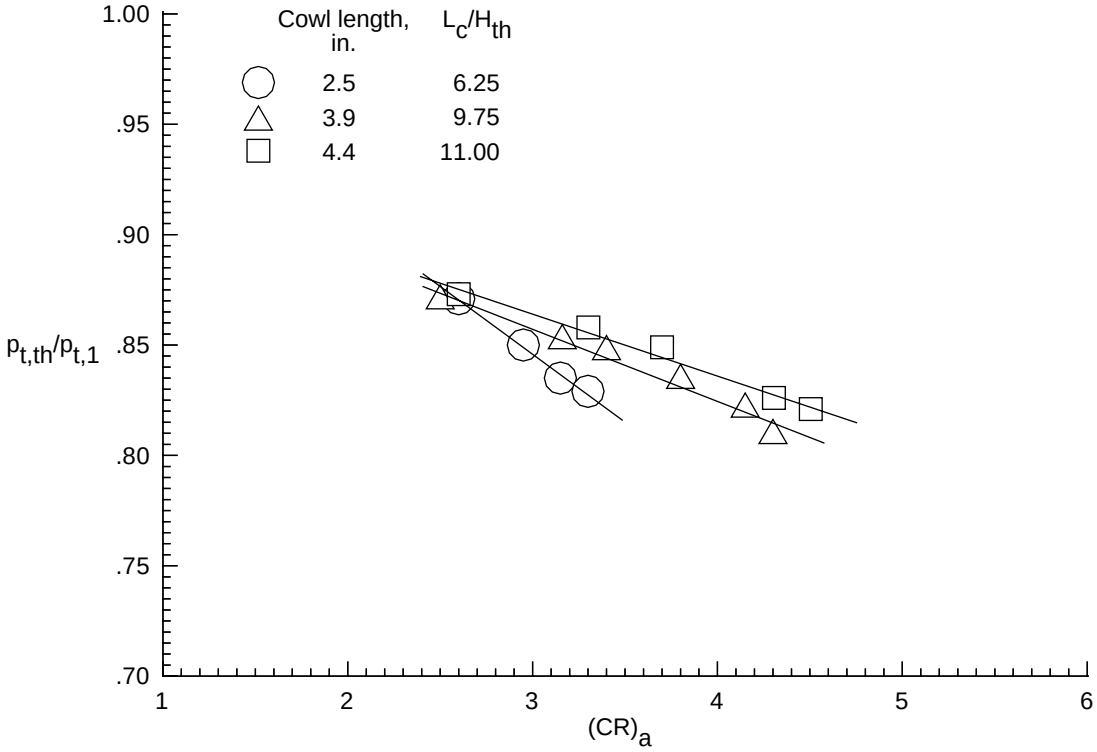

(b) Thick boundary layer.

Figure 14. Inlet throat total pressure recovery versus inlet contraction ratio for 2.5-, 3.9-, and 4.4-in. cowls. Linear curve fit through data.

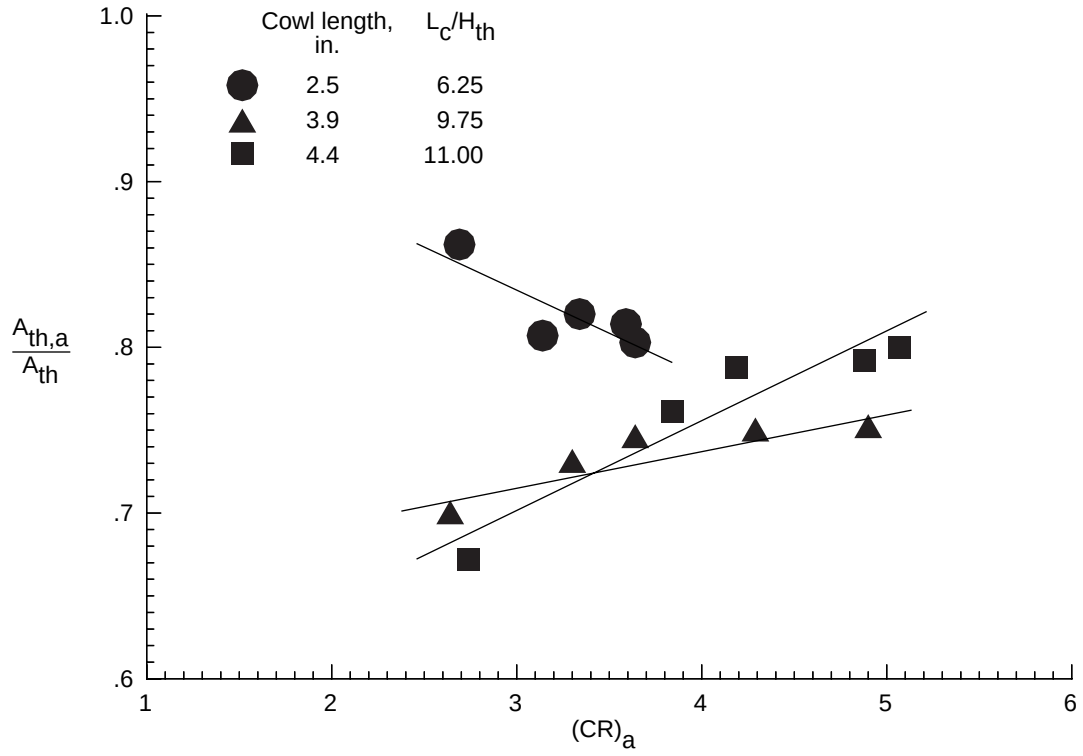

(a) Thin boundary layer.

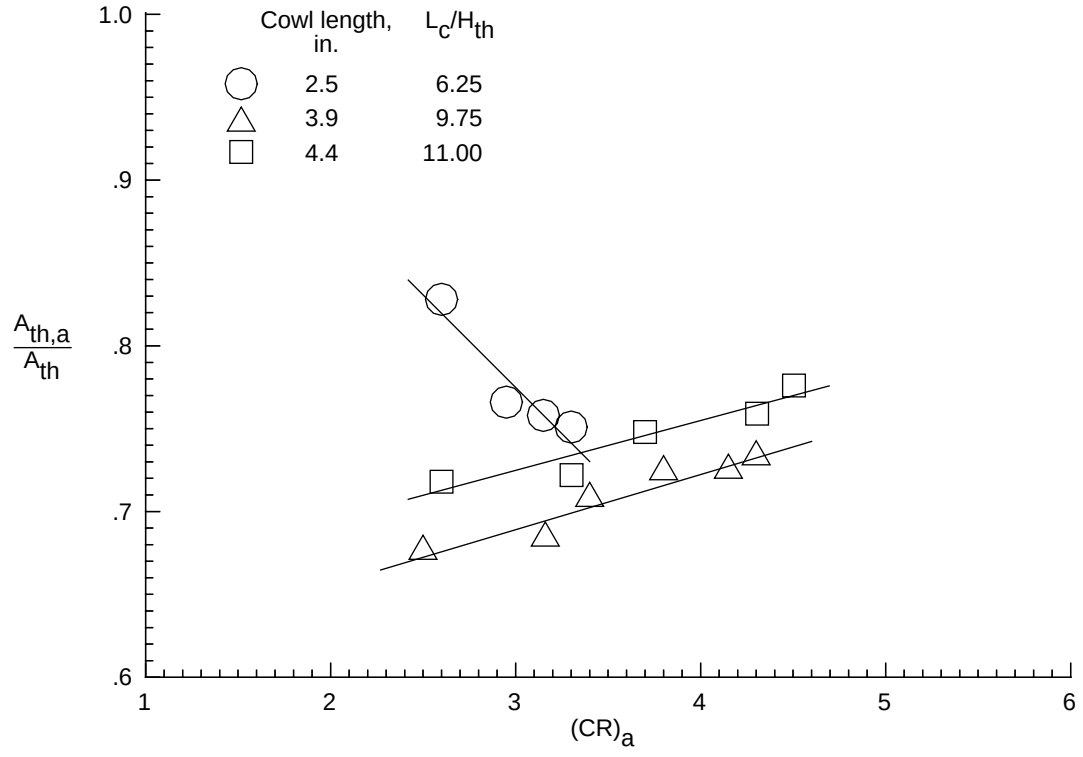

(b) Thick boundary layer.

Figure 15. Inlet throat vena contracta coefficient versus inlet contraction ratio for 2.5-, 3.9-, and 4.4-in. cowls. Linear curve fit through data.

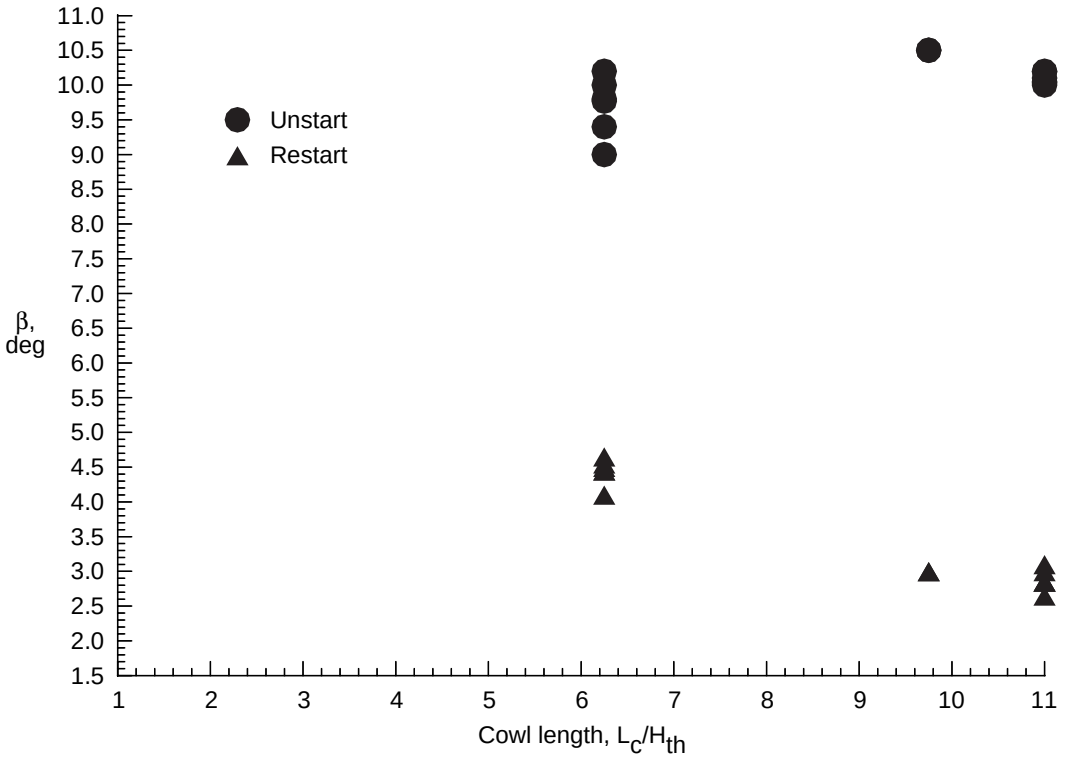

(a) Thin boundary layer (without foreplate).

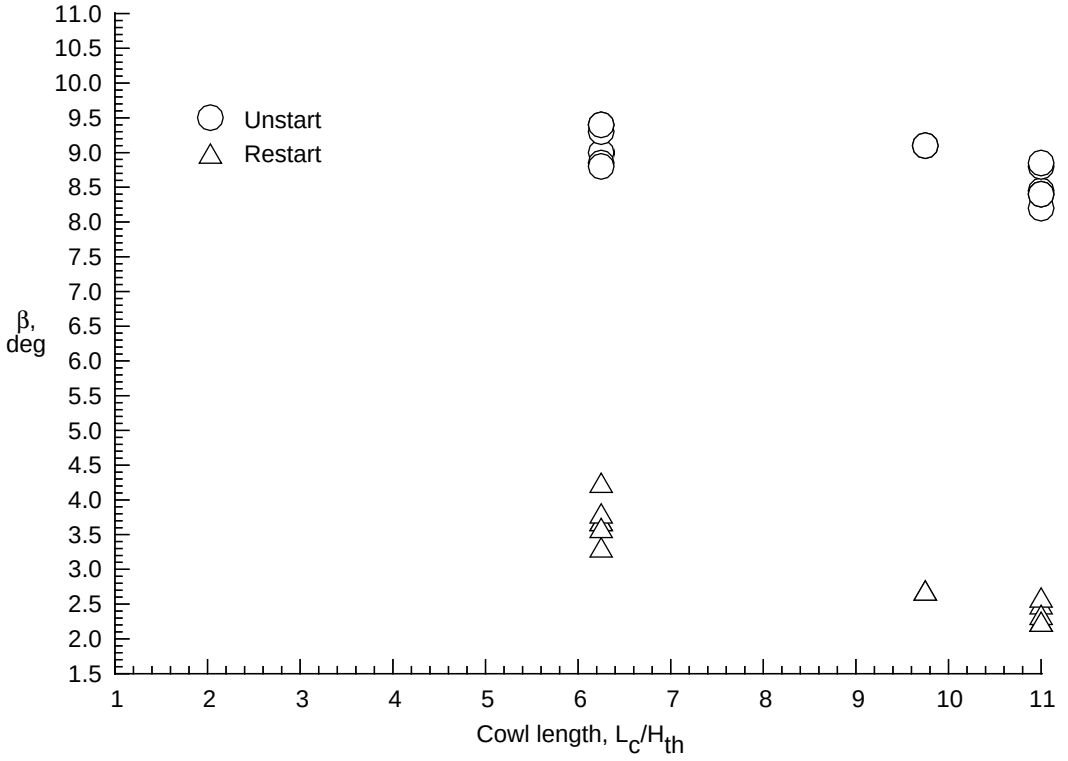

(b) Thick boundary layer (with foreplate).

Figure 16. Inlet unstart and restart convergence angle range for each cowl with thin and thick boundary layers.

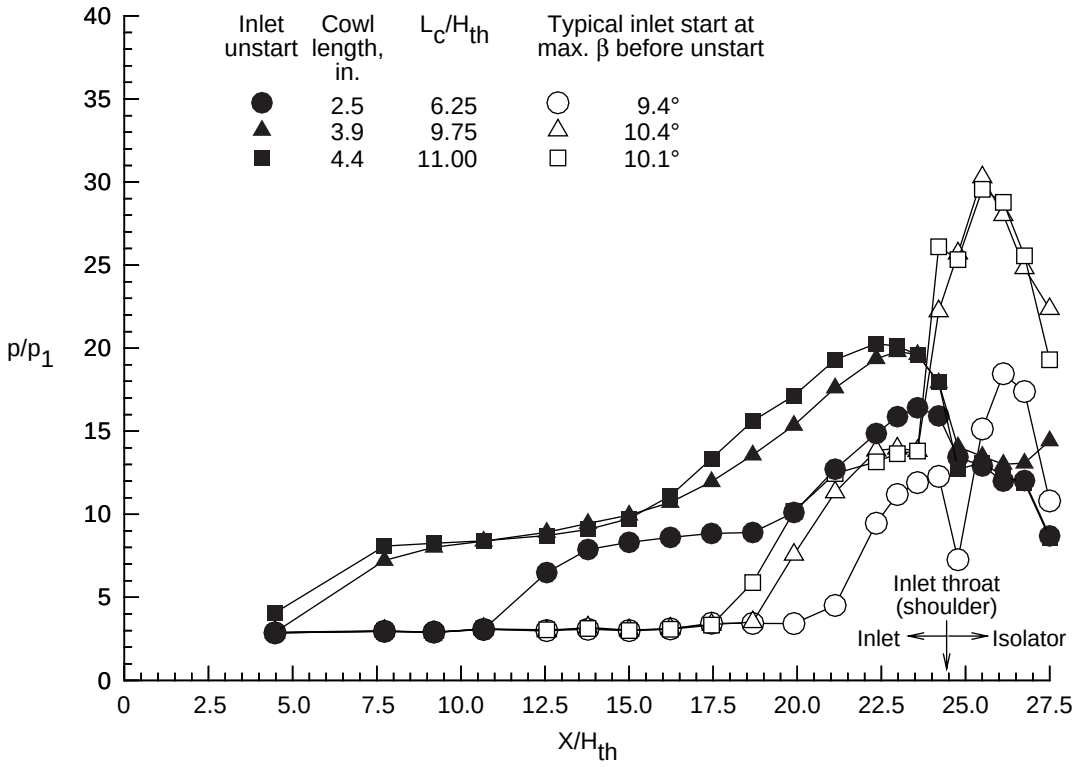

(a) Inlet ramp with thin boundary layer.

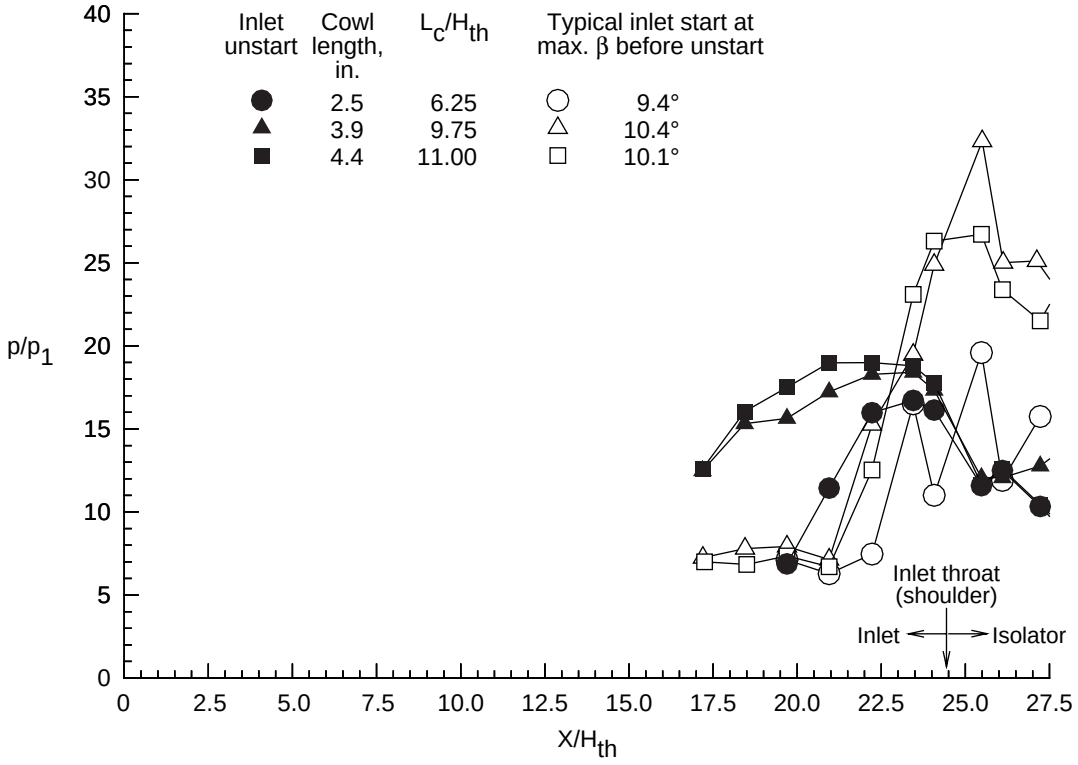

(b) Inlet cowl with thin boundary layer.

Figure 17. Inlet unstart pressure distribution for each cowl with thin and thick boundary layers.

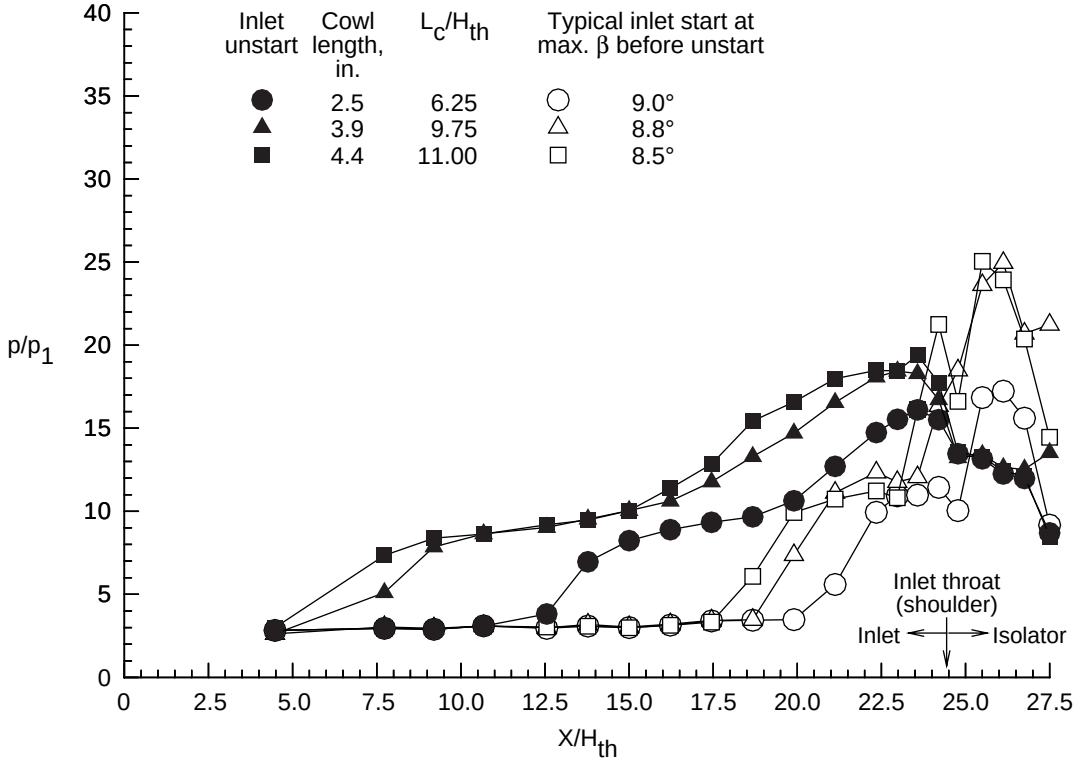

(c) Inlet ramp with thick boundary layer.

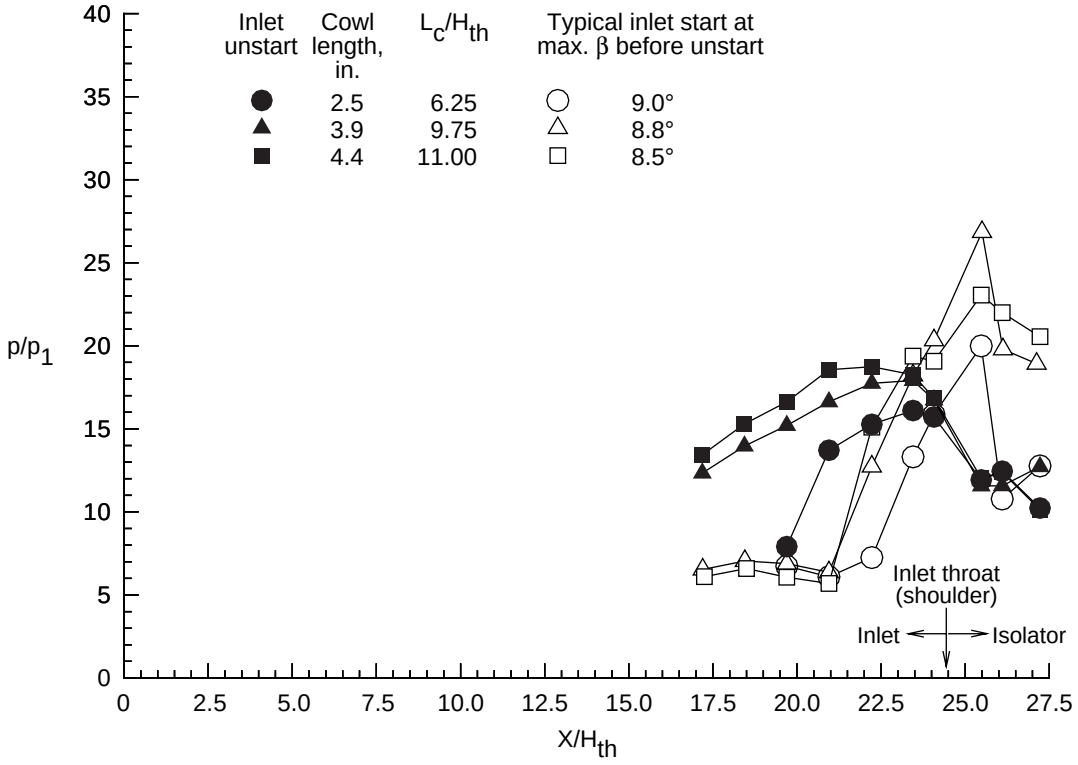

(d) Inlet cowl with thick boundary layer.

Figure 17. Concluded.

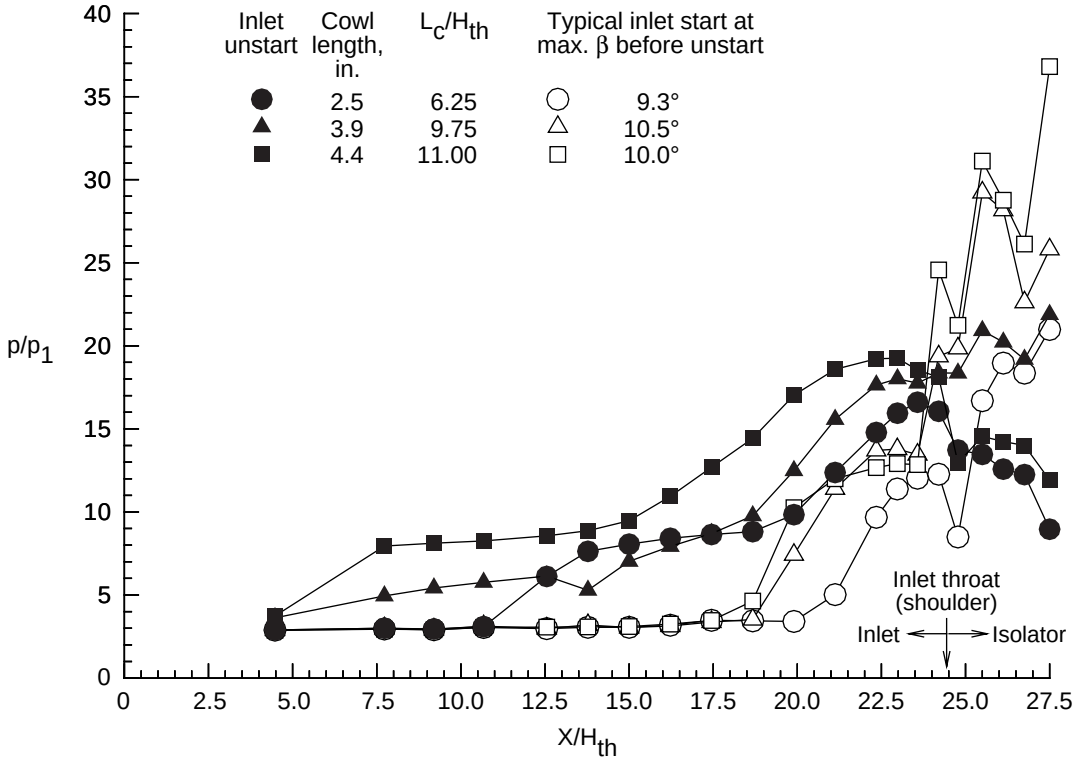

(a) Inlet ramp with thin boundary layer.

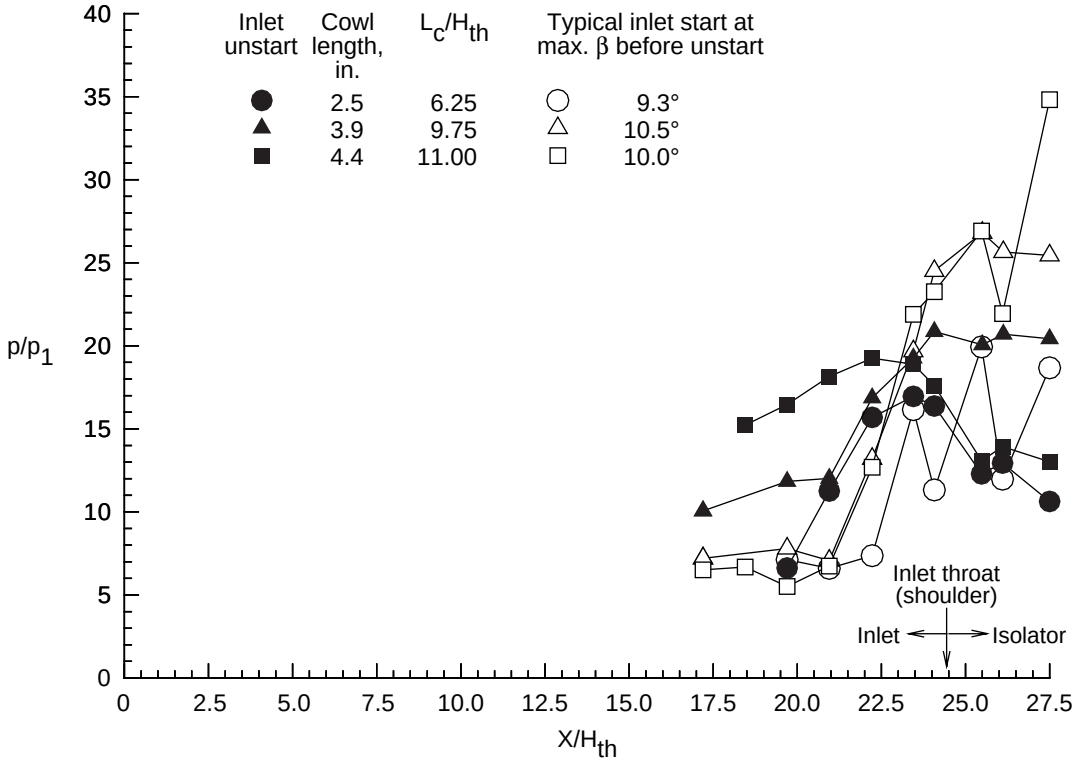

(b) Inlet cowl with thin boundary layer.

Figure 18. Back-pressure unstarted inlet pressure distribution for each cowl with thin and thick boundary layers.

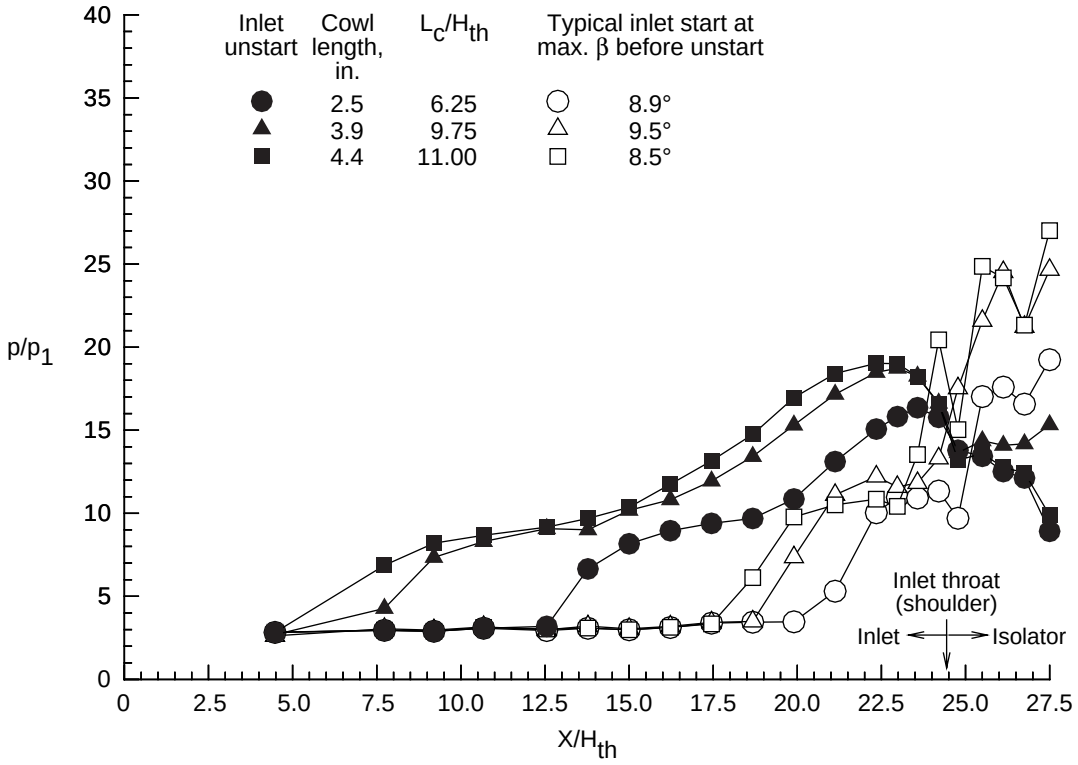

(c) Inlet ramp with thick boundary layer.

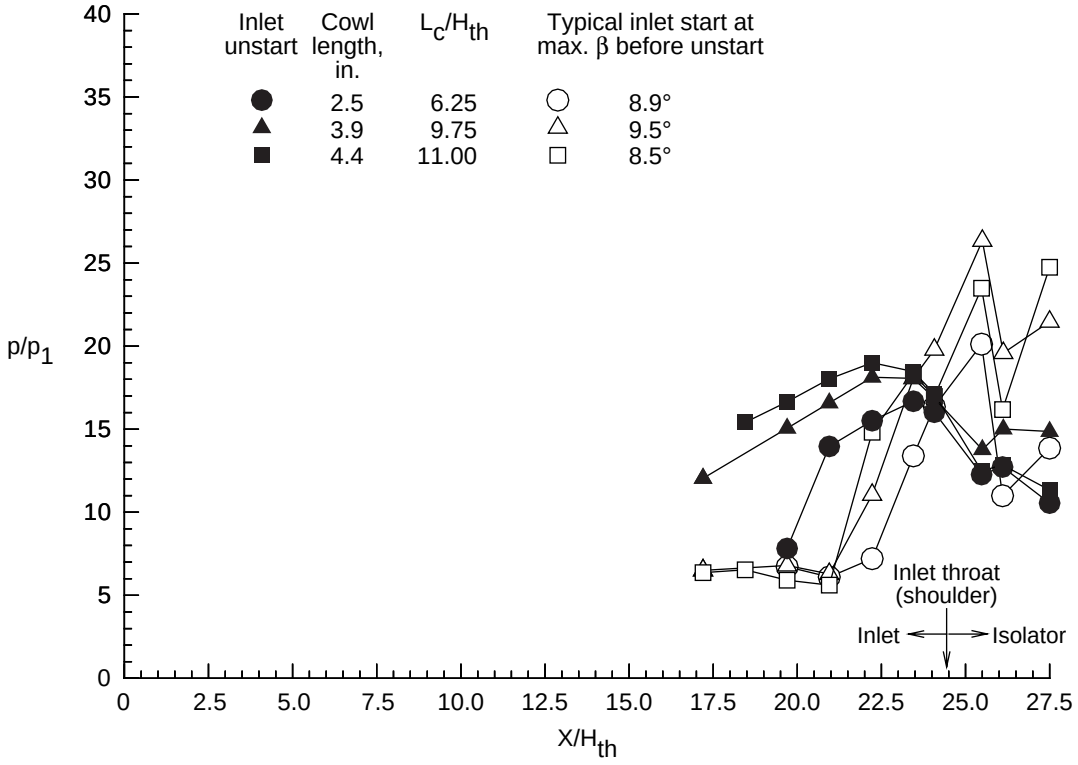

(d) Inlet cowl with thick boundary layer.

Figure 18. Concluded.

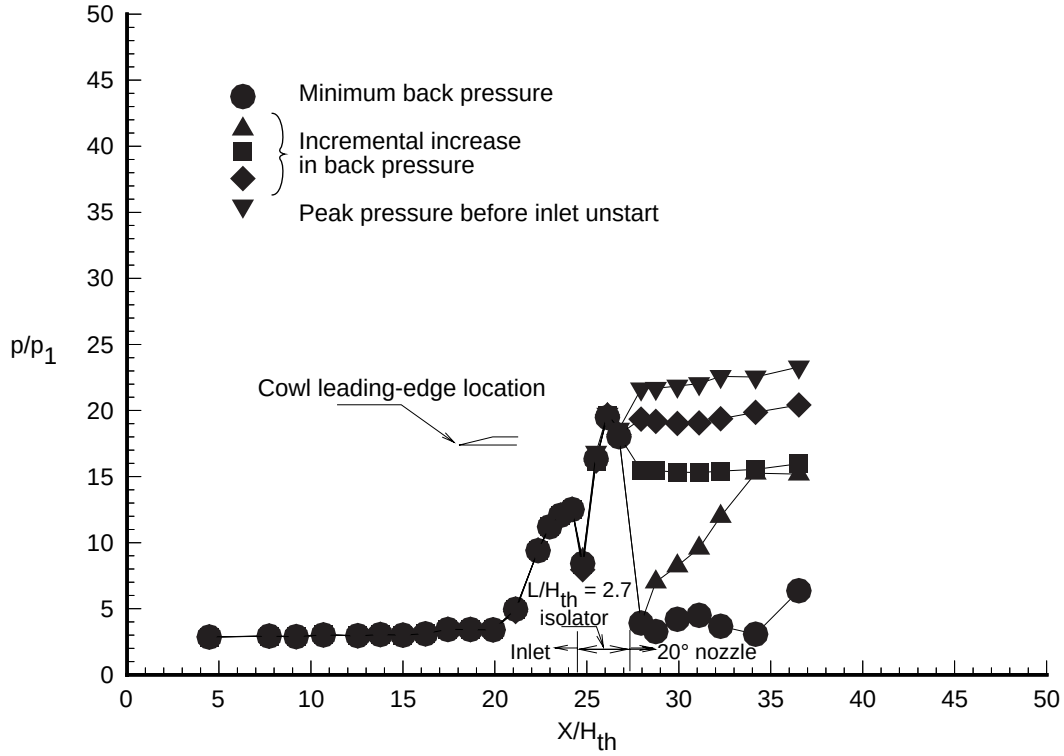

(a) Body side at β = 8.8° with L/H_{th} = 2.7. Run 40; M_{th} = 2.25; $p_{N.S.}/p_1$ = 71.75.

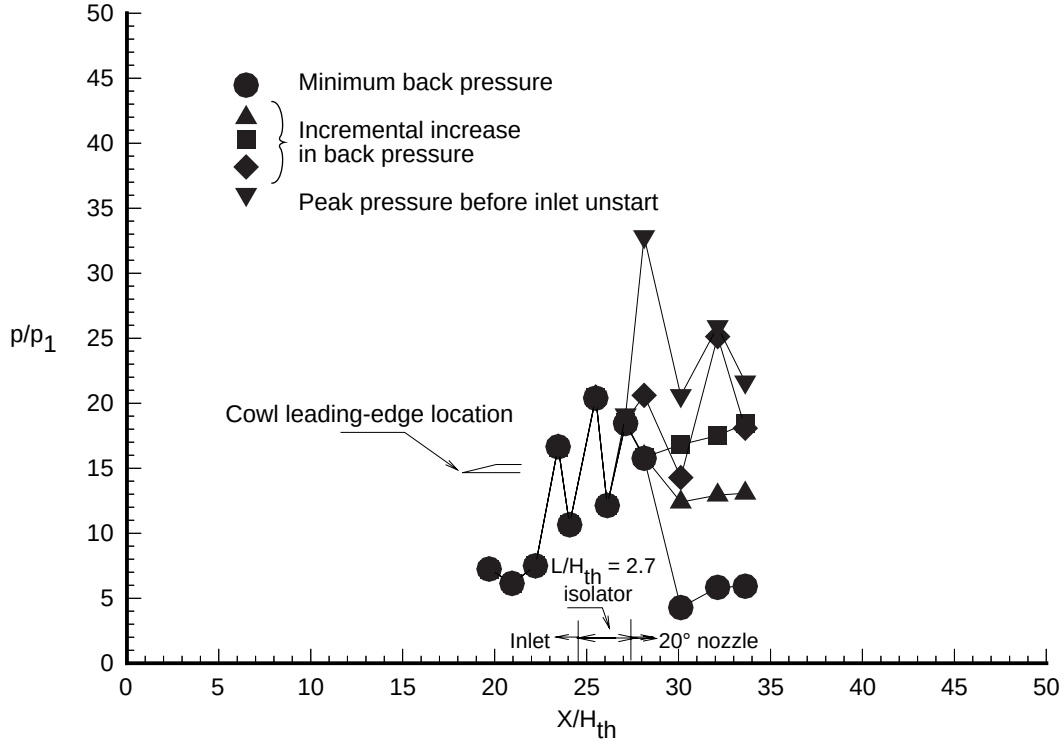

(b) Cowl side at β = 8.8° with L/H_{th} = 2.7. Run 40; M_{th} = 2.25; $p_{N.S.}/p_1$ = 71.75.

Figure 19. Back-pressure effects for 2.5-in. cowl (L_c/H_{th} = 6.25) with thin boundary layer and high inlet convergence angle (β = 8.4°–8.8°) for L/H_{th} = 2.7, 4.7, 8.7, and 16.7, and also for L/H_{th} = 4.7 followed by divergence angle of 6°. Constant-area isolator.

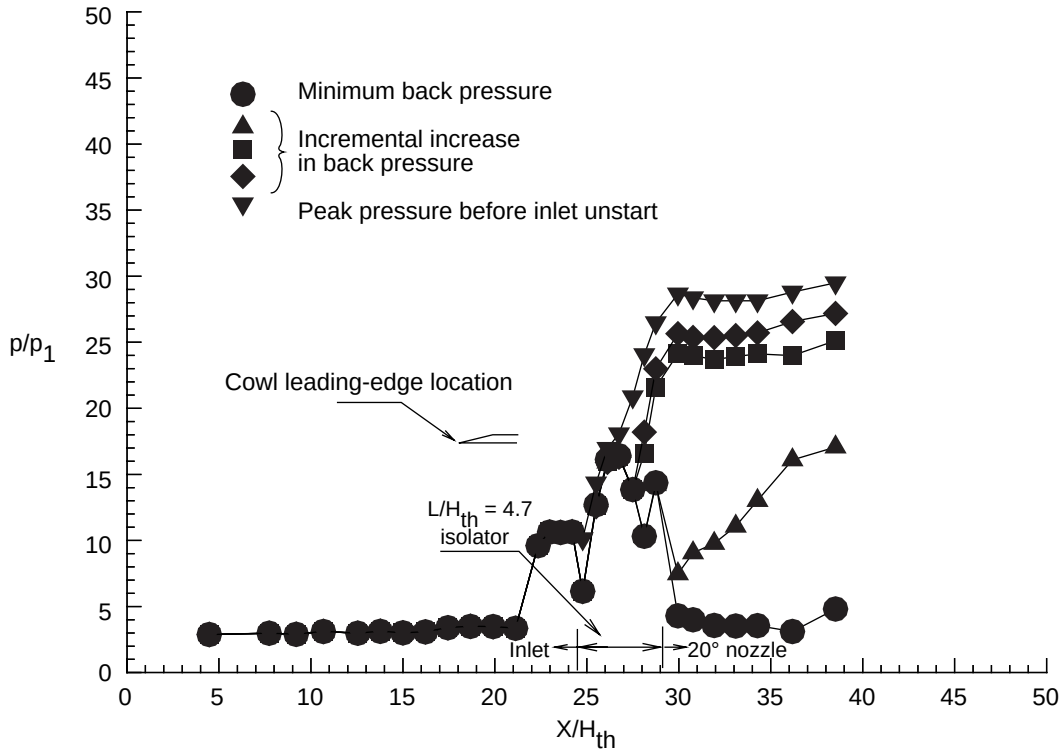

(c) Body side at β = 8.4° with L/H_{th} = 4.7. Run 110; M_{th} = 2.29; $p_{N.S.}/p_1$ = 62.50.

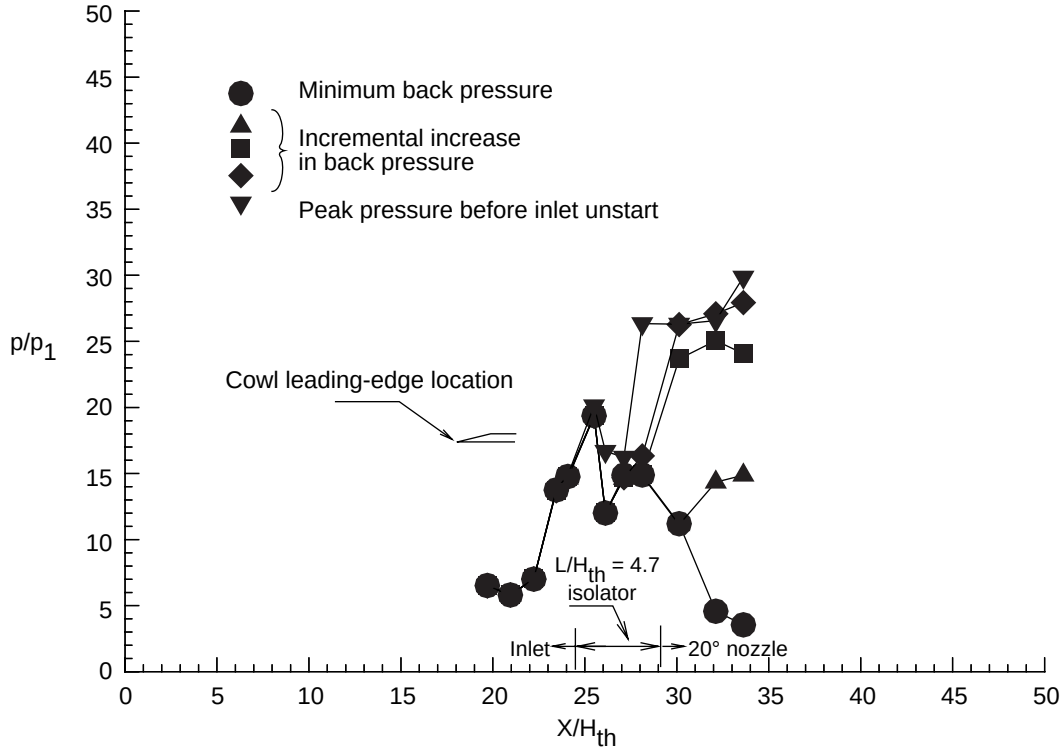

(d) Cowl side at β = 8.4° with L/H_{th} = 4.7. Run 110; M_{th} = 2.29; $p_{N.S.}/p_1$ = 62.50.

Figure 19. Continued.

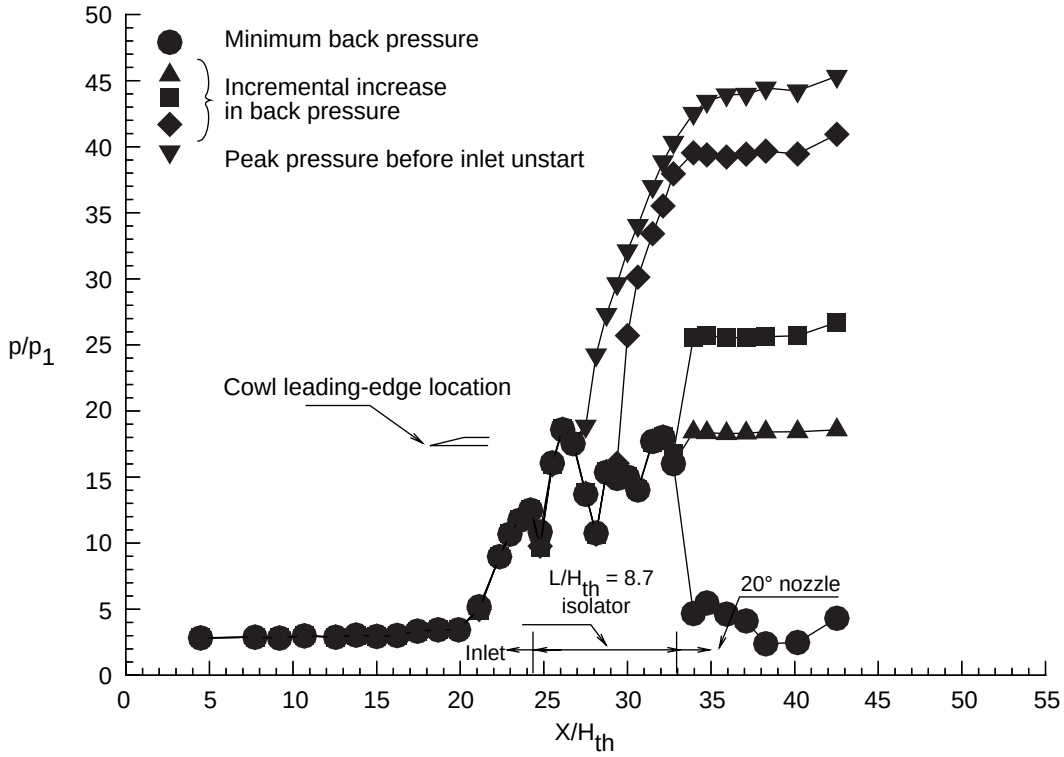

(e) Body side at β = 8.7° with L/H_{th} = 8.7. Run 6; M_{th} = 2.26; $p_{N.S.}/p_1$ = 70.0.

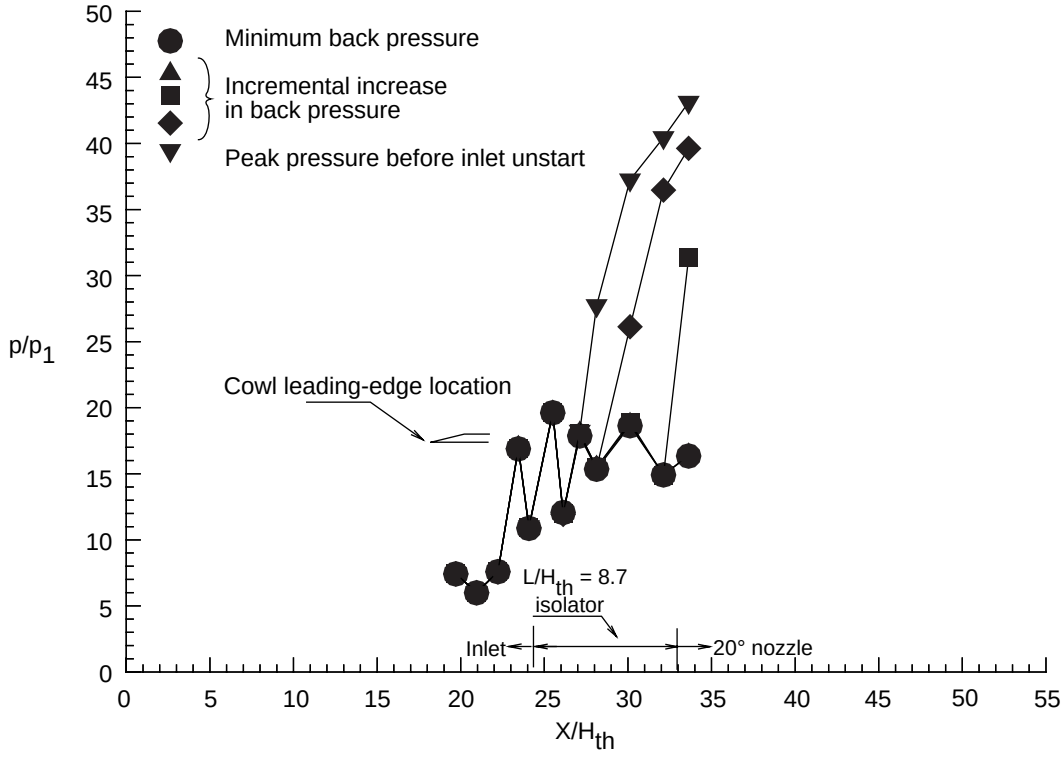

(f) Cowl side at β = 8.7° with L/H_{th} = 8.7. Run 6; M_{th} = 2.26; $p_{N.S.}/p_1$ = 70.0.

Figure 19. Continued.

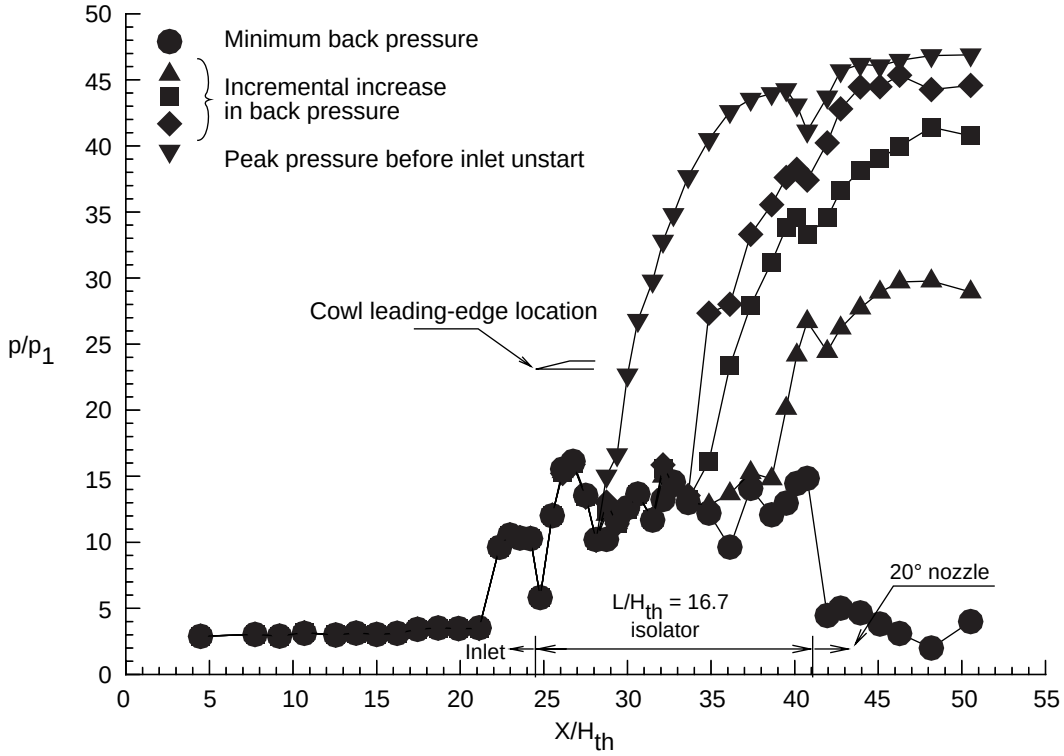

(g) Body side at β = 8.4° with L/H_{th} = 16.7. Run 140; M_{th} = 2.29; $p_{N.S.}/p_1$ = 62.5.

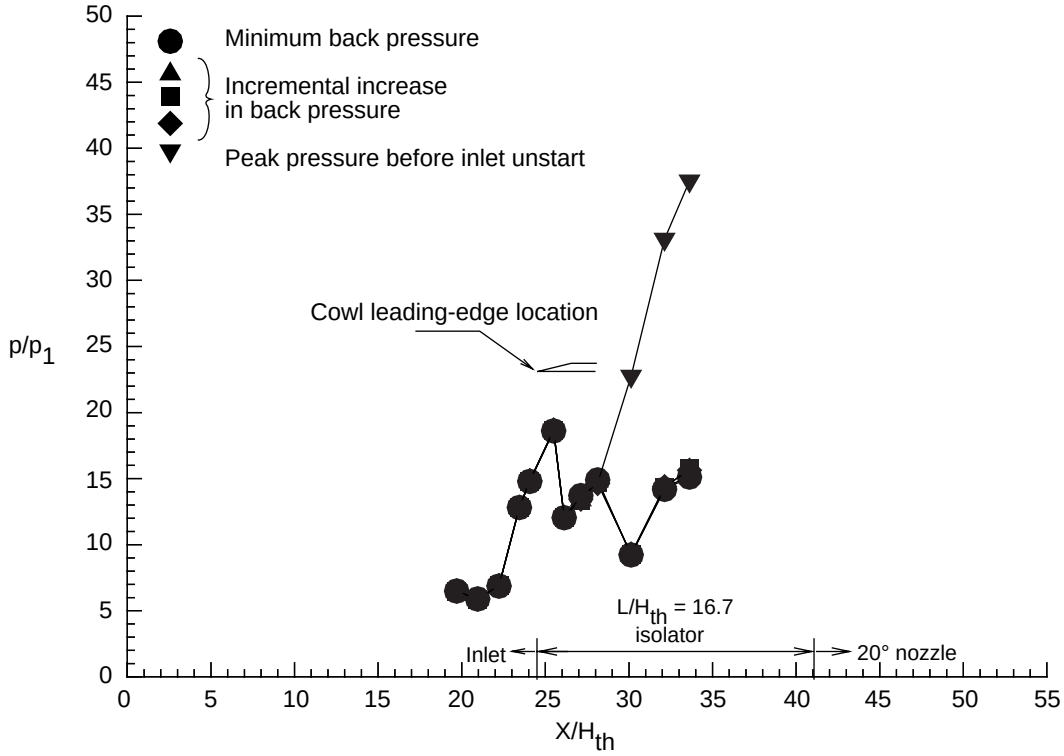

(h) Cowl side at β = 8.4° with L/H_{th} = 16.7. Run 140; M_{th} = 2.29; $p_{N.S.}/p_1$ = 62.5.

Figure 19. Continued.

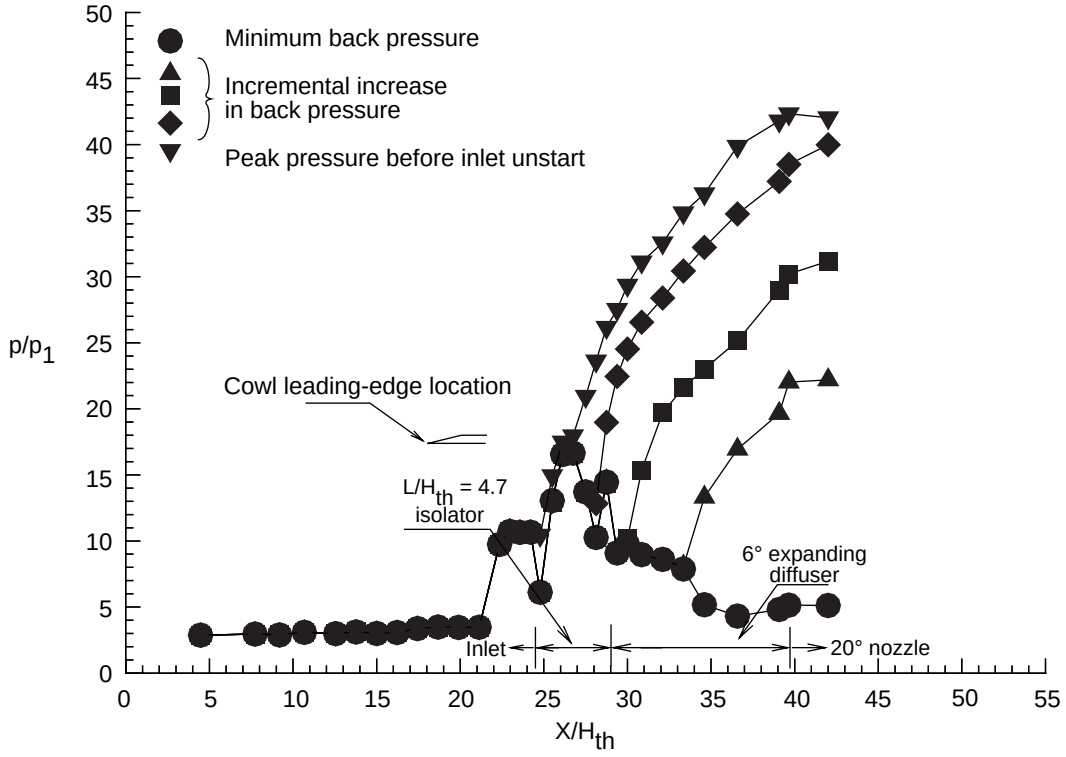

(i) Body side at β = 8.4° with L/H_{th} = 4.7 followed by angle of 6° divergence. Run 115; M_{th} = 2.29; $p_{N.S.}/p_1$ = 62.5.

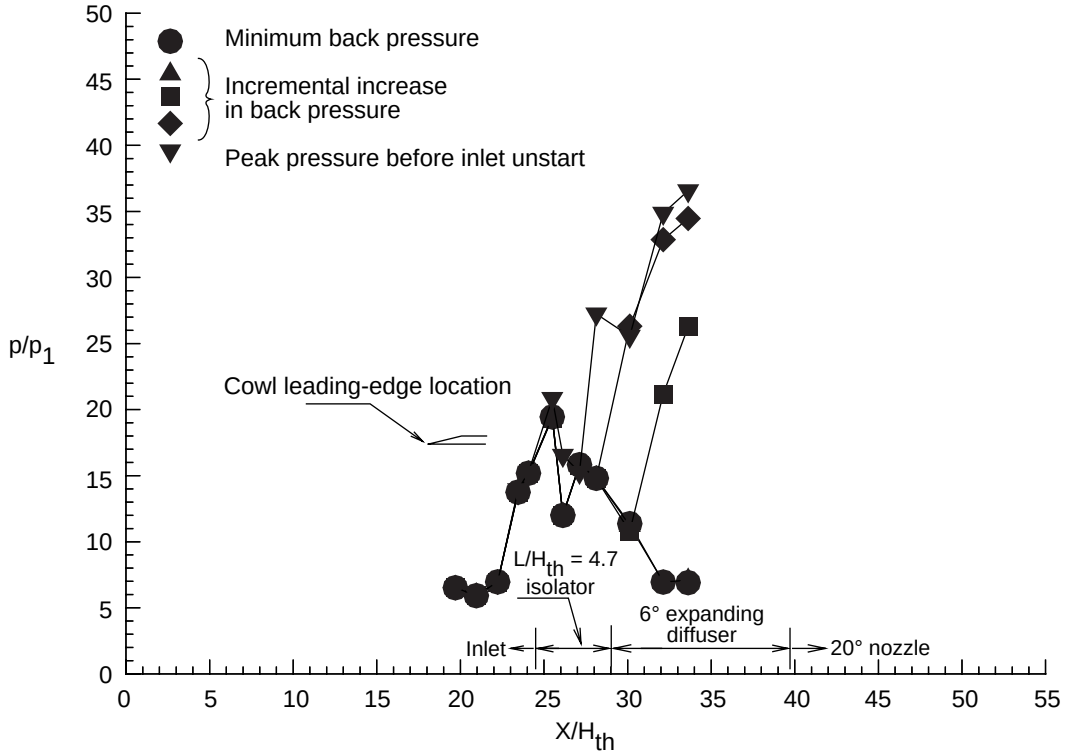

(j) Cowl side at β = 8.4° with L/H_{th} = 4.7 followed by angle of 6° divergence. Run 115; M_{th} = 2.29; $p_{N.S.}/p_1$ = 62.5.

Figure 19. Concluded.

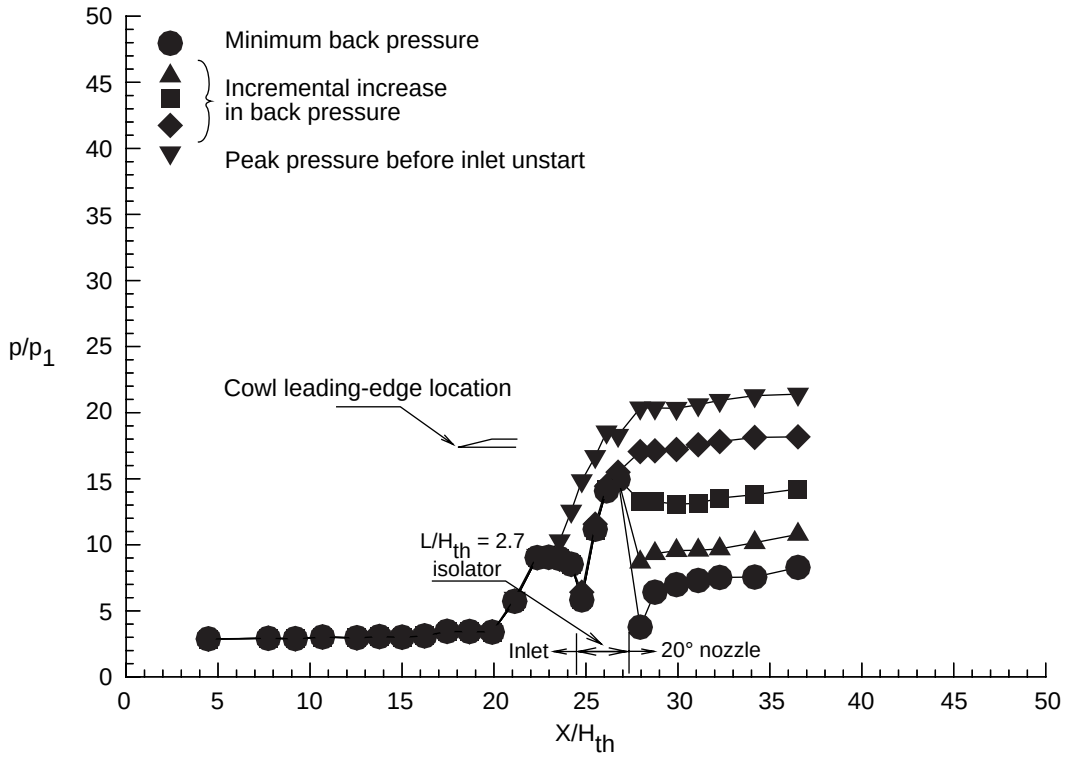

(a) Body side at β = 6° with L/H_{th} = 2.7. Run 40; M_{th} = 2.40; $p_{N.S.}/p_1$ = 56.0.

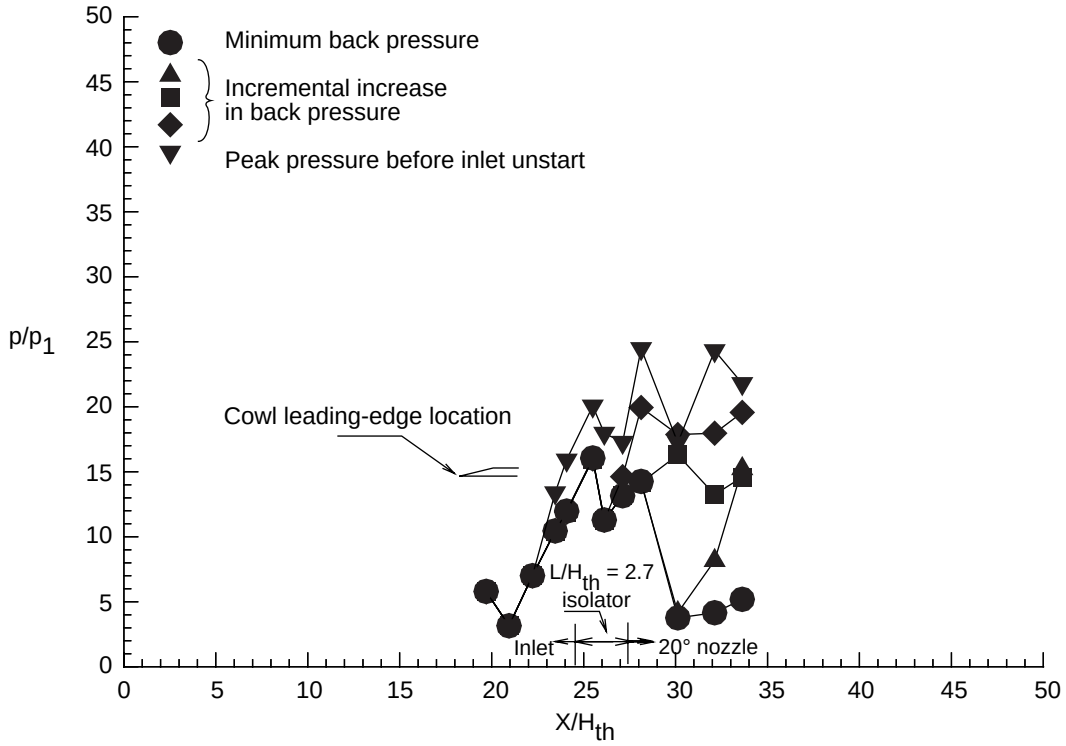

(b) Cowl side at β = 6° with L/H_{th} = 2.7. Run 40; M_{th} = 2.40; $p_{N.S.}/p_1$ = 56.0.

Figure 20. Back-pressure effects for 2.5-in. cowl (L_c/H_{th} = 2.7) with thin boundary layer and medium inlet convergence angle (β = 5.0°–6.0°) for L/H_{th} = 2.7, 4.7, 8.7, and 16.7, and also for L/H_{th} = 4.7 followed by divergence angle of 6°. Constant-area isolator.

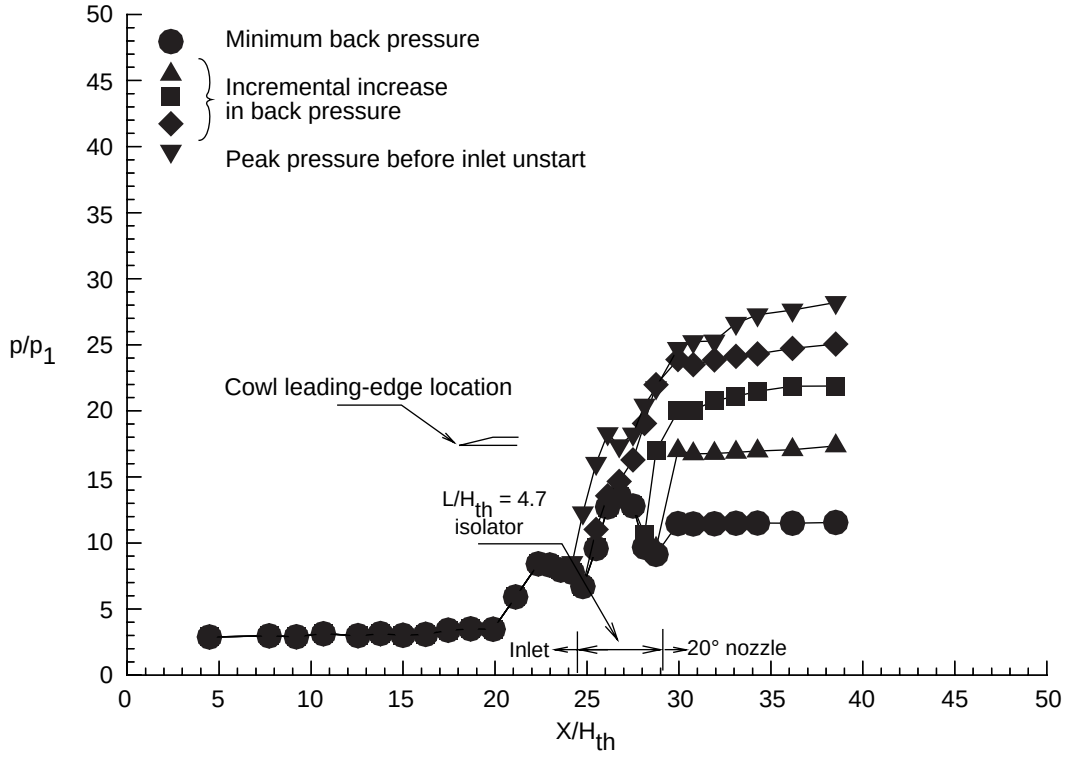

(c) Body side at β = 6° with L/H_{th} = 4.7. Run 112; M_{th} = 2.40; $p_{N.S.}/p_1$ = 56.0.

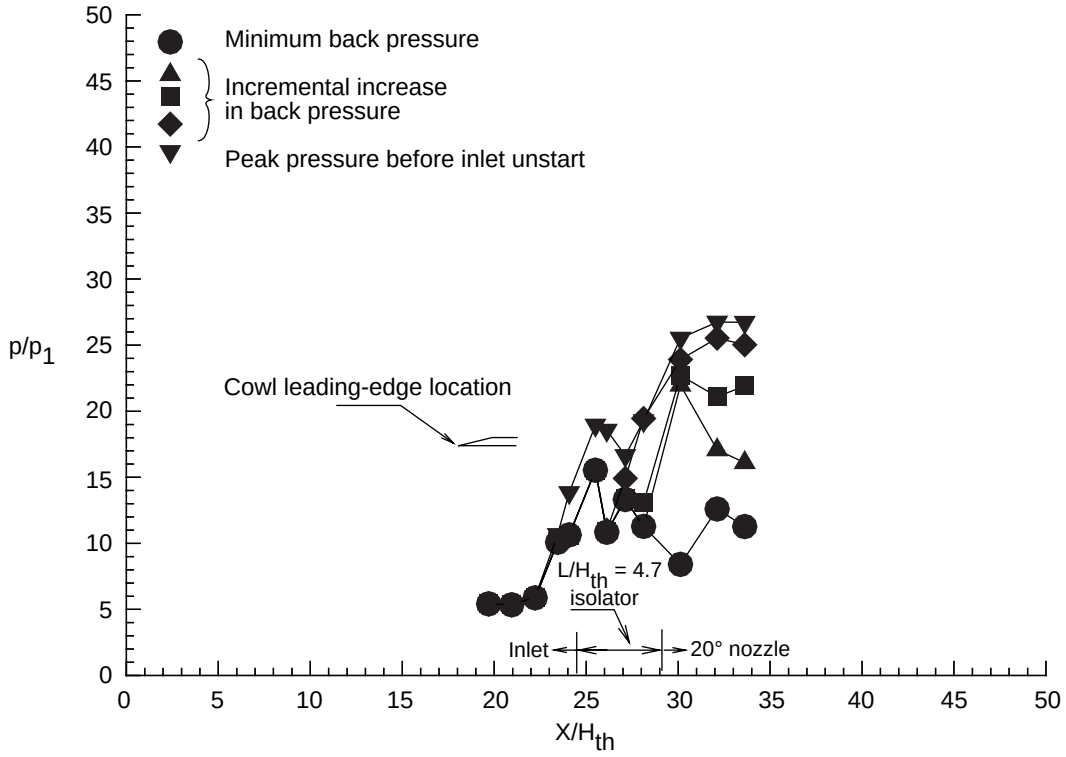

(d) Cowl side at β = 6° with L/H_{th} = 4.7. Run 112; M_{th} = 2.40; $p_{N.S.}/p_1$ = 56.0.

Figure 20. Continued.

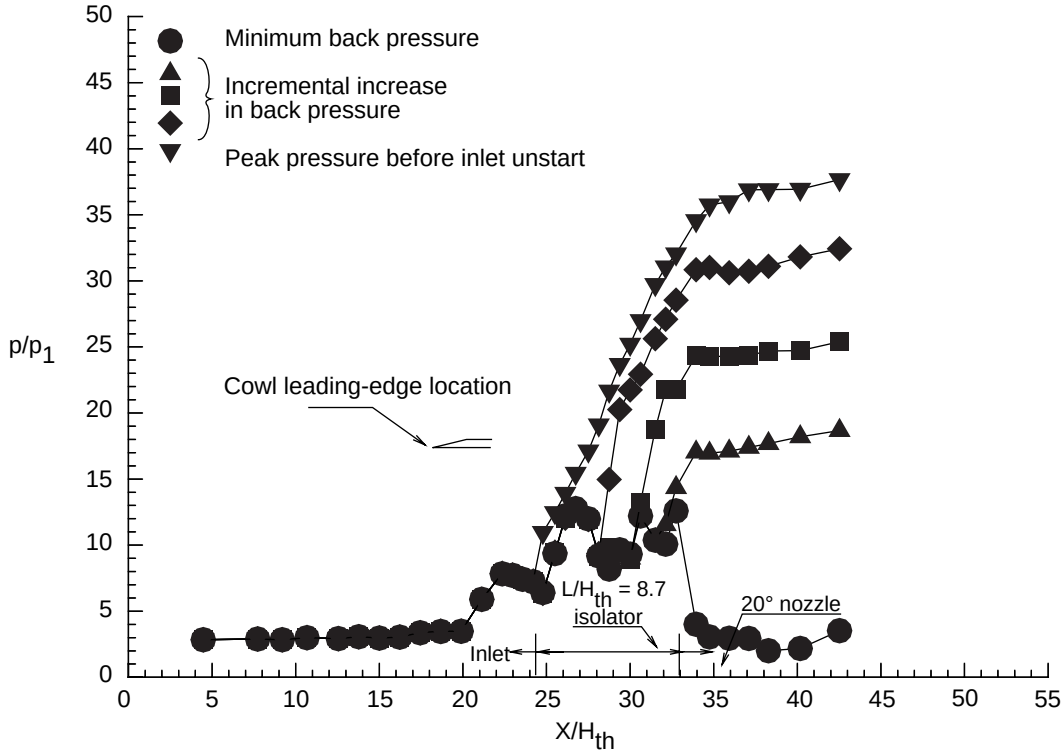

(e) Body side at β = 5° with L/H_{th} = 8.7. Run 5; M_{th} = 2.403; $p_{N.S.}/p_1$ = 52.0.

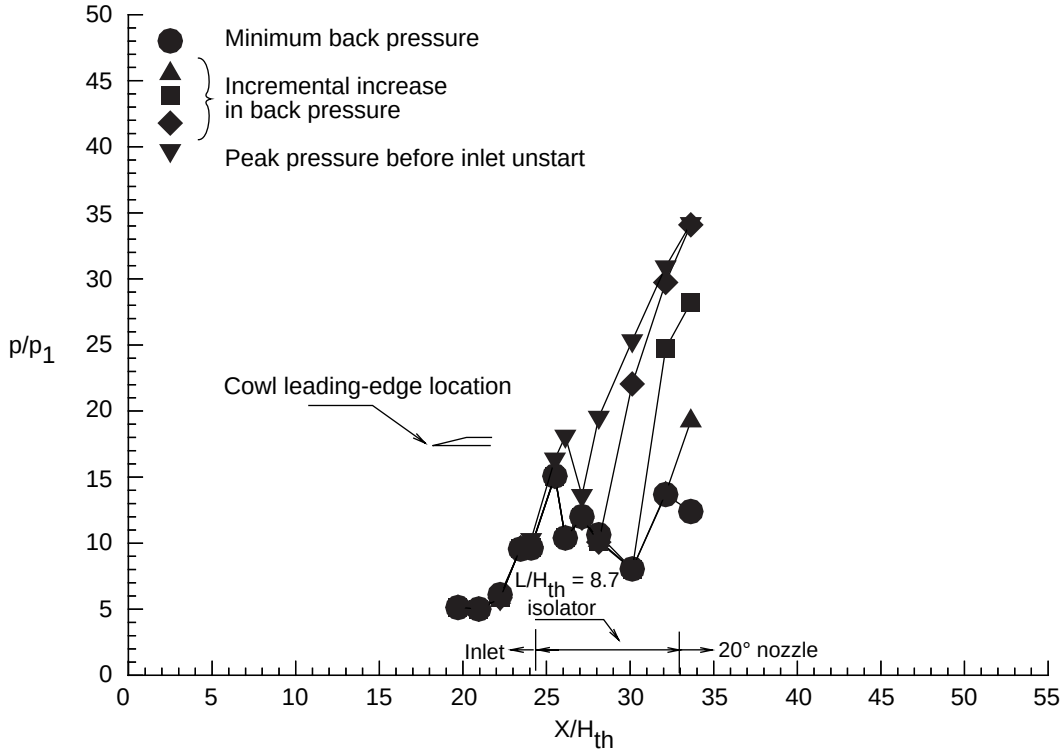

(f) Cowl side at β = 5° with L/H_{th} = 8.7. Run 5; M_{th} = 2.403; $p_{N.S.}/p_1$ = 52.0.

Figure 20. Continued.

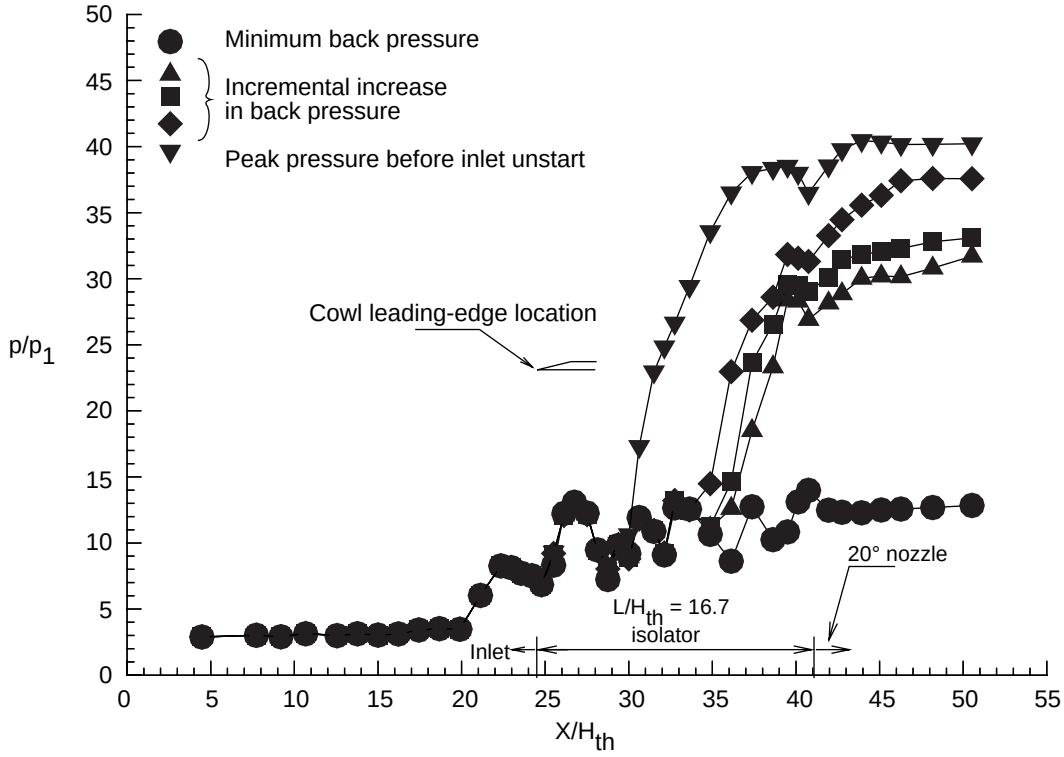

(g) Body side at β = 6° with L/H_{th} = 16.7. Run 141; M_{th} = 2.40; $p_{N.S.}/p_1$ = 56.0.

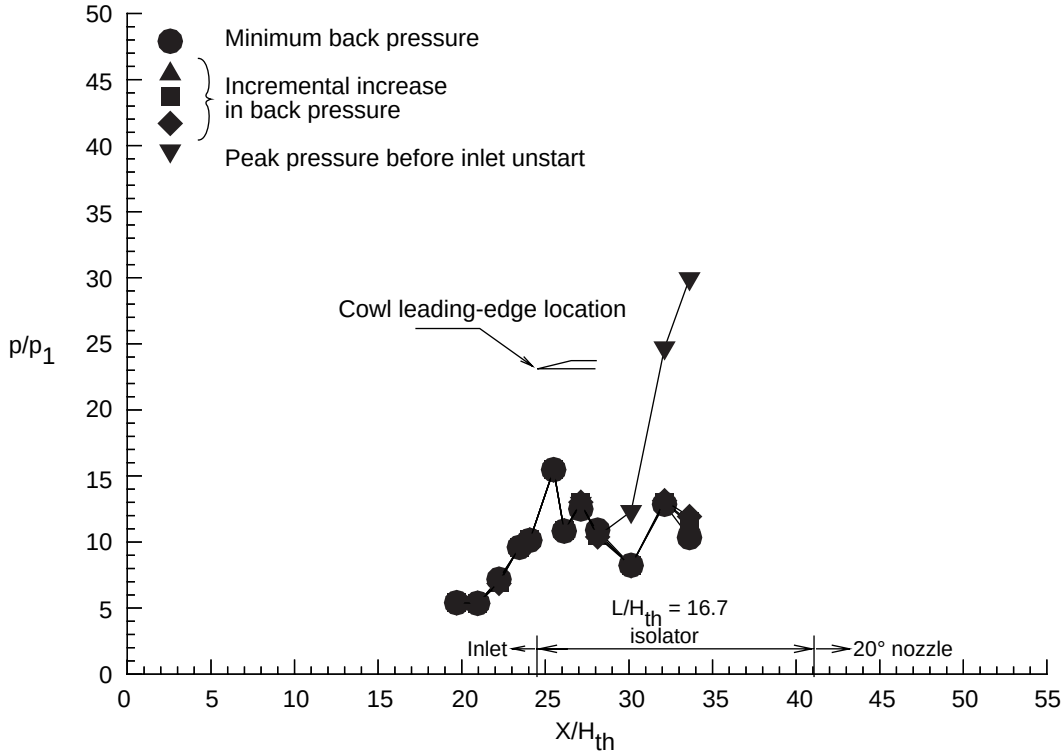

(h) Cowl side at β = 6° with L/H_{th} = 16.7. Run 141; M_{th} = 2.40; $p_{N.S.}/p_1$ = 56.0.

Figure 20. Continued.

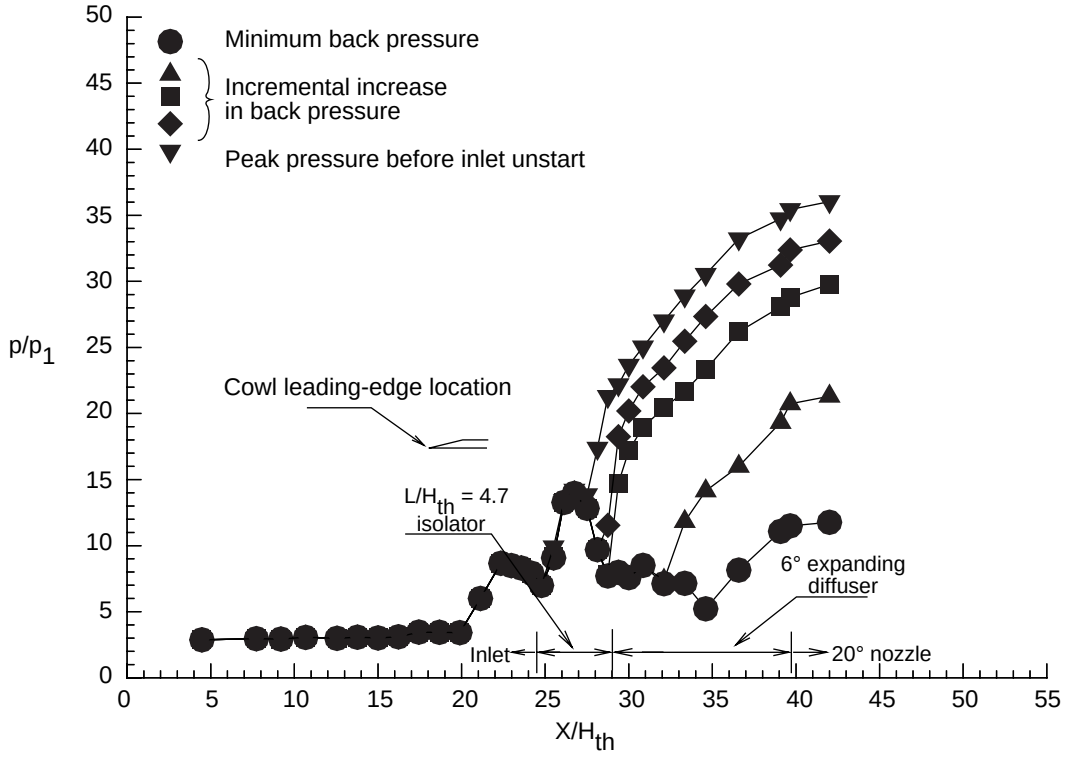

(i) Body side at β = 6° with L/H_{th} = 4.7 followed by angle of 6° divergence. Run 116; M_{th} = 2.40; $p_{N.S.}/p_1$ = 56.0.

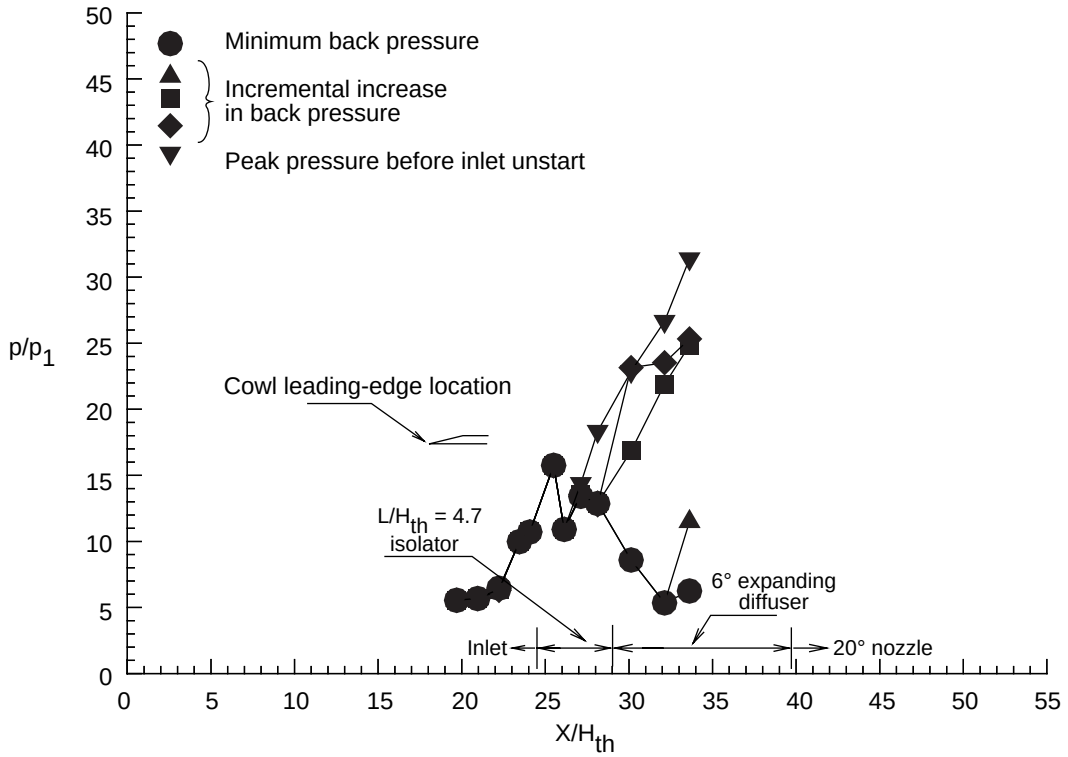

(j) Cowl side at β = 6° with L/H_{th} = 4.7 followed by angle of 6° divergence. Run 116; M_{th} = 2.40; $p_{N.S.}/p_1$ = 56.0.

Figure 20. Concluded.

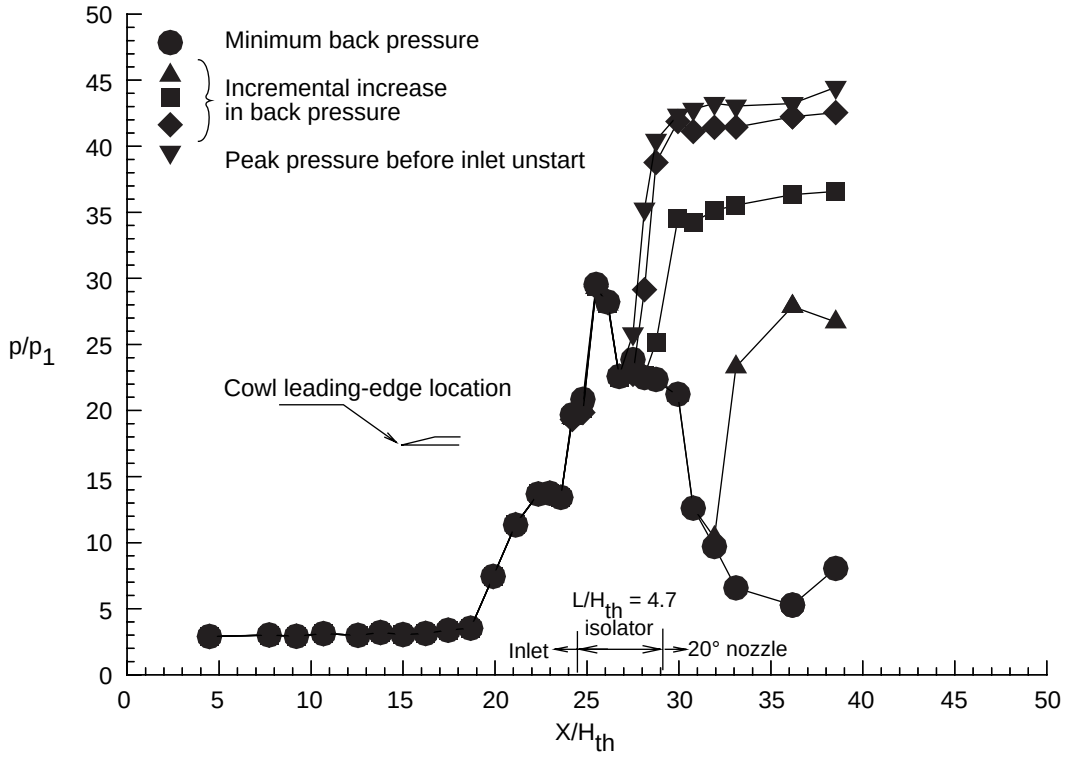

(a) Body side at β = 9.8° with L/H_{th} = 4.7. Run 188; M_{th} = 1.70; $p_{N.S.}/p_1$ = 64.0.

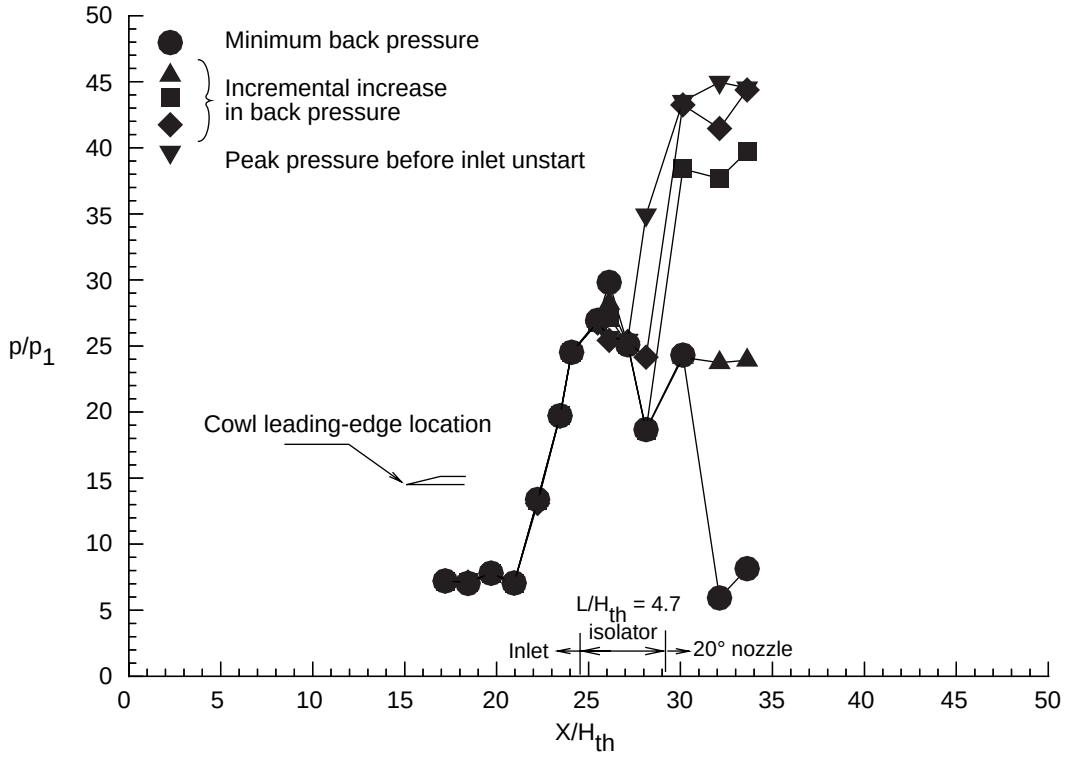

(b) Cowl side at β = 9.8° with L/H_{th} = 4.7. Run 188; M_{th} = 1.70; $p_{N.S.}/p_1$ = 64.0.

Figure 21. Back-pressure effects for 3.9-in. cowl (L_c/H_{th} = 9.75) with thin boundary layer and high inlet convergence angle (β = 9.8°) for L/H_{th} = 4.7. Constant-area isolator.

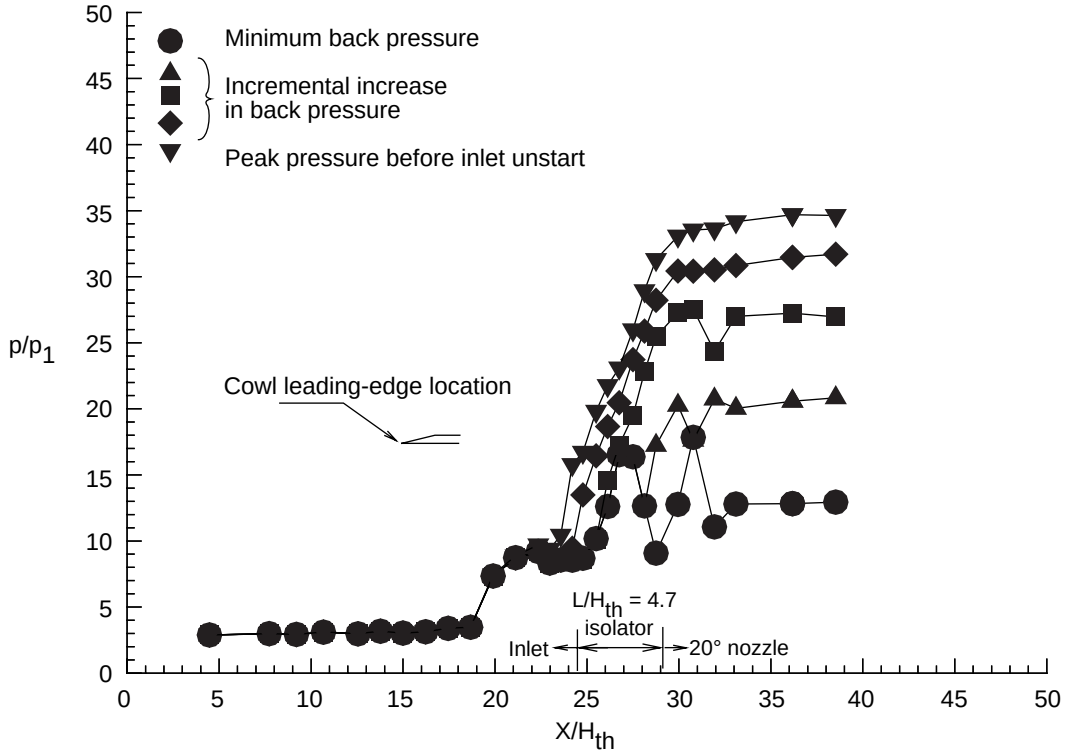

(a) Body side at β = 5.8° with L/H_{th} = 4.7. Run 189; M_{th} = 2.15; $p_{N.S.}/p_1$ = 68.0.

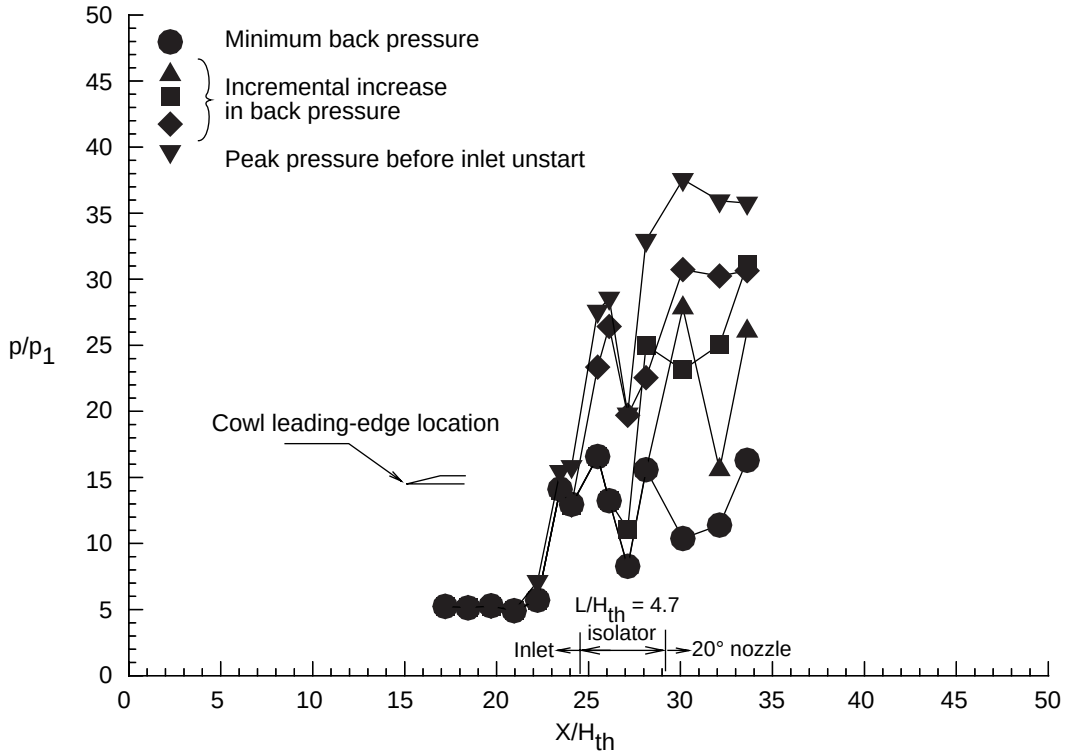

(b) Cowl side at β = 5.8° with L/H_{th} = 4.7. Run 189; M_{th} = 2.15; $p_{N.S.}/p_1$ = 68.0.

Figure 22. Back-pressure effects for 3.9-in. cowl (L_c/H_{th} = 9.75) with thin boundary layer and medium inlet convergence angle (β = 5.8°) for L/H_{th} = 4.7. Constant-area isolator.

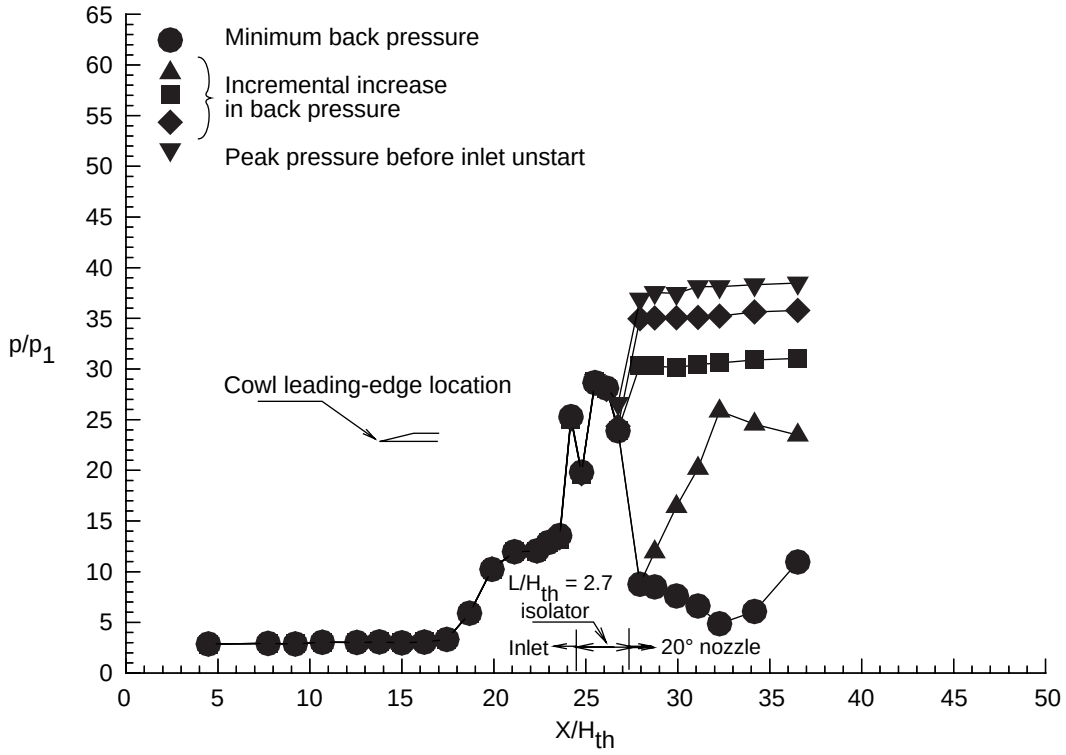

(a) Body side at β = 9.8° with L/H_{th} = 2.7. Run 48; M_{th} = 1.71; $p_{N.S.}/p_1$ = 80.20.

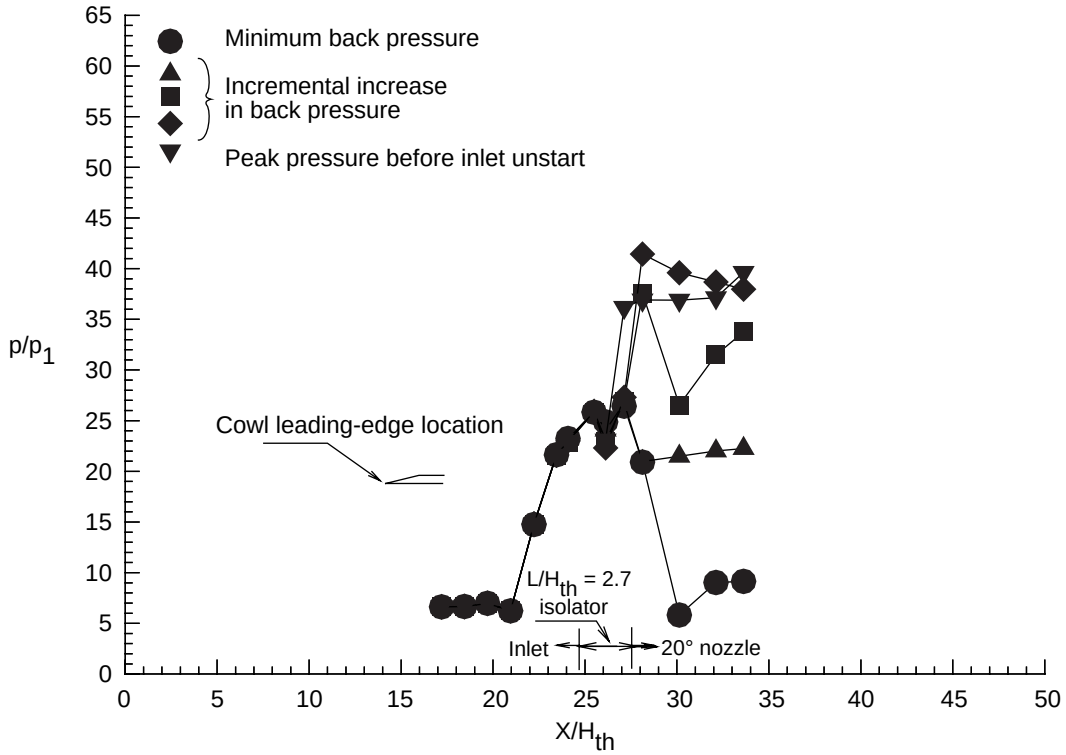

(b) Cowl side at β = 9.8° with L/H_{th} = 2.7. Run 48; M_{th} = 1.71; $p_{N.S.}/p_1$ = 80.20.

Figure 23. Back-pressure effects for 4.4-in. cowl (L_c/H_{th} = 11.00) with thin boundary layer and high inlet convergence angle (β = 9.3°–9.8°) for L/H_{th} = 2.7, 4.7, 8.7, and 16.7, and also for L/H_{th} = 4.7 followed by divergent angle of 6°. Constant-area isolator.

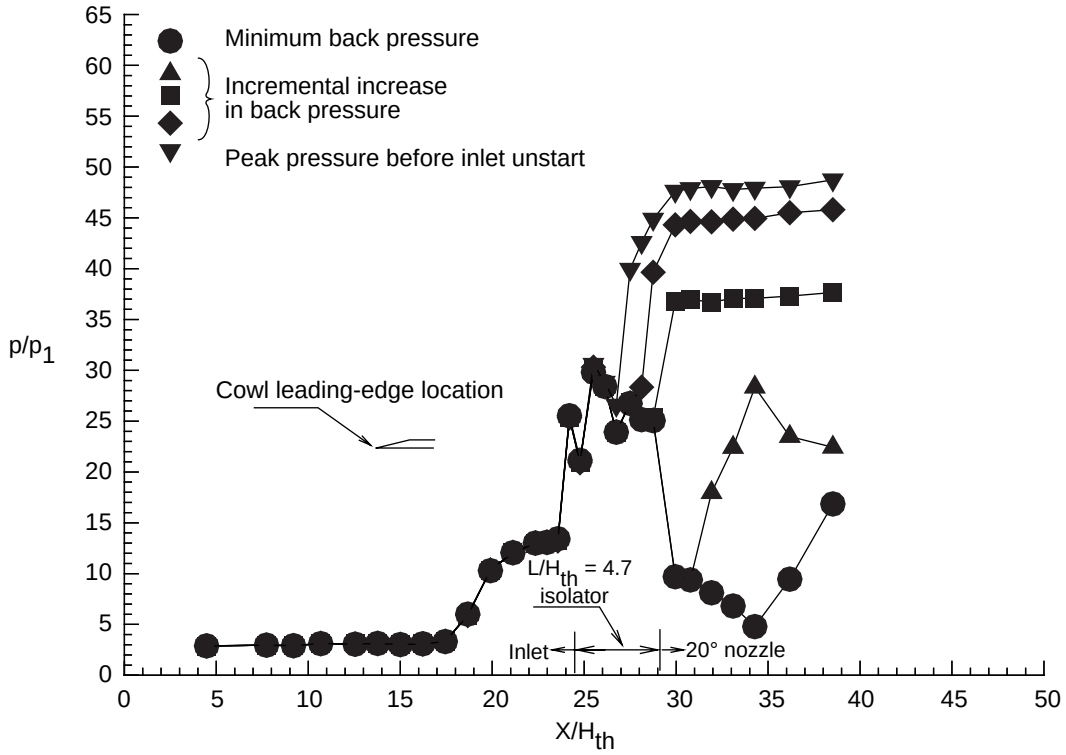

(c) Body side at β = 9.8° with L/H_{th} = 4.7. Run 107; M_{th} = 1.71; $p_{N.S.}/p_1$ = 80.20.

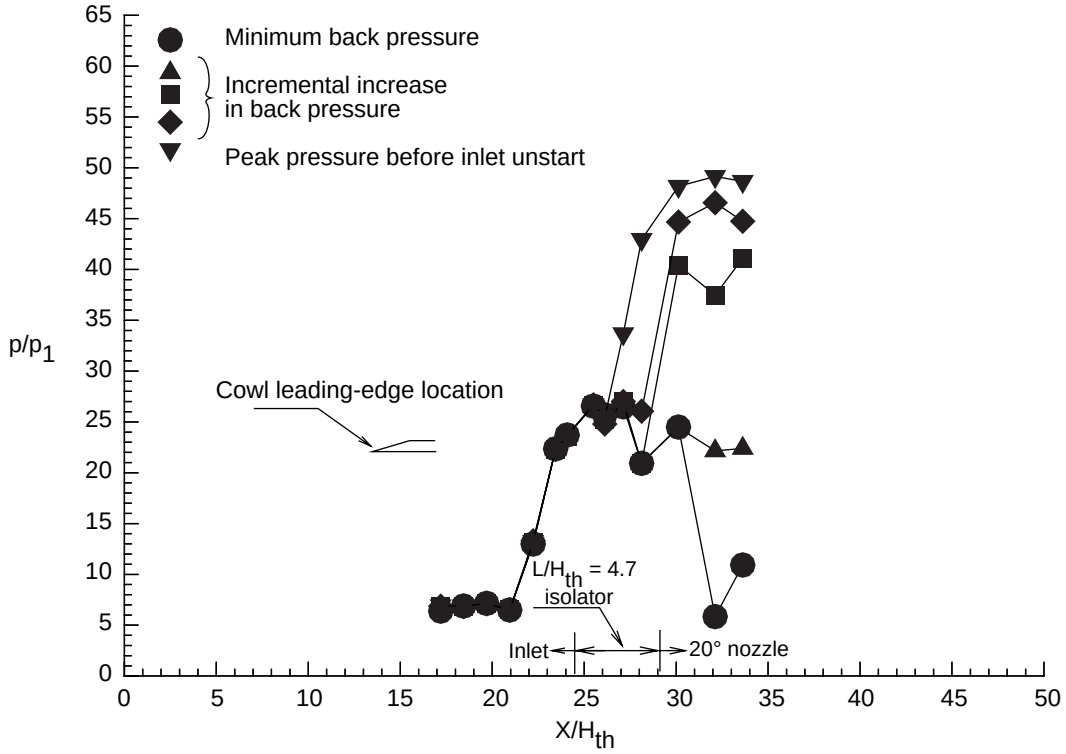

(d) Cowl side at β = 9.8° with L/H_{th} = 4.7. Run 107; M_{th} = 1.71; $p_{N.S.}/p_1$ = 80.20.

Figure 23. Continued.

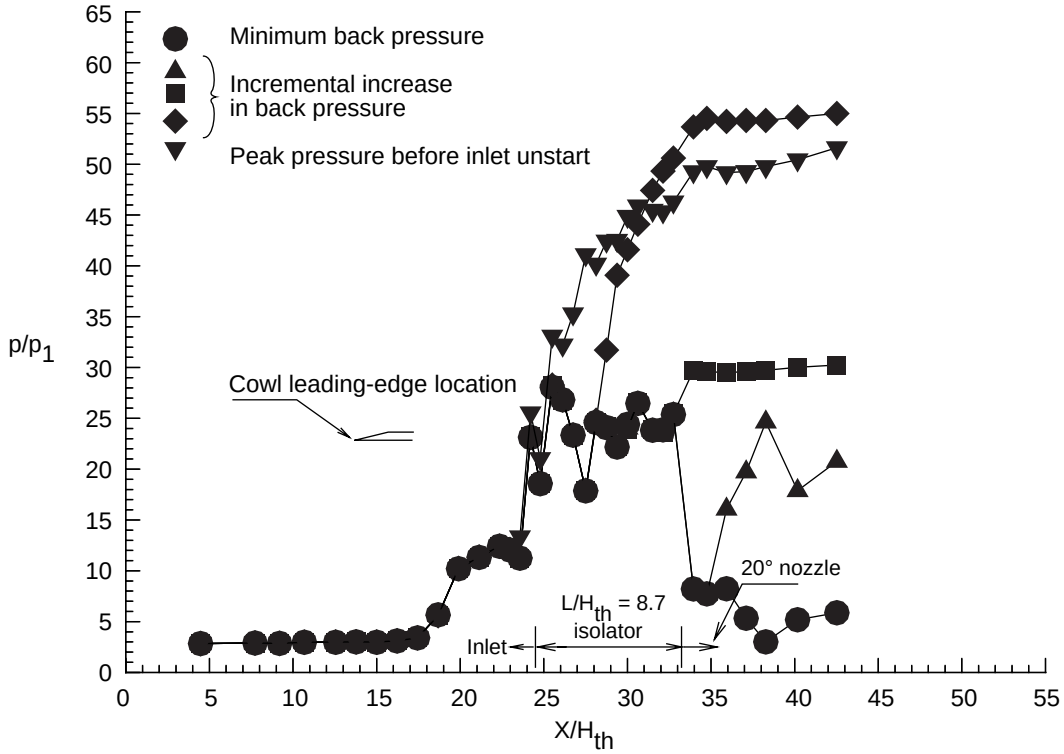

(e) Body side at β = 9.3° with L/H_{th} = 8.7. Run 10; M_{th} = 1.77; $p_{N.S.}/p_1$ = 79.50.

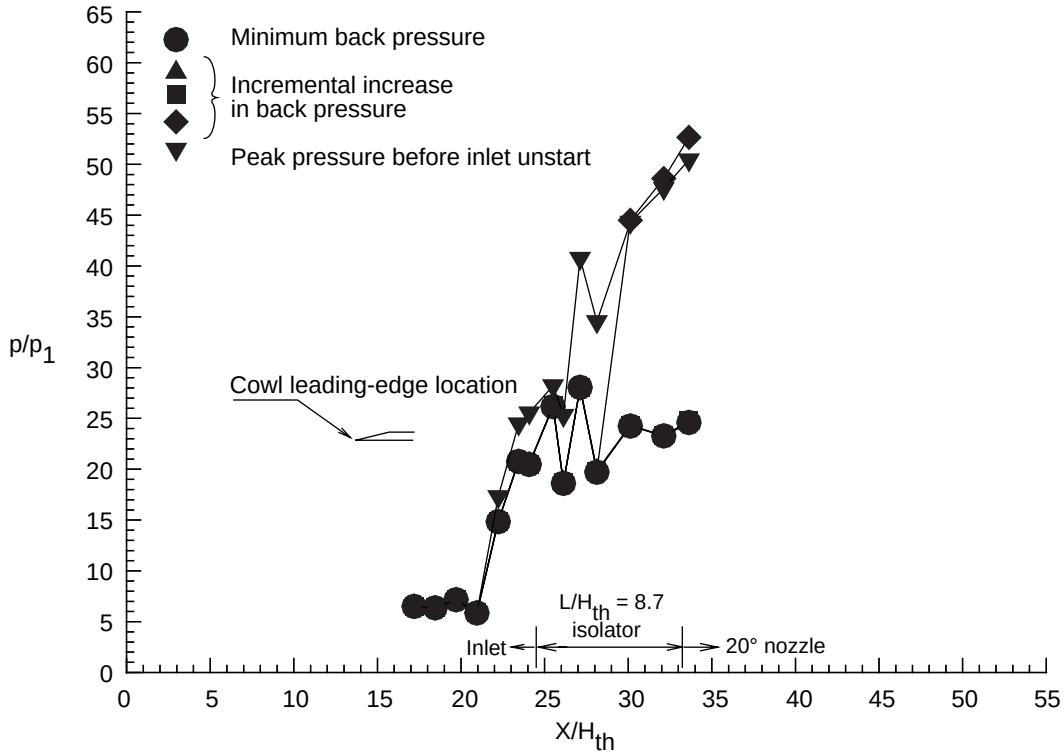

(f) Cowl side at β = 9.3° with L/H_{th} = 8.7. Run 10; M_{th} = 1.7; $p_{N.S.}/p_1$ = 79.50.

Figure 23. Continued.

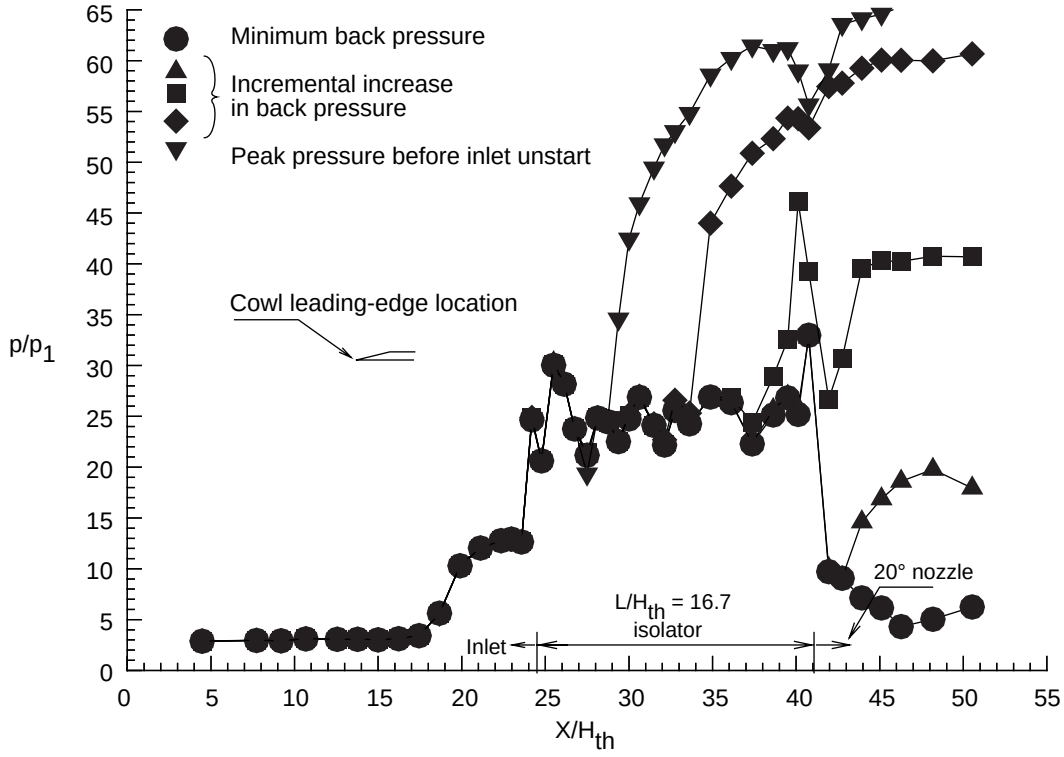

(g) Body side at β = 9.8° with L/H_{th} = 16.7. Run 137; M_{th} = 1.71; $p_{N.S.}/p_1$ = 80.20.

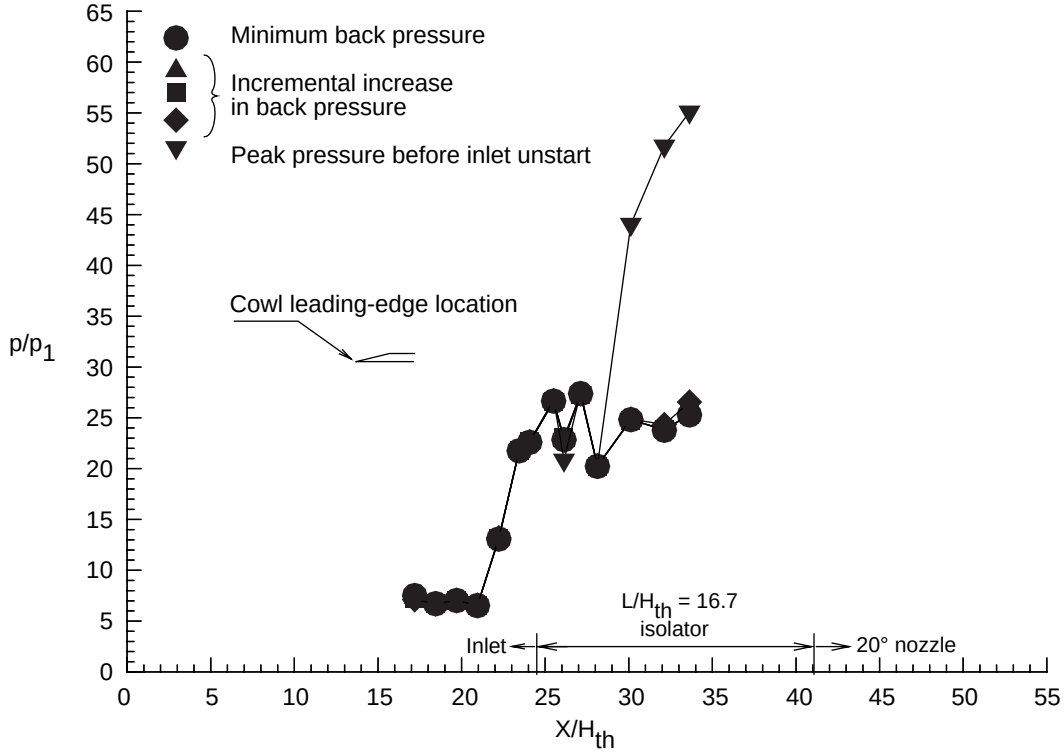

(h) Cowl side at β = 9.8° with L/H_{th} = 16.7. Run 137; M_{th} = 1.71; $p_{N.S.}/p_1$ = 80.20.

Figure 23. Continued.

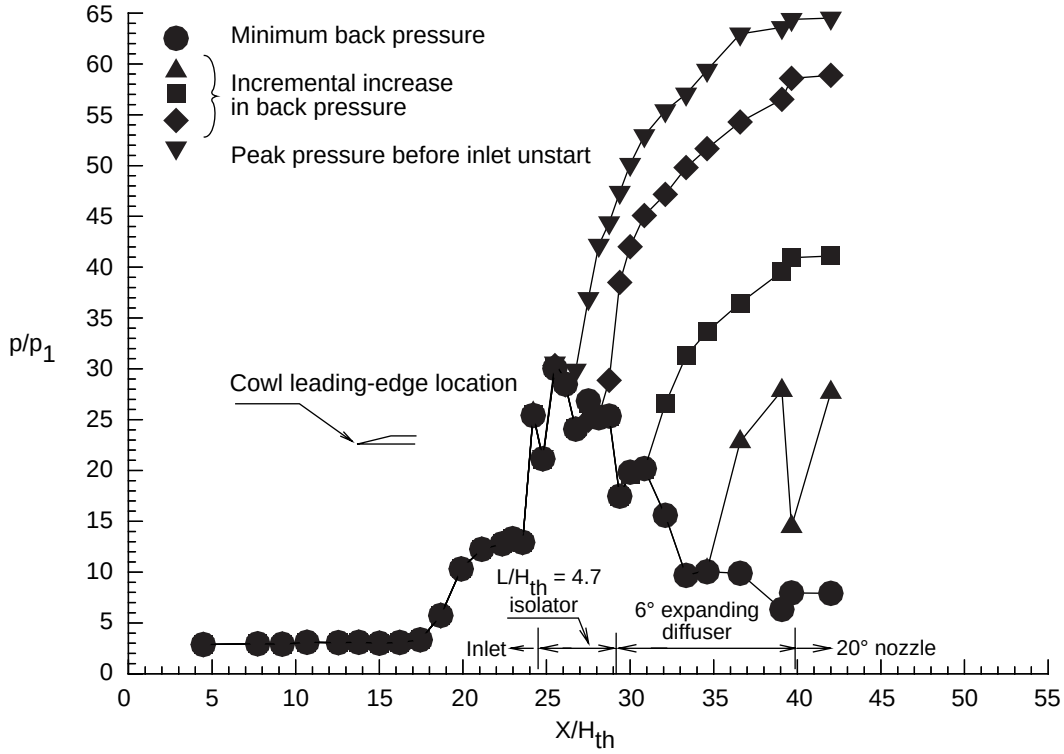

(i) Body side at β = 9.8° with L/H_{th} = 4.7 followed by angle of 6° divergence. Run 120; M_{th} = 1.71; $p_{N.S.}/p_1$ = 80.20.

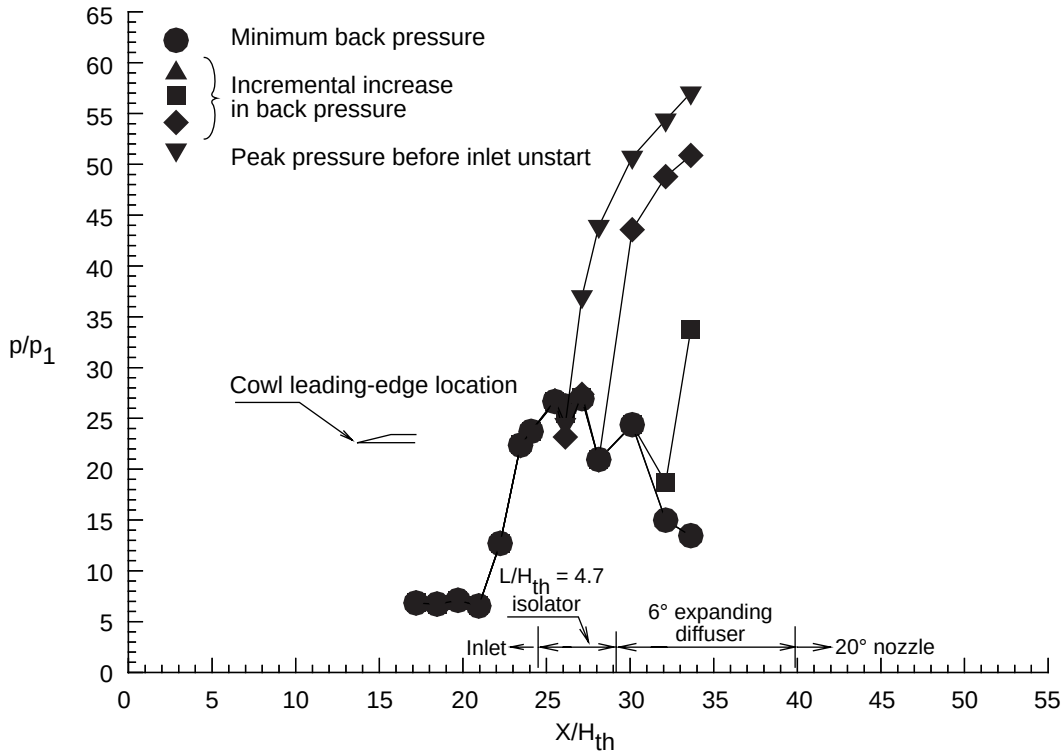

(j) Cowl side at β = 9.8° with L/H_{th} = 4.7 followed by angle of 6° divergence. Run 120; M_{th} = 1.71; $p_{N.S.}/p_1$ = 80.20.

Figure 23. Concluded.

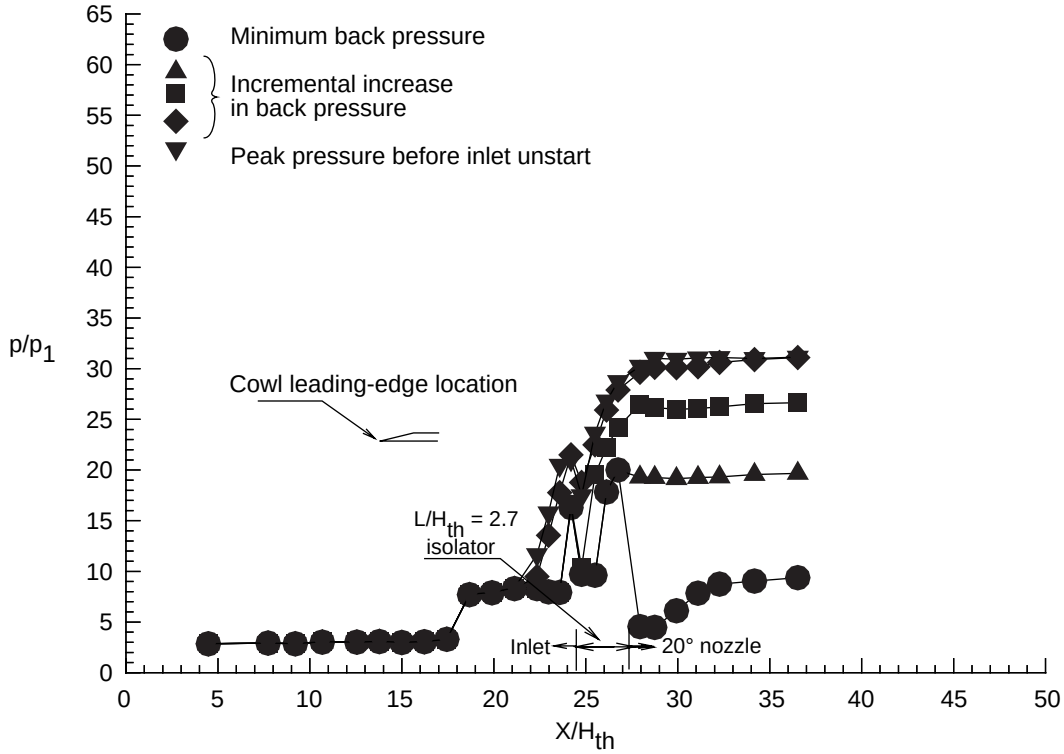

(a) Body side at β = 6.1° with L/H_{th} = 2.7. Run 47; M_{th} = 2.14; $p_{N.S.}/p_1$ = 72.36.

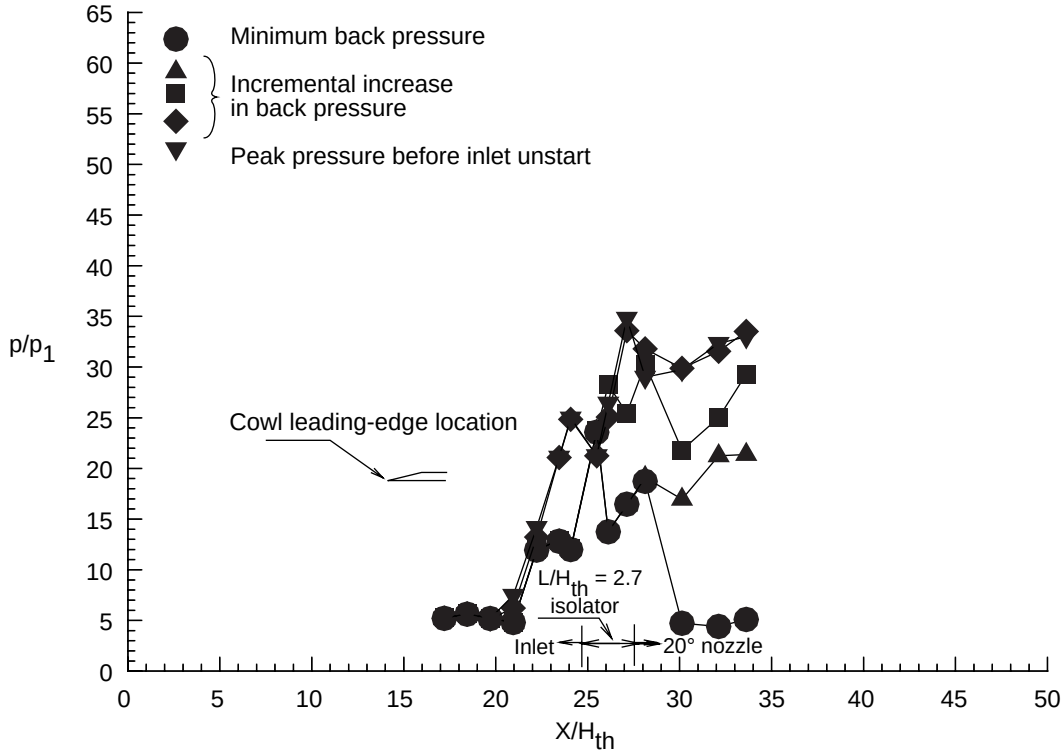

(b) Cowl side at β = 6.1° with L/H_{th} = 2.7. Run 47; M_{th} = 2.14; $p_{N.S.}/p_1$ = 72.36.

Figure 24. Back-pressure effects for 4.4-in. cowl (L_c/H_{th} = 11.00) with thin boundary layer and medium inlet convergence angle (β = 6.1°) for L/H_{th} = 2.7, 4.7, 8.7, and 16.7, and also for L/H_{th} = 4.7 followed by divergence angle of 6°. Constant-area isolator.

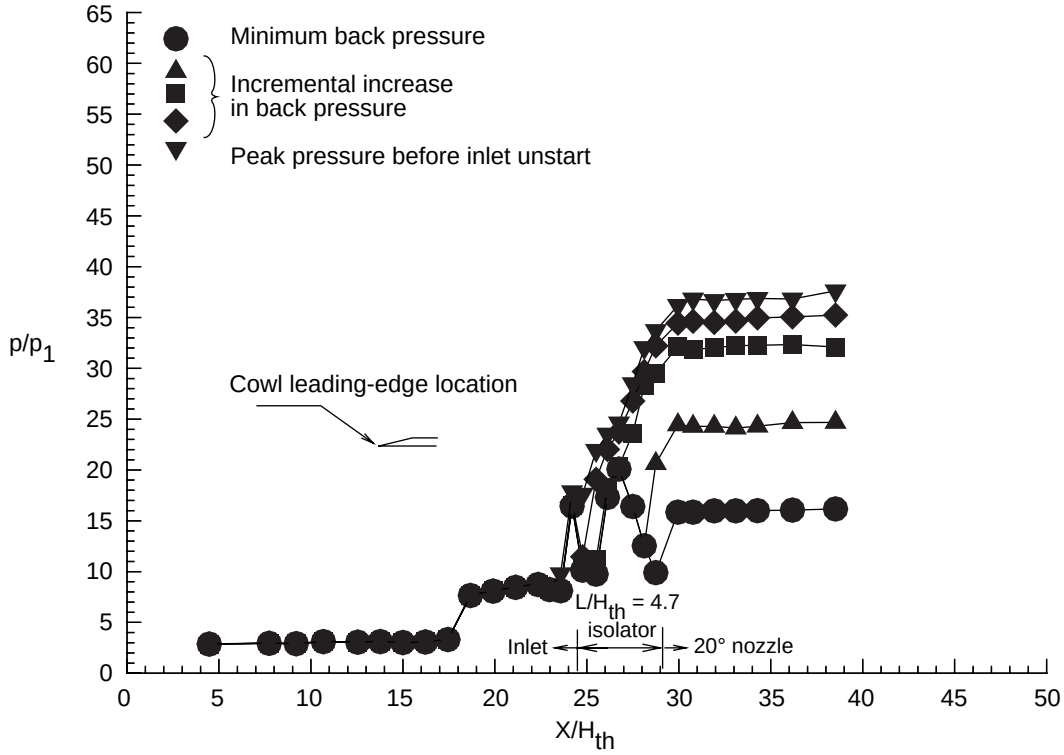

(c) Body side at β = 6.1° with L/H_{th} = 4.7. Run 108; M_{th} = 2.14; $p_{N.S.}/p_1$ = 72.36.

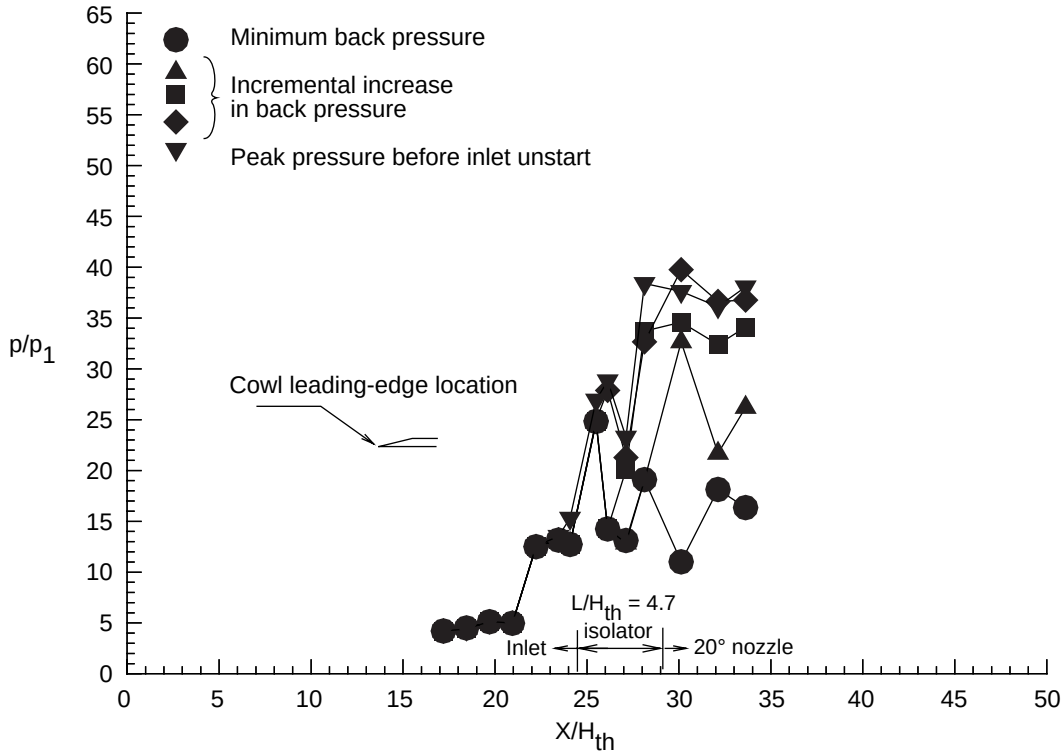

(d) Cowl side at β = 6.1° with L/H_{th} = 4.7. Run 108; M_{th} = 2.14; $p_{N.S.}/p_1$ = 72.36.

Figure 24. Continued.

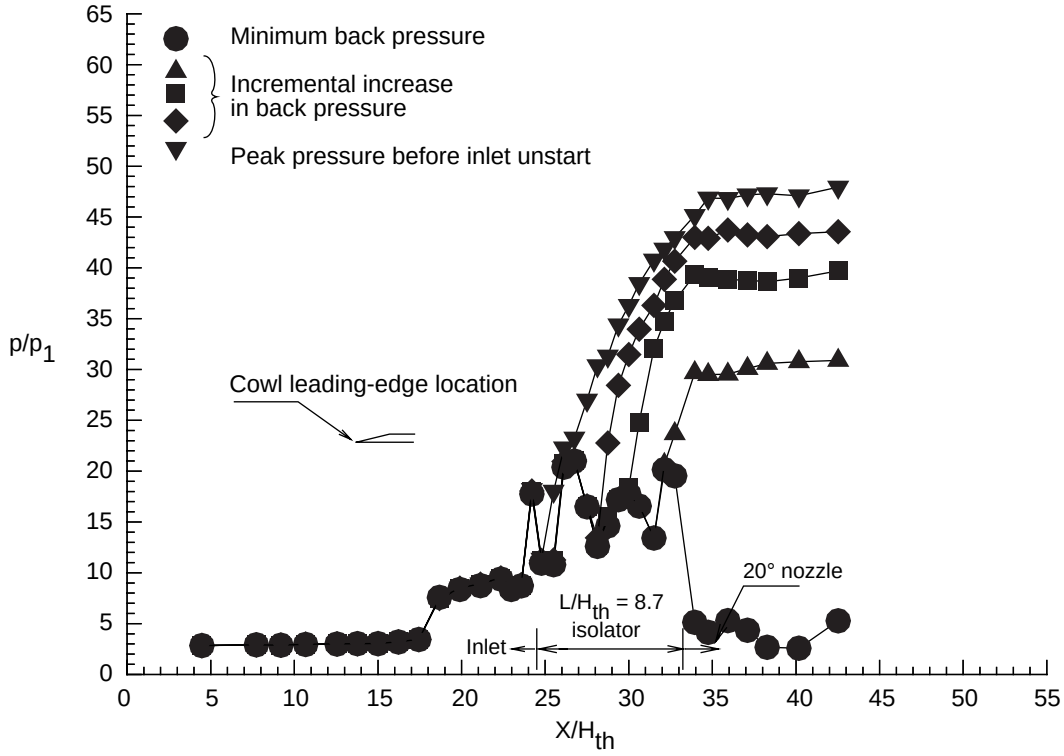

(e) Body side at β = 6.1° with L/H_{th} = 8.7. Run 11; M_{th} = 2.14; $p_{N.S.}/p_1$ = 72.36.

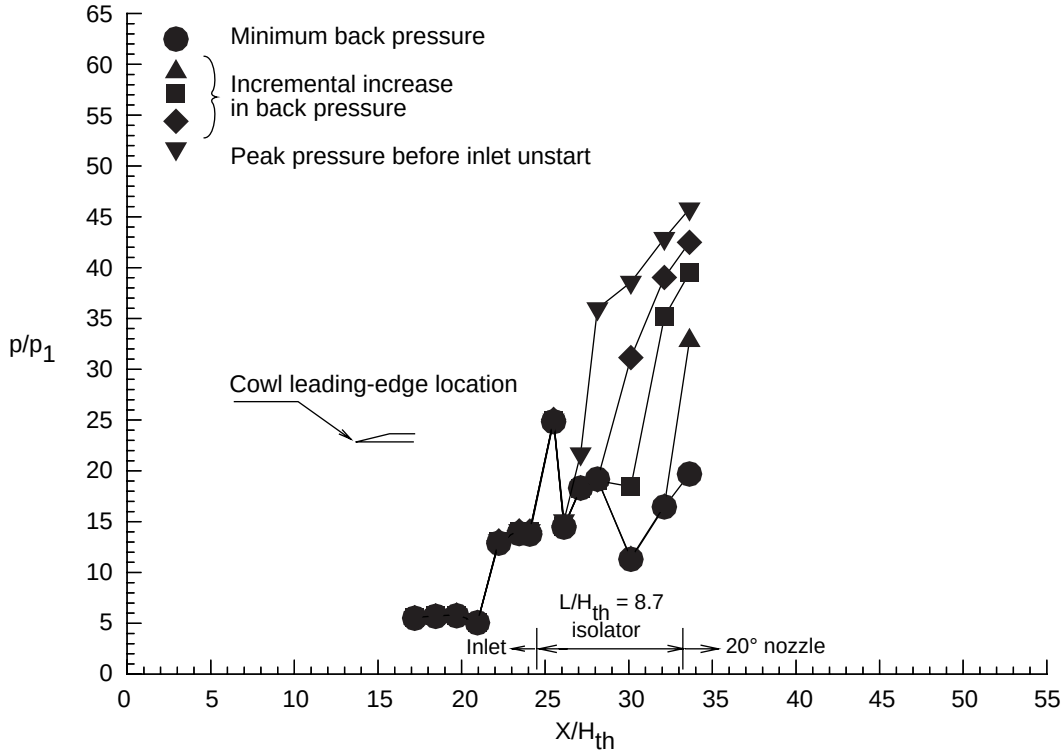

(f) Cowl side at β = 6.1° with L/H_{th} = 8.7. Run 11; M_{th} = 2.14; $p_{N.S.}/p_1$ = 72.36.

Figure 24. Continued.

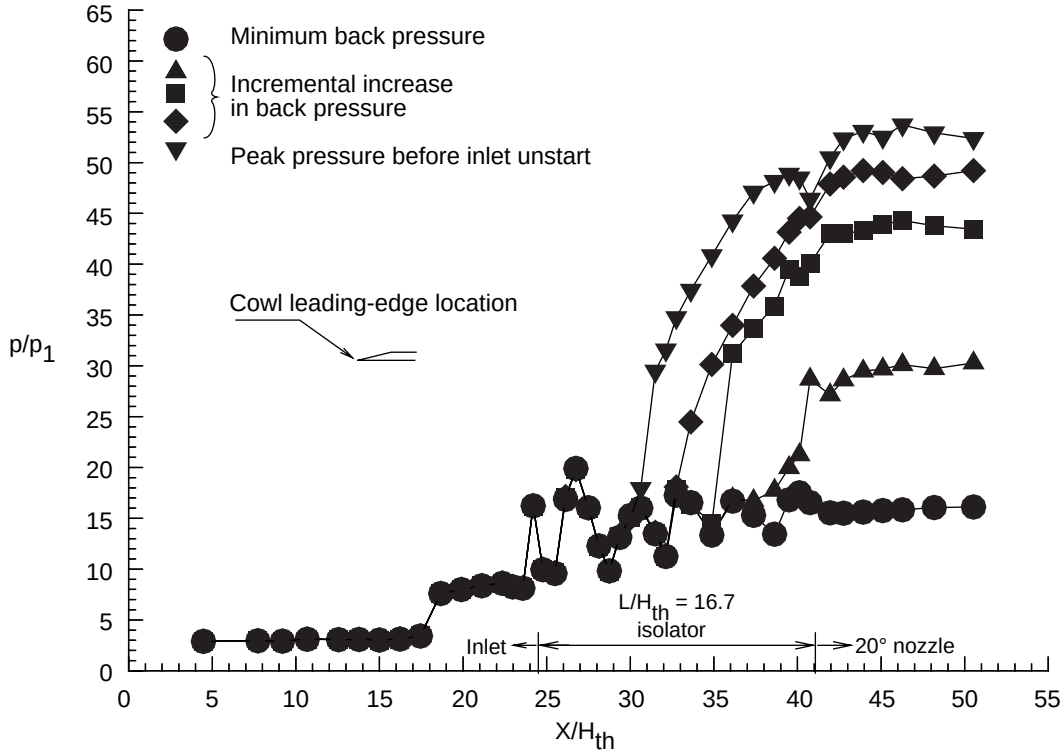

(g) Body side at β = 6.1° with L/H_{th} = 16.7. Run 136; M_{th} = 2.14; $p_{N.S.}/p_1$ = 72.36.

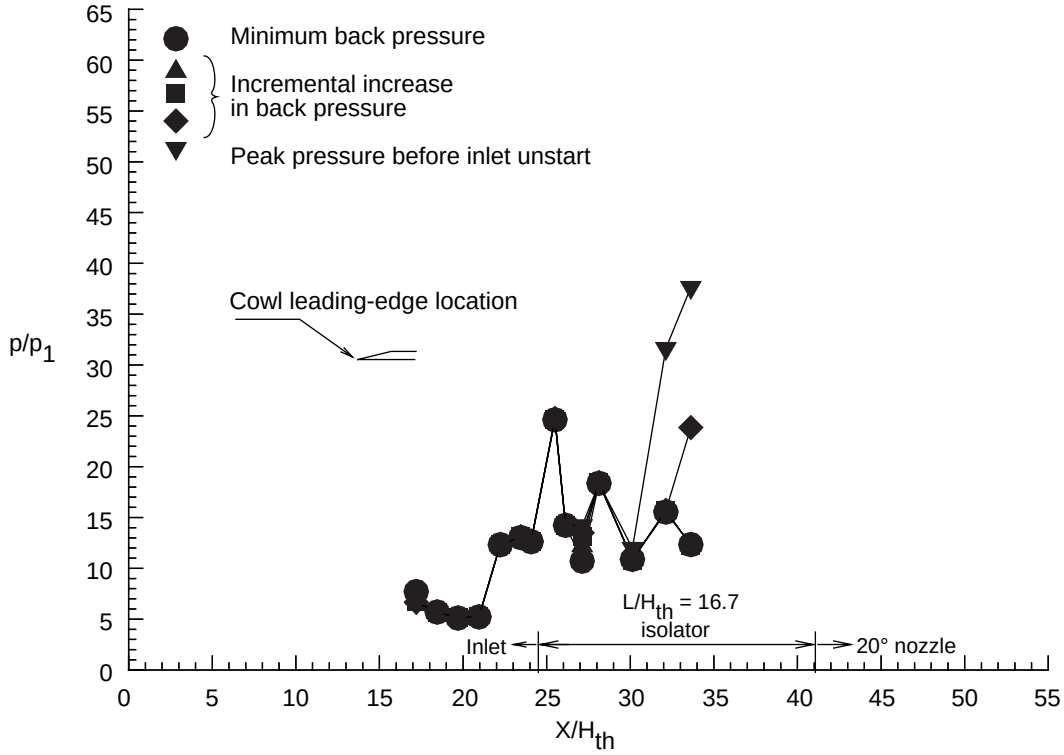

(h) Cowl side at β = 6.1° with L/H_{th} = 16.7. Run 136; M_{th} = 2.14; $p_{N.S.}/p_1$ = 72.36.

Figure 24. Continued.

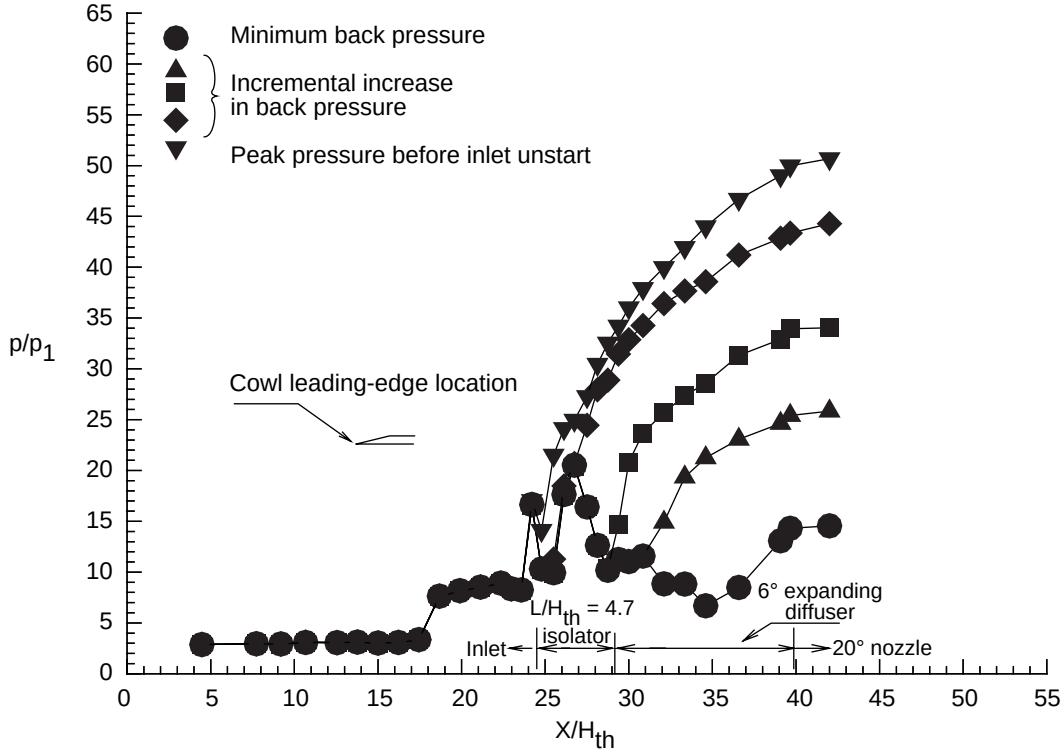

(i) Body side at β = 6.1° with L/H_{th} = 4.7 followed by angle of 6° divergence. Run 120; M_{th} = 2.14; $p_{N.S.}/p_1$ = 72.36.

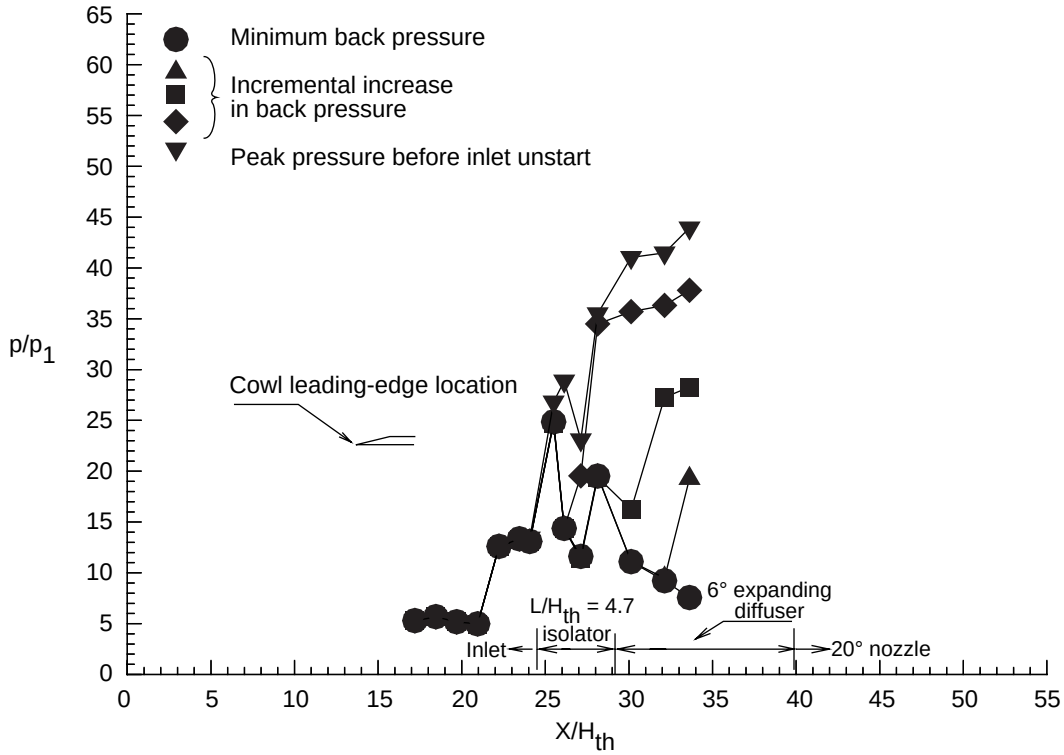

(j) Cowl side at β = 6.1° with L/H_{th} = 4.7 followed by angle of 6° divergence. Run 120; M_{th} = 2.14; $p_{N.S.}/p_1$ = 72.36.

Figure 24. Concluded.

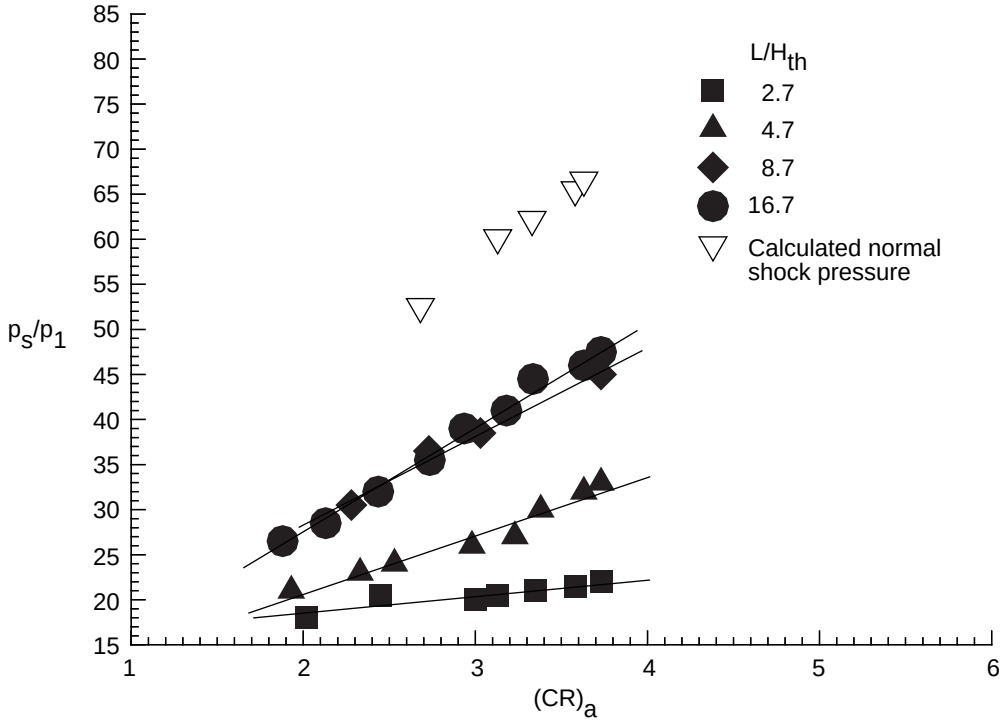

(a) Thin boundary layer.

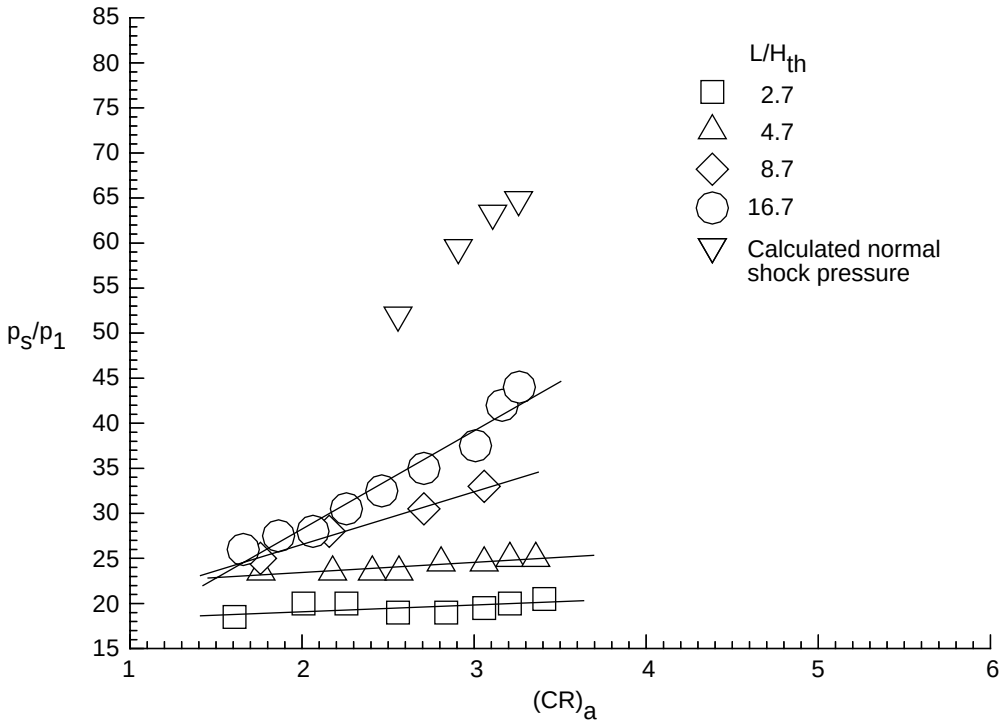

(b) Thick boundary layer.

Figure 25. Inlet-isolator maximum back pressure with constant-area isolator lengths (L/H_{th}) of 2.7, 4.7, 8.7, and 16.7 for 2.5-in. cowl (L_c/H_{th} = 6.25). Linear curve fit through data.

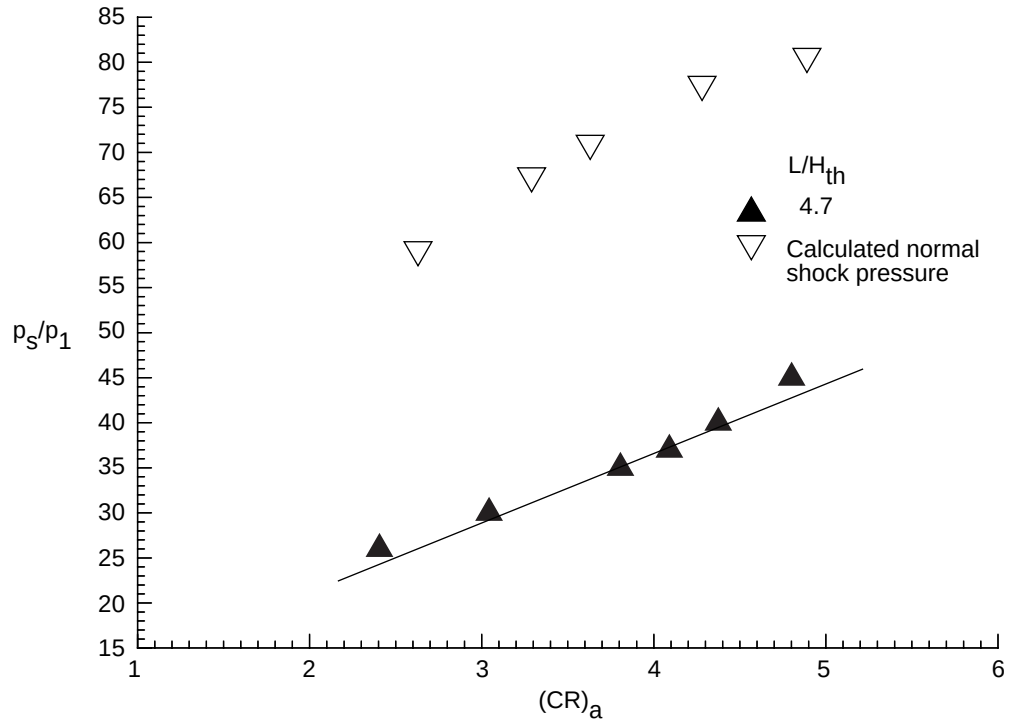

(a) Thin boundary layer.

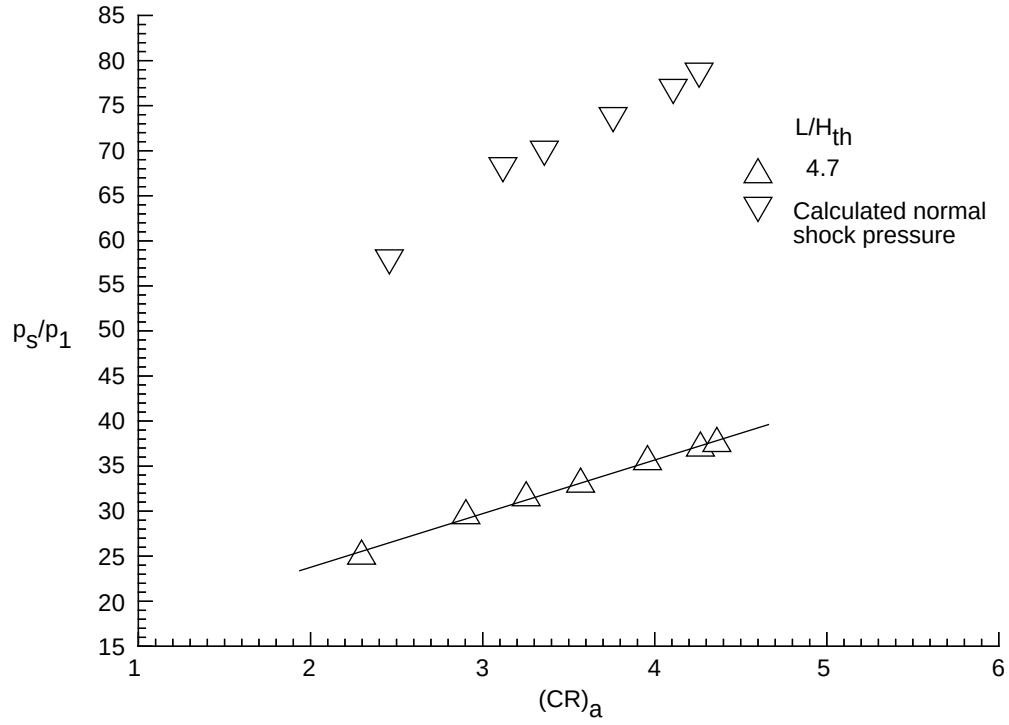

(b) Thick boundary layer.

Figure 26. Inlet-isolator maximum back pressure with constant-area isolator lengths (L/H_{th}) of 2.7, 4.7, 8.7, and 16.7 for 3.9-in. cowl (L_c/H_{th} = 9.75). Linear curve fit through data.

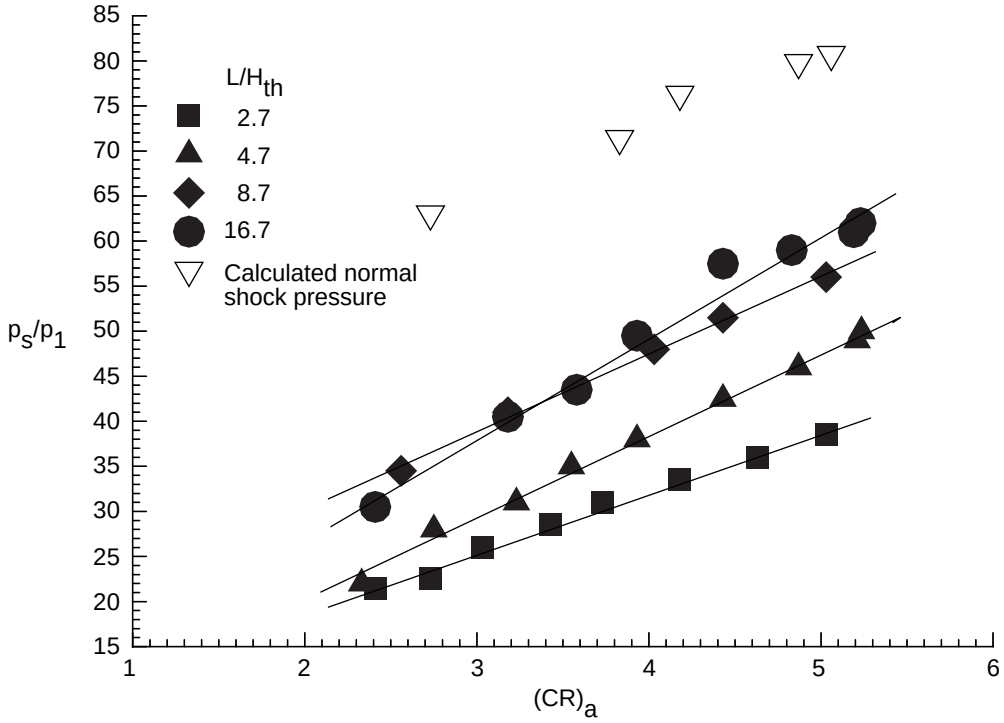

(a) Thin boundary layer.

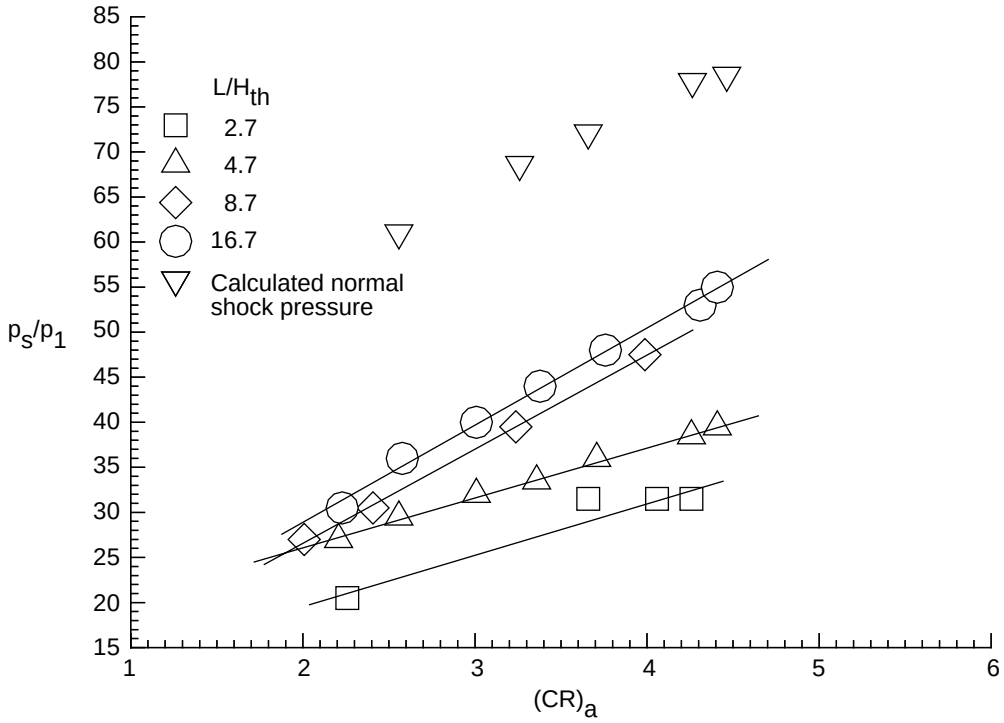

(b) Thick boundary layer.

Figure 27. Inlet-isolator maximum back pressure with constant-area isolator lengths (L/H_{th}) of 2.7, 4.7, 8.7, and 16.7 for 4.4-in. cowl (L_c/H_{th} = 11.00). Linear curve fit through data.

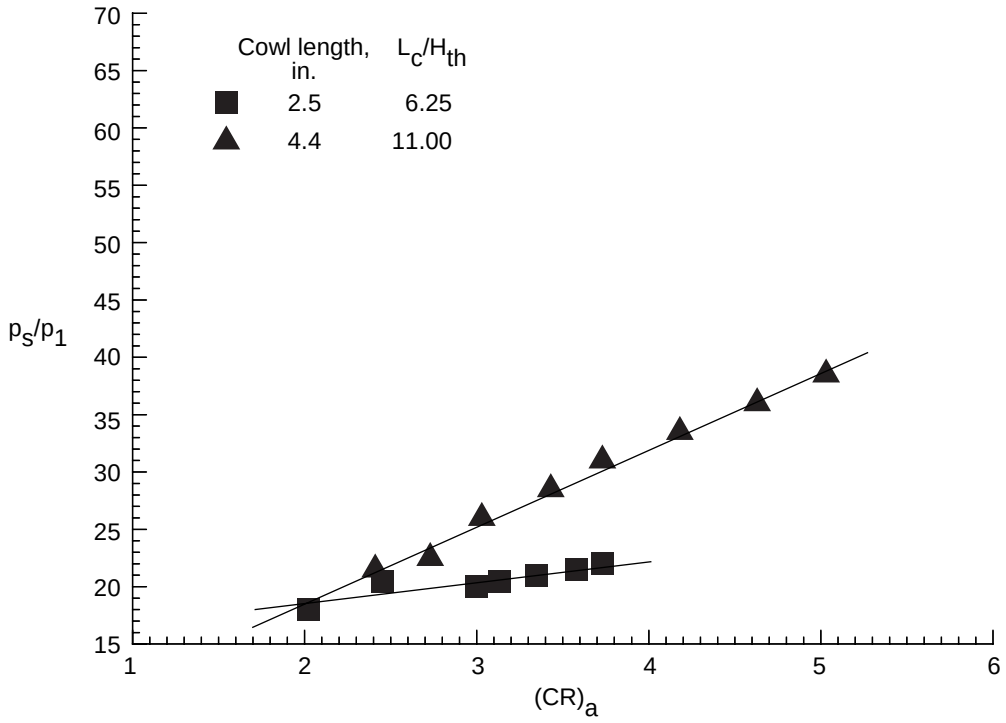

(a) Thin boundary layer.

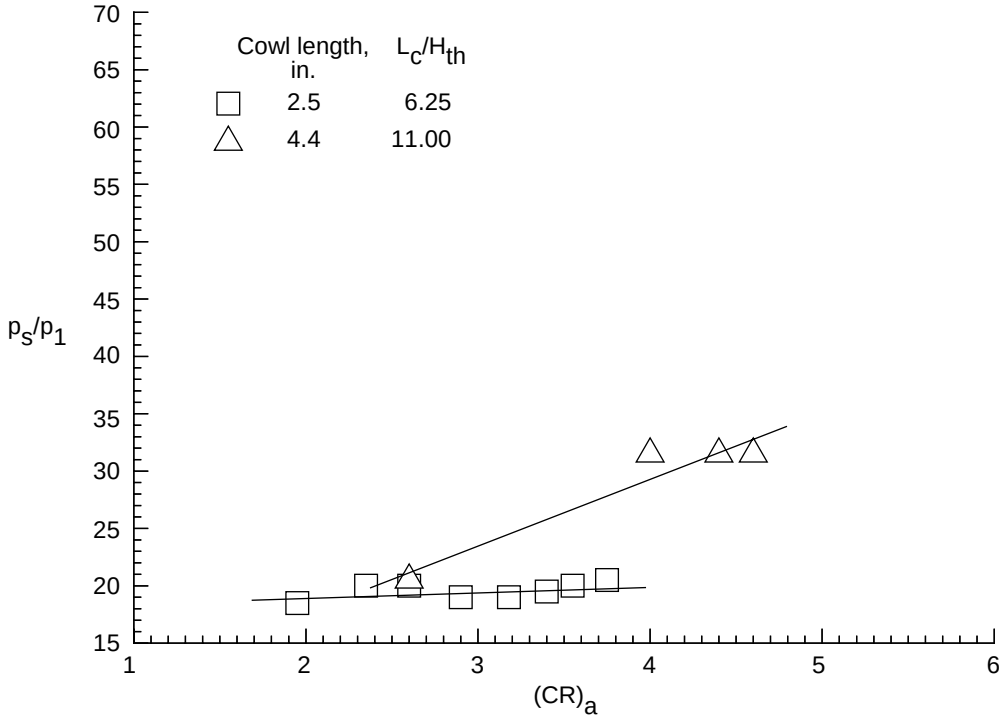

(b) Thick boundary layer.

Figure 28. Effects of 2.5- and 4.4-in. cowls on inlet-isolator maximum pressure capability with constant-area isolator length (L/H_{th}) of 2.7. Linear curve fit through data.

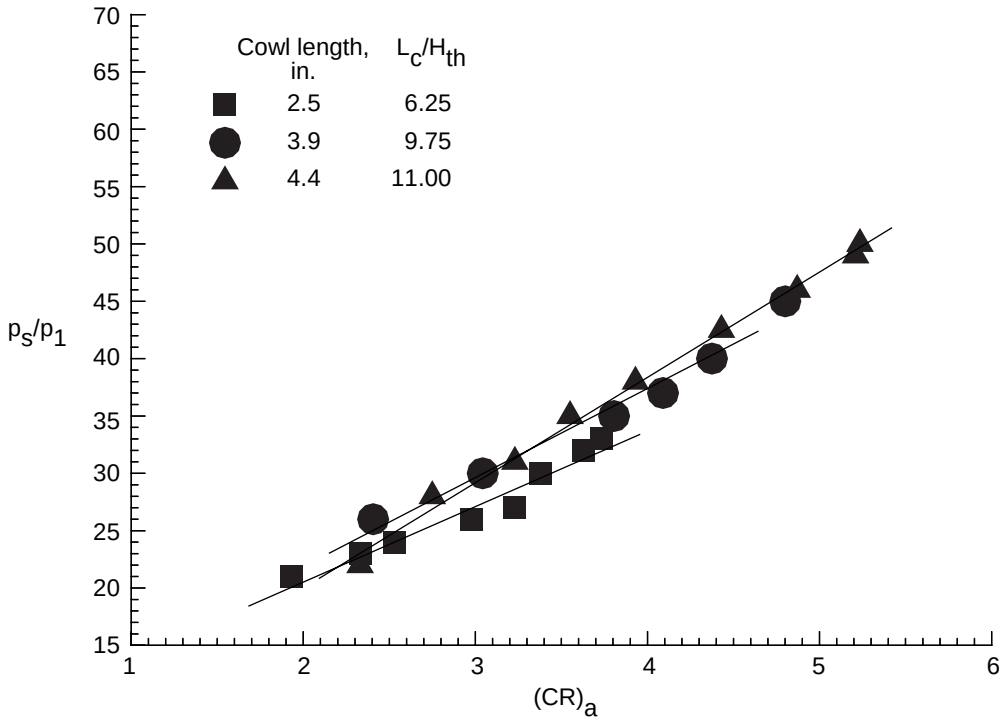

(a) Thin boundary layer.

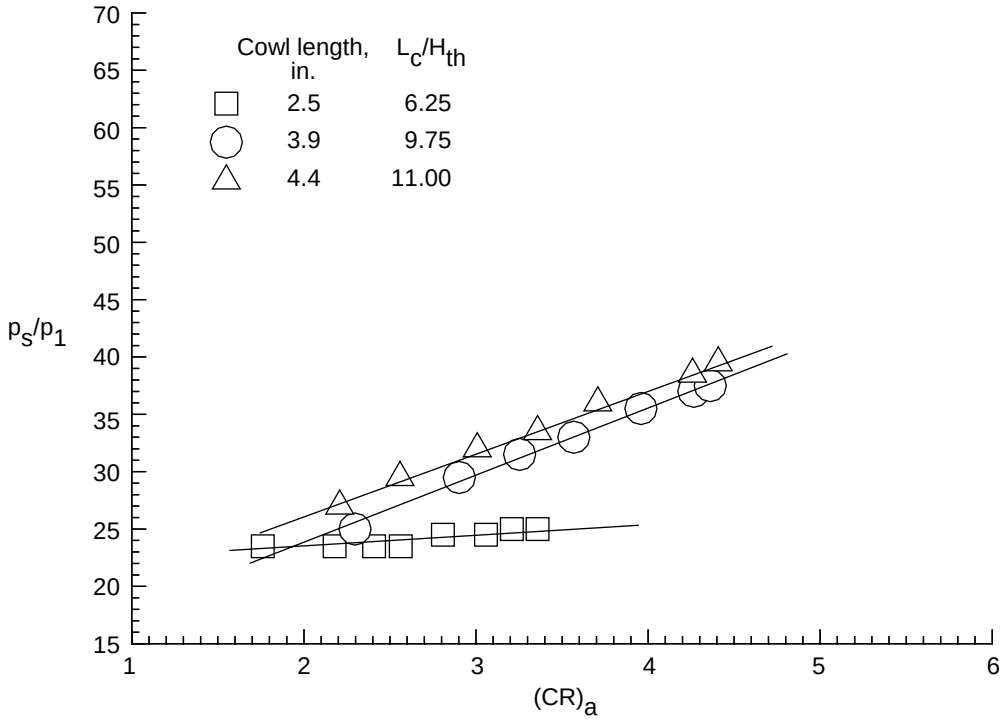

(b) Thick boundary layer.

Figure 29. Effects of 2.5-, 3.9-, and 4.4-in. cowls on inlet-isolator maximum pressure capability with constant-area isolator length (L/H_{th}) of 4.7 and with step area increase. Linear curve fit through data.

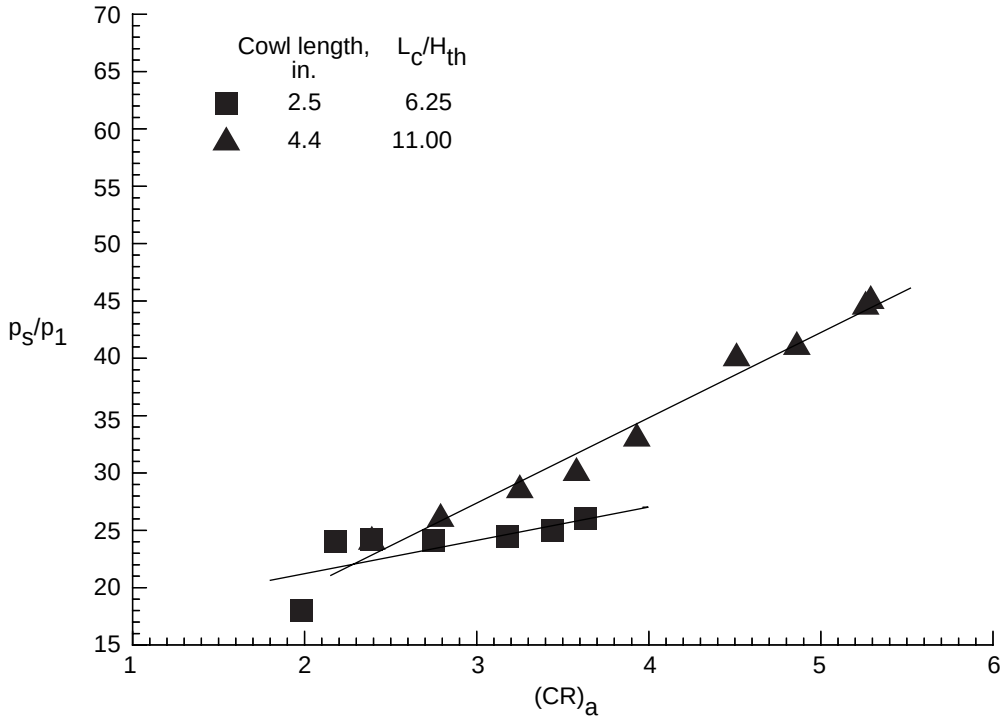

(c) Thin boundary layer and rearward-facing steps (L_s/H_{th} = 0.7). Step heights are 0.050 in. on body side and 0.028 in. on cowl side.

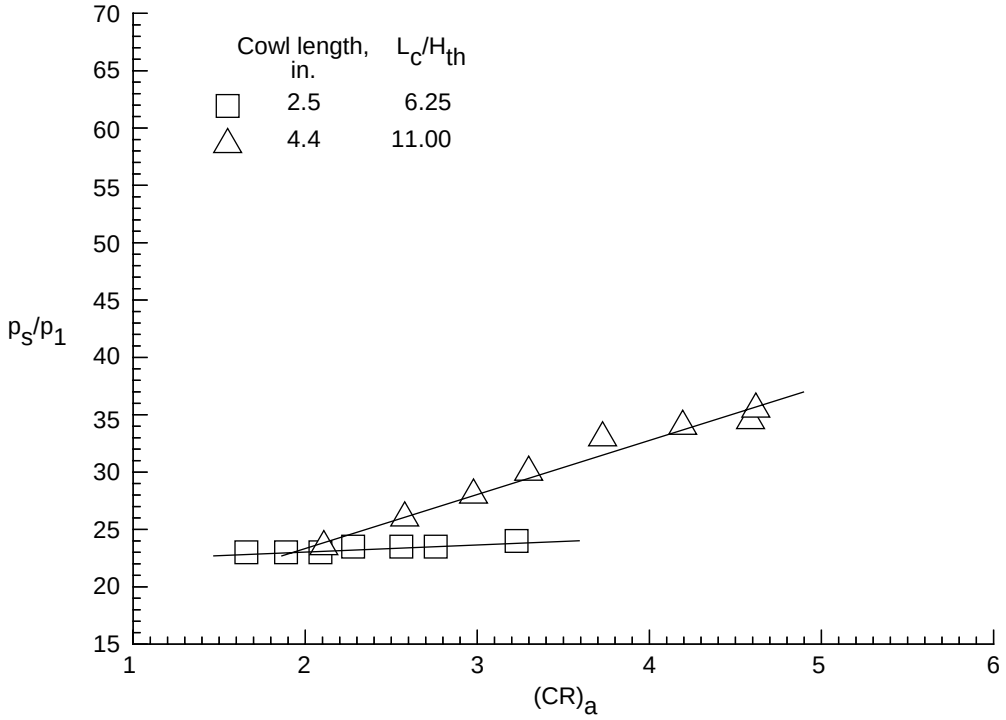

(d) Thick boundary layer and rearward-facing steps (L_s/H_{th} = 0.7). Step heights are 0.050 in. on body side and 0.028 in. on cowl side.

Figure 29. Continued.

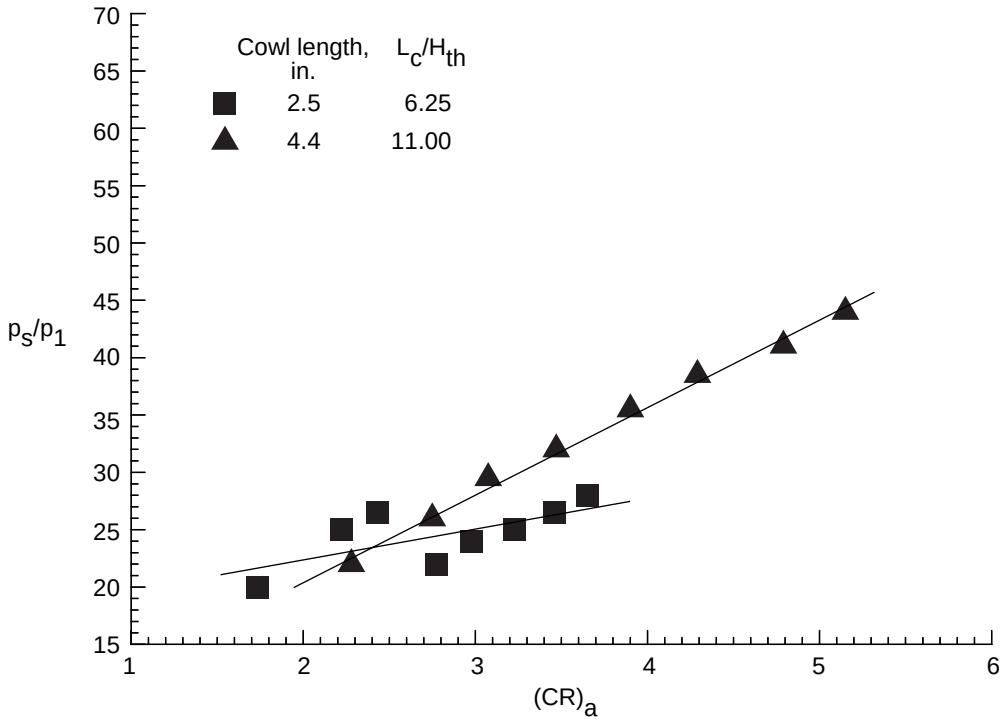

(e) Thin boundary layer and rearward-facing steps (L_s/H_{th} = 2.7). Step heights are 0.050 in. on body side and 0.028 in. on cowl side.

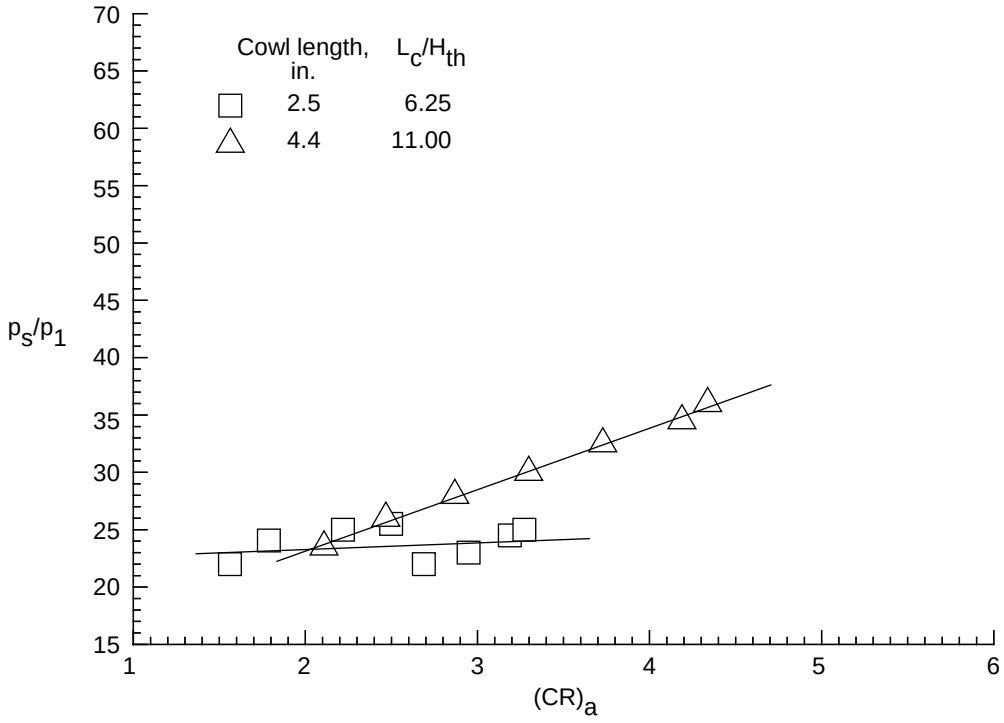

(f) Thick boundary layer and rearward-facing steps (L_s/H_{th} = 2.7). Step heights are 0.050 in. on body side and 0.028 in. on cowl side.

Figure 29. Concluded.

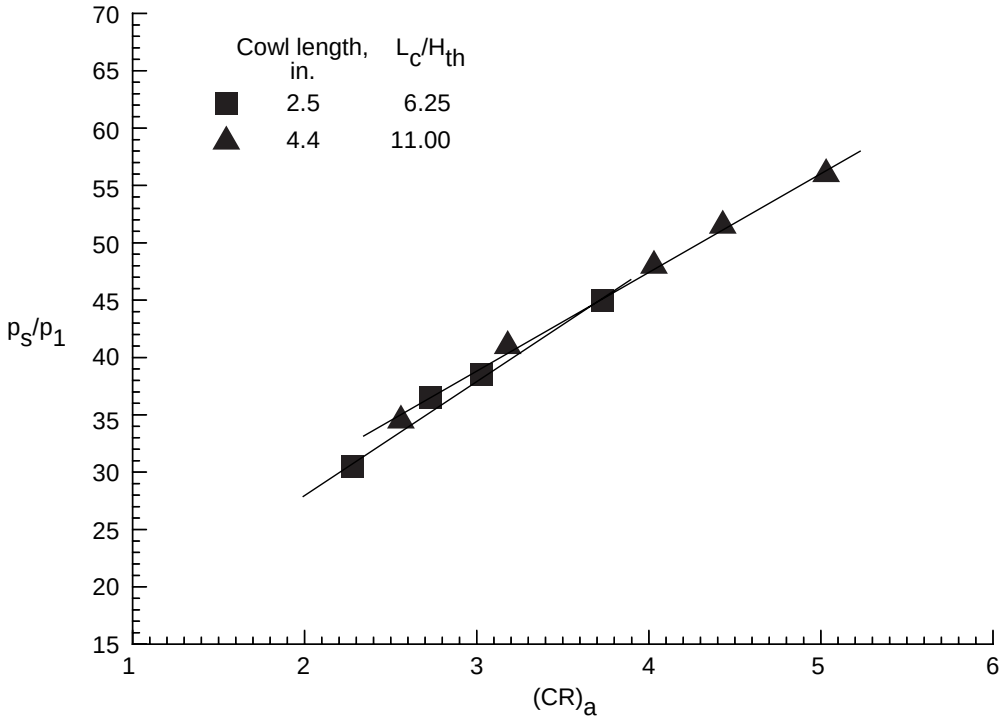

(a) Thin boundary layer.

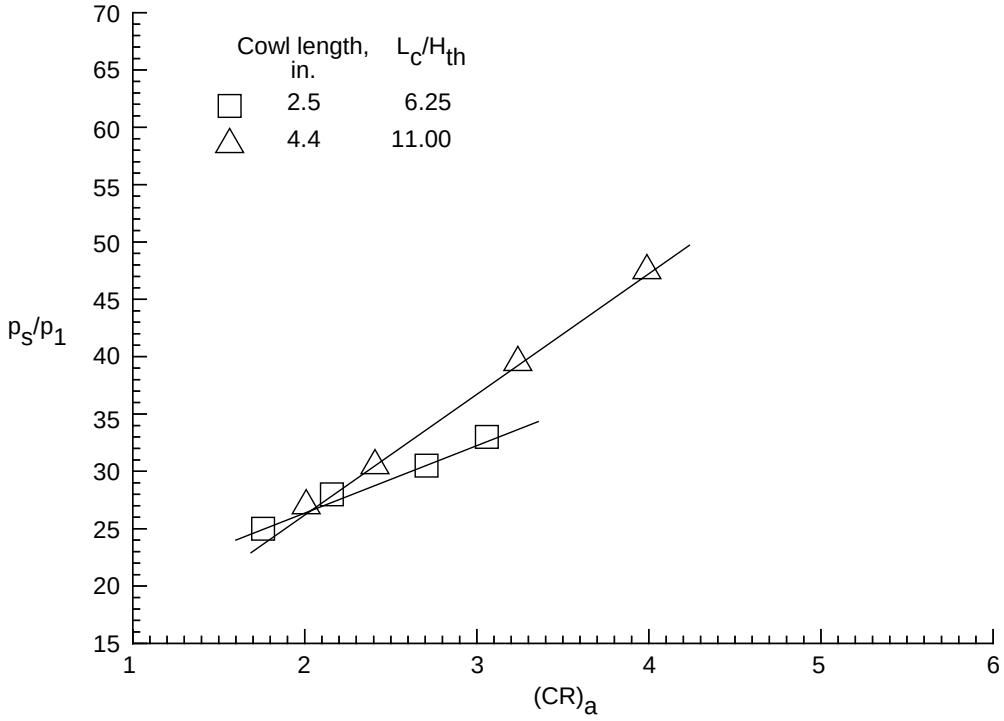

(b) Thick boundary layer.

Figure 30. Effects of 2.5- and 4.4-in. cowls on inlet-isolator maximum pressure capability with constant-area isolator length (L/H_{th}) of 8.7. Linear curve fit through data.

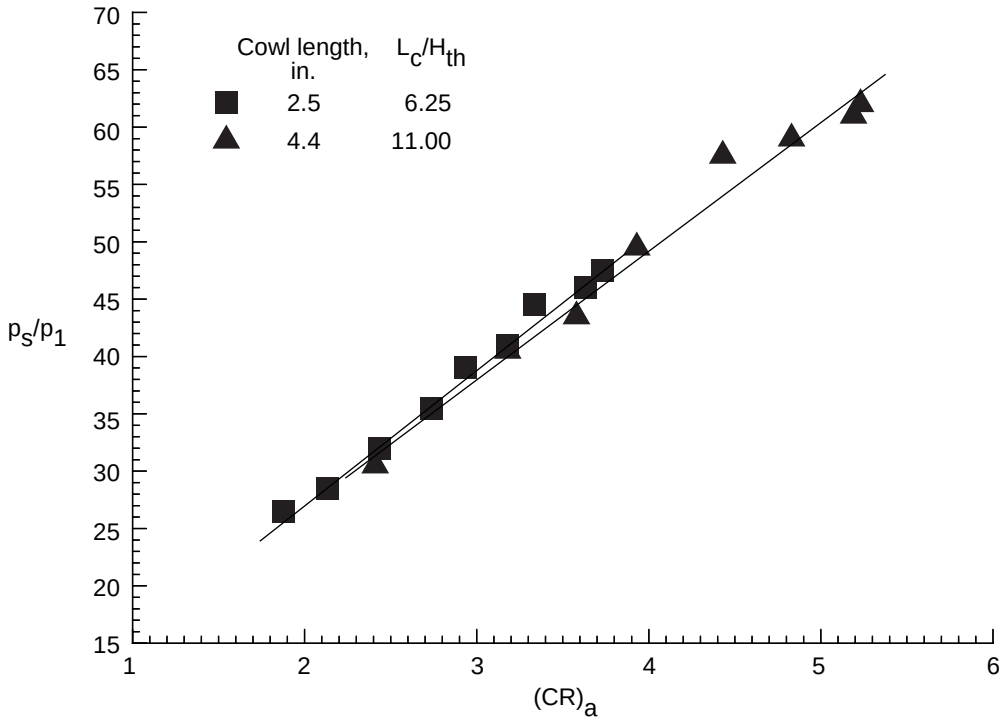

(a) Thin boundary layer.

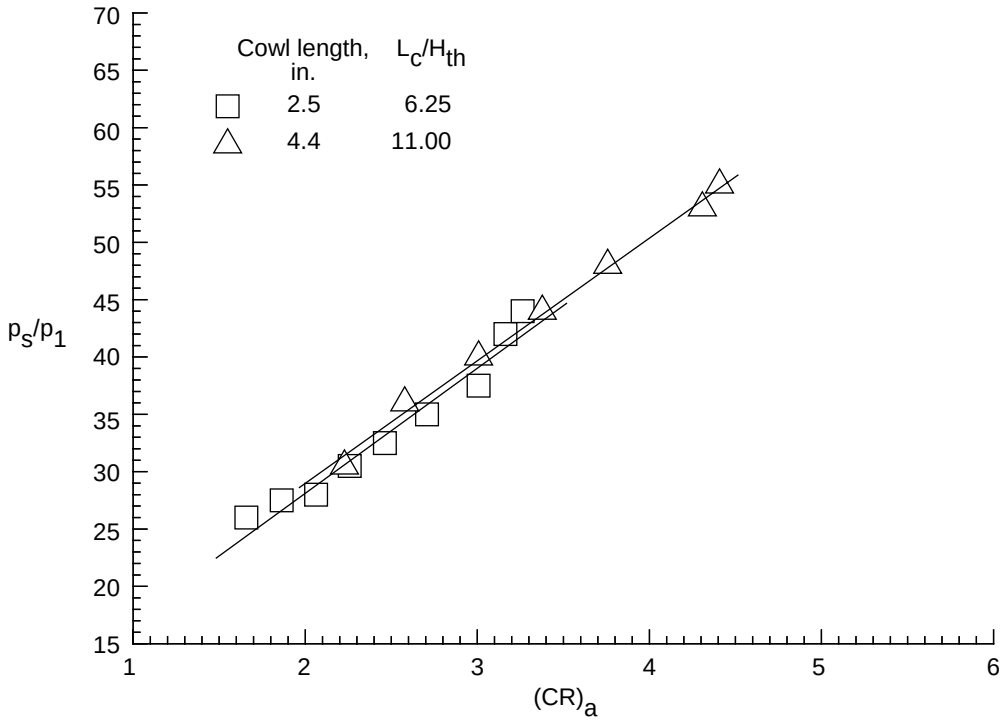

(b) Thick boundary layer.

Figure 31. Effects of 2.5- and 4.4-in. cowls on inlet-isolator maximum pressure capability with constant-area isolator length (L/H_{th}) of 16.7. Linear curve fit through data.

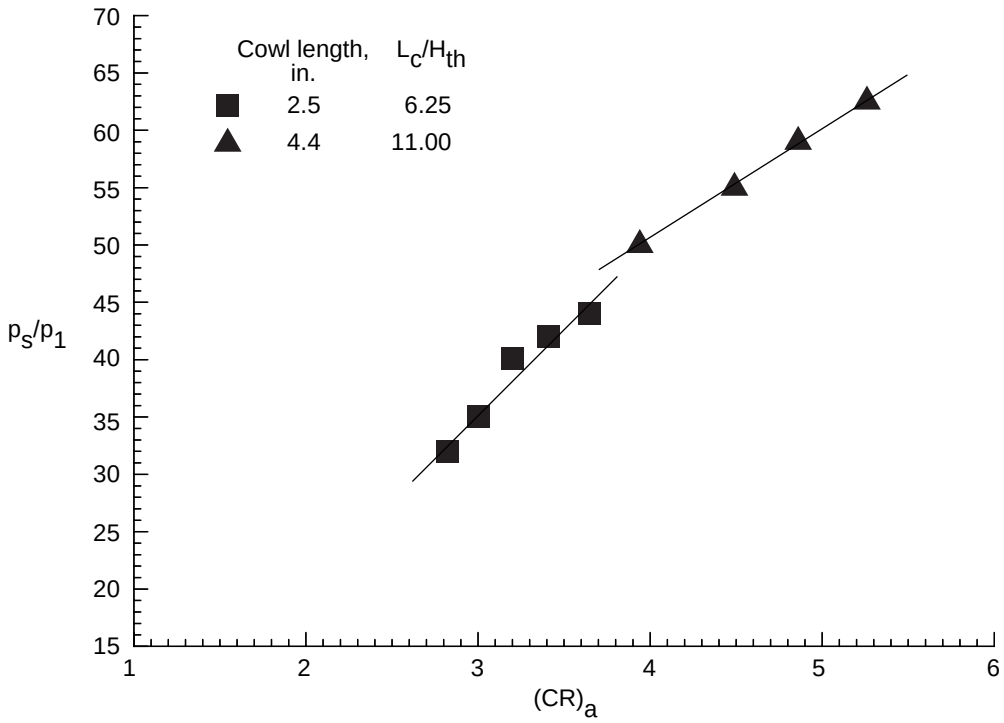

(a) Thin boundary layer.

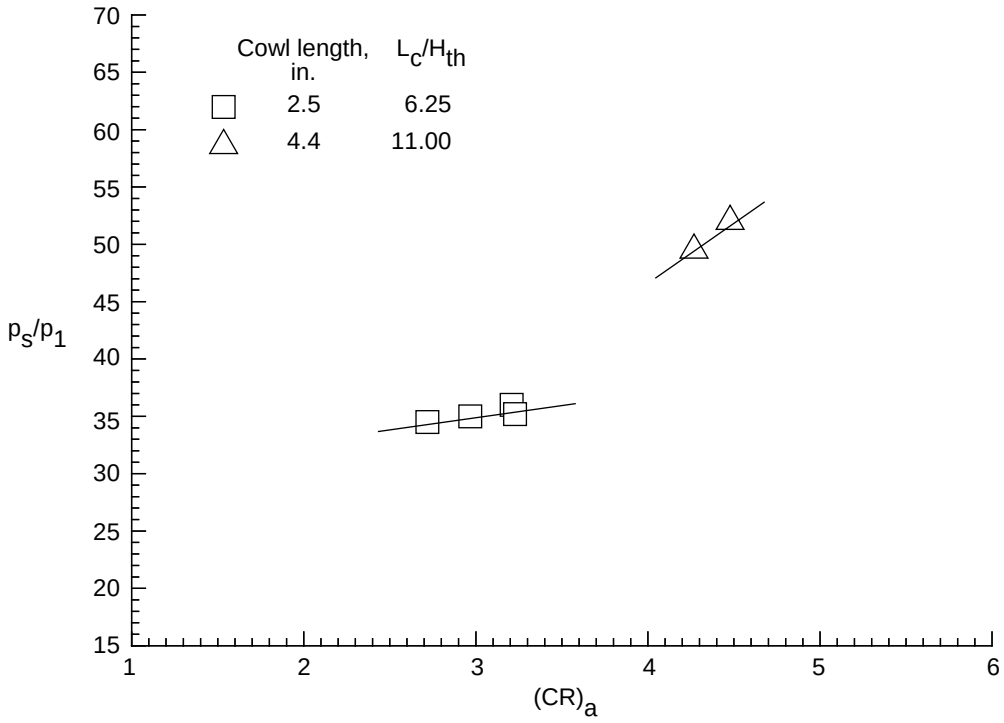

(b) Thick boundary layer.

Figure 32. Effects of 2.5- and 4.4-in. cowls on inlet-isolator maximum pressure capability with constant-area isolator length (L/H_{th}) of 4.7 followed by divergence angle of 6° with L/H_{th} = 15.32. Linear curve fit through data.

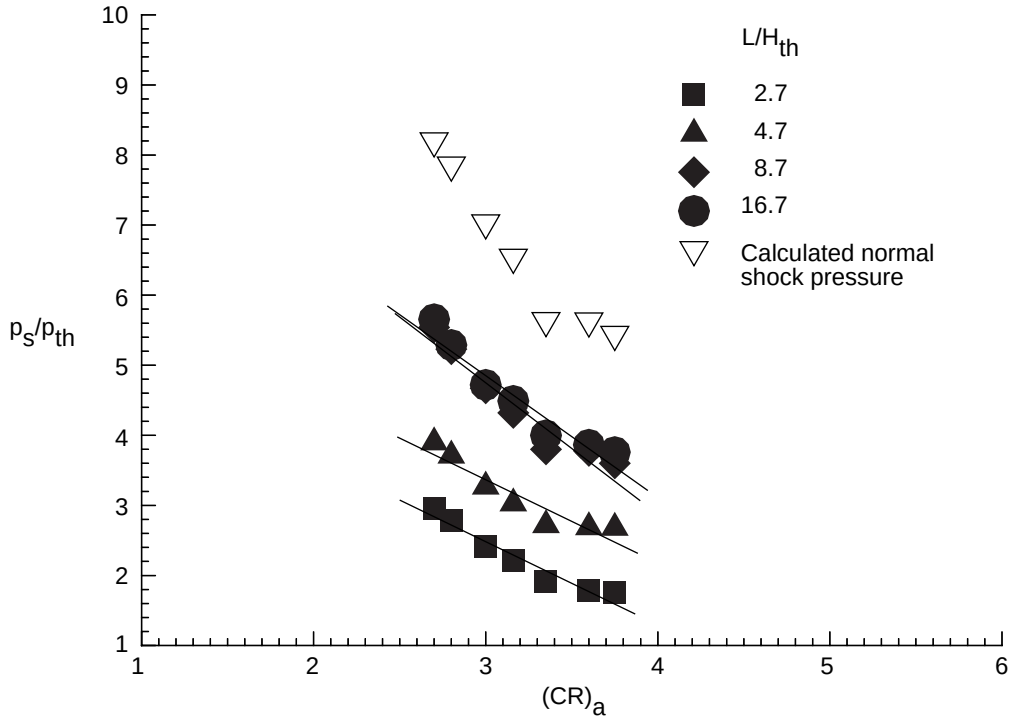

(a) Thin boundary layer.

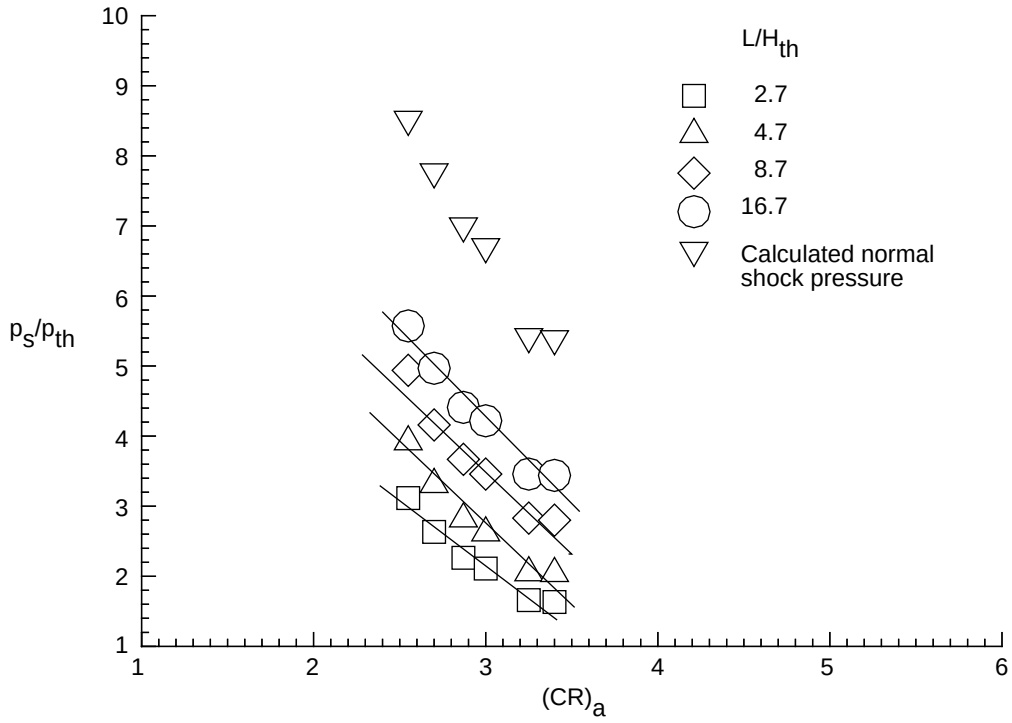

(b) Thick boundary layer.

Figure 33. Isolator effectiveness for 2.5-in. cowl (L_c/H_{th} = 6.25). Linear curve fit through data.

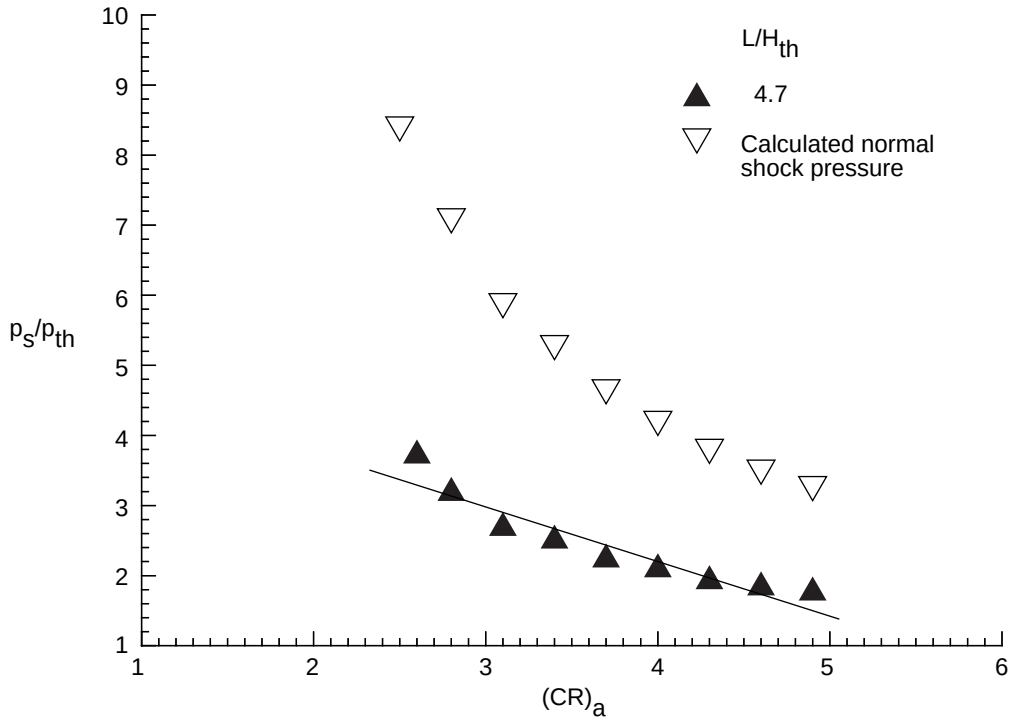

(a) Thin boundary layer.

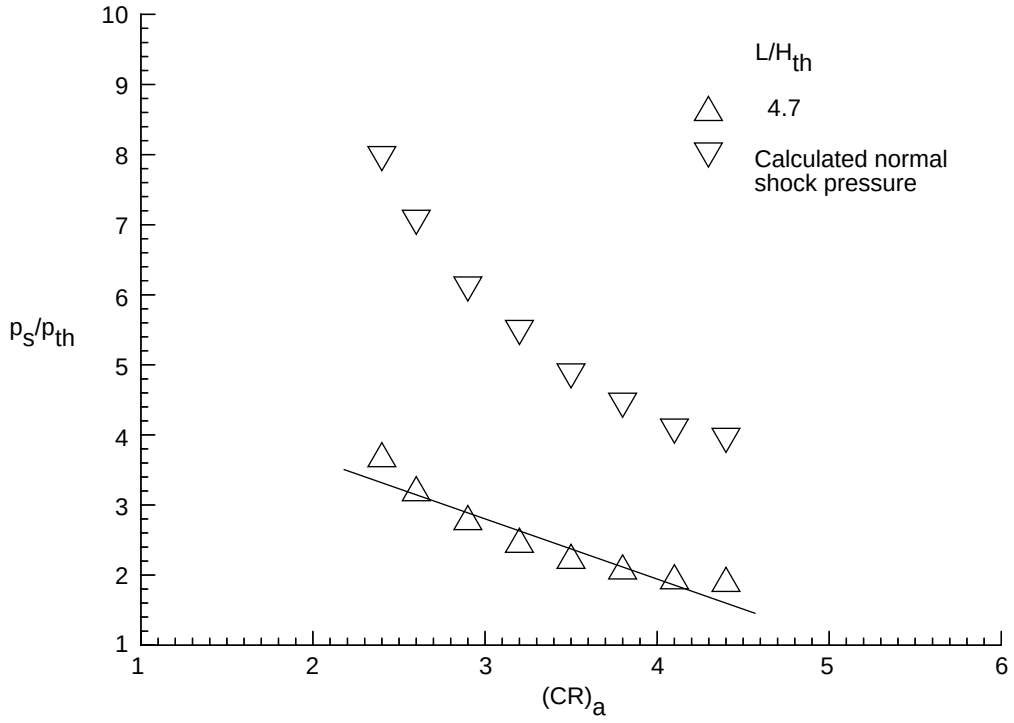

(b) Thick boundary layer.

Figure 34. Isolator effectiveness for 3.9-in. cowl (L_c/H_{th} = 9.75). Linear curve fit through data.

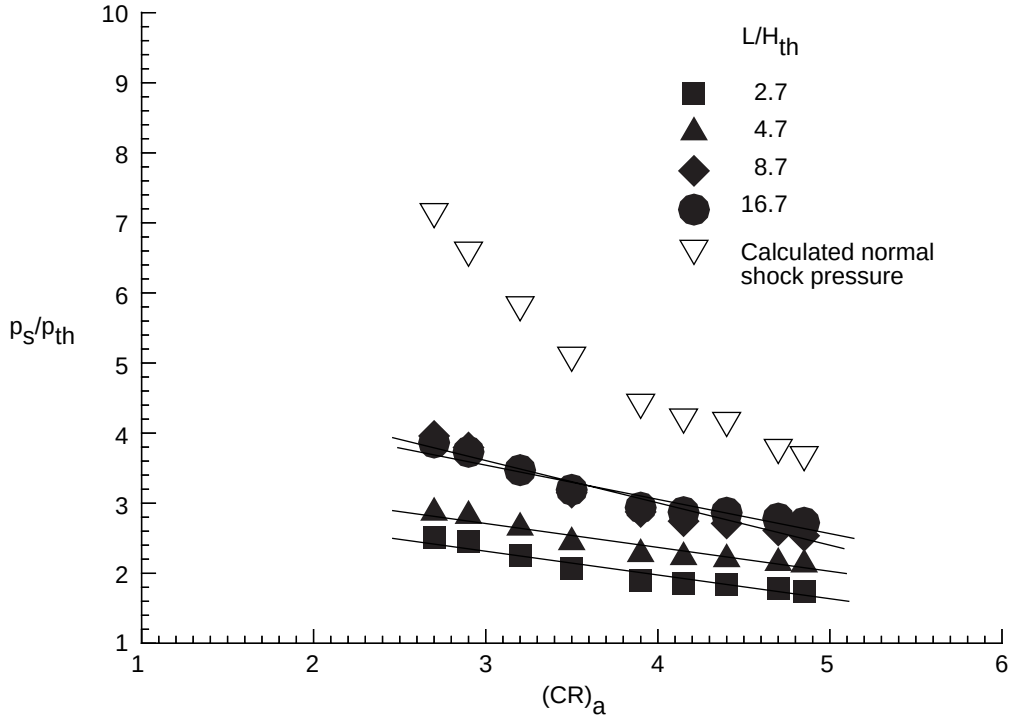

(a) Thin boundary layer.

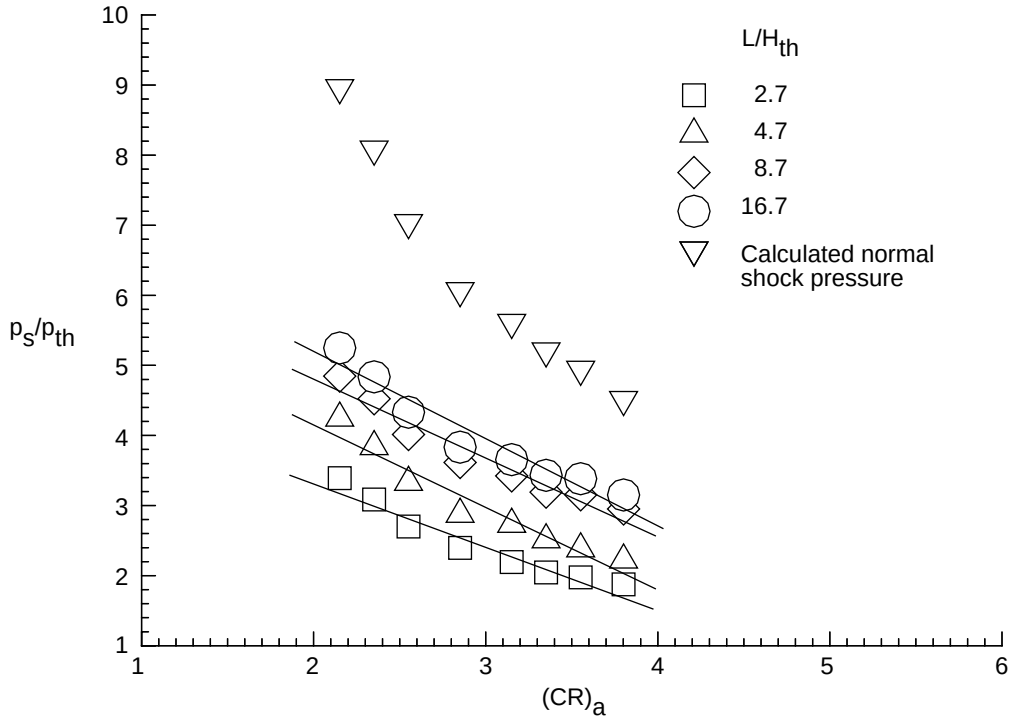

(b) Thick boundary layer.

Figure 35. Isolator effectiveness for 4.4-in. cowl (L_c/H_{th} = 11.00). Linear curve fit through data.

REPORT DOCUMENTATION PAGE

Form Approved
OMB No. 0704-0188

1. AGENCY USE ONLY *(Leave blank)*	2. REPORT DATE	3. REPORT TYPE AND DATES COVERED
	May 1995	Technical Paper

4. TITLE AND SUBTITLE
Experimental Investigation of Inlet-Combustor Isolators for a Dual-Mode Scramjet at a Mach Number of 4

5. FUNDING NUMBERS
WU 505-70-62-01

6. AUTHOR(S)
Saied Emami, Carl A. Trexler, Aaron H. Auslender, and John P. Weidner

7. PERFORMING ORGANZATION NAME(S) AND ADDRESS(ES)
NASA Langley Research Center
Hampton, VA 23681-0001

8. PERFORMING ORGANIZATION REPORT NUMBER
L-17422

9. SPONSORIING/MONITORING AGENCY NAME(S) AND ADDRESS(ES)
National Aeronautics and Space Administration
Washington, DC 20546-0001

10. SPONSORING/MONITORING AGENCY REPORT NUMBER
NASA TP-3502

11. SUPPLEMENTARY NOTES
Emami and Auslender: Lockheed Engineering & Sciences Company, Hampton, VA; Trexler and Weidner: Langley Research Center, Hampton, VA.

12a. DISTRIBUTION/AVAILABILITY STATEMENT
Unclassified–Unlimited
Subject Category 07
Availability: NASA CASI (301) 621-0390

12b. DISTRIBUTION CODE

13. ABSTRACT *(Maximum 200 words)*

This report details experimentally derived operational characteristics of numerous two-dimensional planar inlet-combustor isolator configurations at a Mach number of 4. Variations in geometry included (1) inlet cowl length, (2) inlet cowl rotation angle, (3) isolator length, and (4) utilization of a rearward-facing isolator step. To obtain inlet-isolator maximum pressure-rise data relevant to ramjet-engine combustion operation, configurations were mechanically back pressured. Results demonstrated that the combined inlet-isolator maximum back-pressure capability increases as a function of isolator length and contraction ratio, and that the initiation of unstart is nearly independent of inlet cowl length, inlet cowl contraction ratio, and mass capture. Additionally, data are presented quantifying the initiation of inlet unstarts and the corresponding unstart pressure levels.

14. SUBJECT TERMS	15. NUMBER OF PAGES
Inlet and isolator; Inlet unstart; Inlet restart; Supersonic inlet; Isolator back pressure; Isolator performance; Inlet operation; Ramjet; Scramjet; Combustion back pressure	90
	16. PRICE CODE A05

17. SECURITY CLASSIFICATION OF REPORT	18. SECURITY CLASSIFICATION OF THIS PAGE	19. SECURITY CLASSIFICATION OF ABSTRACT	20. LIMITATION OF ABSTRACT
Unclassified	Unclassified	Unclassified	